

Evaluation of PVDF Microstructure via Microbeam
Small-Angle X-ray Scattering after the Exposure to
Supercritical CO₂

A thesis

submitted to the Department of Chemistry
in partial fulfilment of the requirements for the
German academic degree Dr. rer. nat.

by

Fábio Gosi de Aquino

University of Hamburg

2015

Firstly, huge thanks to my family for their patience and to GE Oil & Gas for this
immeasurable opportunity.

Zuerst möchte ich mich bei meiner Familie für ihre Geduld bedanken, sowie bei
GE Oil & Gas für die großartige Gelegenheit.

Reviewers/Gutachter

1. Prof. Dr. Almut Stribeck

2. Prof. Dr. Luinstra

Disputation: 04.12.2015

Table of Contents

Abstract	xii
Zusammenfassung	xiv
Chapter I	2
Introduction	2
1.1. Unbonded Flexible Pipes	2
1.2. Poly(vinylidene fluoride) (PVDF)	9
1.2.1. Synthesis of PVDF	11
1.2.2. Crystallization from the Melt.....	12
1.2.2.1. α -Phase.....	14
1.2.2.2. β -Phase.....	15
1.3. Yielding in Polymeric Materials	17
1.4. Whitening in PVDF	18
1.4.1. Cold Forming in Polymers.....	22
1.5. CO ₂ Supercritical Conditions	23
1.6. Permeability of Gases Through Flexbarrier.....	25
1.7. Characterization of Structure Gradients in Polymers after Mechanical Loading	27
SAXS Theory.....	29
2.1 X-ray Scattering	29
2.2. Small Angle X-ray Scattering.....	31
2.2.1. The Magic Square	37
2.2.1. Chord Distribution Function	39
2.2.1.1. Step 1: Projection on the Representative Plane.....	39
2.2.1.2. Step 2: Laplacian and Background Correction	40
2.2.1.3. Step3: Fourier Transform	41
2.3. Objective	43
Chapter III	45
Experimental	45
3.1. Exposition Test of PVDF to Supercritical CO ₂	45

3.2.	Pipe Dissection and Specimens Retrieval	47
3.2.1.	SAXS Measurements.....	56
3.2.2.	Characterization by SEM.....	58
3.3.	Additional Samples for SAXS Measurements.....	61
3.4.	Mid-scale Swelling Test.....	63
	Chapter IV.....	69
	Results and Discussions	69
4.1.	Data Evaluation.....	69
4.2.	Virgin PVDF.....	73
4.3.	SAXS Results for PVDF Samples Exposed to Supercritical CO ₂	75
4.3.1.	Vertical Scans	75
4.3.2.	Horizontal Scans.....	86
4.3.3.	Quantitative Analysis.....	93
4.3.4.	Density Results	100
4.3.5.	WAXS Measurements.....	102
4.4.	SAXS – Additional Samples.....	105
4.5.	Mid-scale Swelling Test Result	108
	Conclusions and Future Works	112
	References	116
	Further Acknowledgments	133
	Eidesstattliche Versicherung	135

Nomenclature

$\mathbf{r} = (r_1, r_2, r_3)$	Real space vector and its components
$\mathbf{s} = (s_1, s_2, s_3)$	Reciprocal space vector and its components
$\rho(\mathbf{r})$	Electron density
$I(\mathbf{s})$	Scattering intensity
2θ	Scattering angle
λ	Radiation wavelength
\square	Slice mapping
\mathcal{F}_3	3D Fourier transform
\mathcal{F}_3^{-1}	Inverse 3D Fourier transform
μ	Linear absorption coefficient
ρ_i	Electron density of phase i (i=c crystalline phase, i=a amorphous phase)
ε_y	Yield strain
ε_b	Elongation at break
φ	Azimuthal angle
d	Length-scale of order in Bragg's law
L	Long period
\bar{h}_v	Void height
v_c	Volume crystallinity
\bar{d}_v	Void diameter
A	Area
Carcass	Metallic layer commonly made up of stainless steel
CO ₂	Carbon dioxide

Flexbarrier™ (inner liner)	Polymeric layer commonly made up with PVDF
Flexlok™ (hoop strength layer)	Metallic layer commonly made up of carbon steel
Flexwear™	Sacrificial layer commonly made up of PVDF
$g(r)$	Chord length distribution (CLD)
$g_1(r)$	Interface distribution function (IDF)
$h_i(r_{12}, r_3)$	Distance distribution (peaks of CDF)
I_{Fl}	Intensity fluctuation background
k	Total scattered intensity (invariant)
MAXS	Middle-angle X-ray scattering
l	Distance between fiducial marks
l_0	Initial distance between fiducial marks
L_b	Long period of a transverse lamellae-stack
$P(\mathbf{r})$	Patterson function
p	Differential pressure
PA11	Polyamide 11
PA12	Polyamide 12
PE	Polyethylene
Pre-salt	Cluster of oil and gas reserves in Brazil
PVDF	Poly(vinylidene fluoride)
R	Sample-detector distance
RGD	Rapid gas decompression
s	Modulus of s -vector
s	Wall thickness

SAXS	Small-angle X-ray scattering
SEM	Scanning electron microscopy
t	Time
USAXS	Ultra-small-angle X-ray scattering
V	Irradiated volume
v	Volume fraction
WAXS	Wide-angle X-ray scattering
$z(r)$	Chord distribution function (CDF)
1D	One-dimensional
2D	Two-dimensional
3D	Three-dimensional

Abstract

In order to mimic extreme service conditions, a segment of flexible pipe has been subjected to rapid gas decompression. Following the test, it was observed that the poly(vinylidene fluoride) (PVDF) layers had swollen into the gaps between the adjacent metallic layers, forming noses (or cusps), which turned white. The nanostructure gradient was studied by small-angle X-ray scattering (SAXS). SAXS was also carried out, both in the zones where the upper metallic layer had broken and where it retained integrity.

SAXS patterns showed two features related to void scattering and the scattering of the semi-crystalline morphology. Remote from the noses and from the damage zone, there are no voids. The isotropic morphology may be compared to that of a virgin pipe. Flexwear exhibits a constant crystallinity (50%). In the Flexbarrier layer the crystallinity increases to 58%. For the Flexbarrier, voids were detected only in depths up to 1 mm in the whitened region. In depths below to 1 mm no voids were detected.

Approaching the noses, the morphology changes from semi-crystalline layer stacks to highly orientated microfibrils. Needle-shaped voids are orientated, parallel to the microfibrils. In the Flexlok gaps, where the noses appear, the structure turns almost perpendicular to the layer. Away from the damage zone, the voids only penetrate into part of the layers. In the damage zones, voids and orientation of the crystalline domains are observed throughout the layers. Domain orientation extends out to either side of the whitened nose regions. The changing orientation direction and void formation are restricted to the white regions, indicating that chronologically successive mechanisms of cold drawing are mapped into the space. Orientation alignment is lowest in the wear layer away from the damage, and highest in the barrier directly under the damage.

Complementary tests have been performed in order to assess the effects of the whitening, such as observations by means of SEM, Density and WAXS in order to investigate any phase transformation of PVDF.

As part of this thesis, a mid-scale swelling test has been carried out at 90°C. The microstructure of PVDF in the regions of whitening could be observed by SEM up to 10µm and such images could be indirectly compared to SAXS results. No significant density variation was encountered comparing the virgin with the whitened material. No phase transformation of PVDF in the whitened region has been detected by means of WAXS.

Another mid-scale swelling test has been carried out, however it failed, and the aim of the test was to quantify the strain imposed on the Flexlok due to swelling of the Flexbarrier. This test will be repeated.

Zusammenfassung

Ein Rohrsegment wurde mit einem superkritischen Fluid gefüllt und einer schnellen Dekompression unterzogen um extreme Betriebsbedingungen einer flexiblen Steigleitung zu imitieren. Das Rohr enthält zwei dicke Polymerschichten aus Poly(vinylidenfluorid) (PVDF) mit den Bezeichnungen Flexbarrier (Sperrschicht) bzw. Flexwear (Abnutzungsschicht). Nach dem Test wurde beobachtet, daß die beiden Schichten in die Lücken der darüber liegenden Metallkarkassen geflossen waren. Die gebildeten Nasen (d.h. Ausbuchtungen) waren weiß geworden. Quer und längs durch die Nasen wurden Scans mit einem Röntgen-Mikrostrahl durchgeführt und die Röntgenkleinwinkelstreuung (engl.: SAXS) registriert. So konnte die Änderung der Nanostruktur als Funktion des Ortes („Nanostruktur-Gradient“) bestimmt werden. Da im Test die Metallarmierung an einer Stelle gebrochen war, wurden die Gradienten sowohl in der Bruchzone als auch im intakten Gebiet bestimmt. Zum Vergleich wurde auch ein jungfräuliches Rohr untersucht.

Das jungfräuliche Rohr zeigt nur die bekannte isotrope Streuung von teilkristallinem PVDF. Die aus der SAXS bestimmte Volumenkristallinität beträgt 50%. In der Flexwear-Schicht des getesteten Rohrs hat sich die Kristallinität nicht geändert. In der näher am warmen fluiden Medium liegenden Flexbarrier-Schicht ist die Kristallinität auf 58% gestiegen.

In den Scans zeigen die SAXS-Streubilder einen Übergang von isotropem PVDF zu uniaxial hoch orientiertem Material, wobei sich die Achse kontinuierlich dreht. Dies wurde vorher noch nie festgestellt. Jedes Streubild hat zwei gut unterscheidbare Merkmale. Meridionale Streuung wird verursacht von der der teilkristallinen Morphologie; äquatoriale Streuung kann auf nadelförmige Mikro-Hohlräume zurückgeführt werden. Außerhalb der Schädigungszone und weit weg von den Nasen gibt es keine Mikro Hohlräume. In den Nasen liegen die nadelförmigen Poren meist in der Schichtebene, so dass sie die Sperrwirkung nur wenig mindern. Nah an Kanten der Metallkarkasse drehen sie sich jedoch quer zur Schichtrichtung. Der negative Effekt kann minimiert werden, indem man das Design der Metallkarkasse optimiert. Günstig ist außerdem, dass im

Flexbarrier abseits der Schädigungszone, Mikrohohlräume nur in einer dünnen Teilschicht der weiß gewordenen Regionen festgestellt wurden.

Die teilkristalline Morphologie ändert sich beim Scan durch die Nasen deutlich. Fern von den Nasen findet man isotrope Stapel aus abwechselnd kristallinen und amorphen Lamellen. Bei der Annäherung an die Nasen beobachtet man einen Übergang zu hochorientierten Mikrofibrillen, die aus kornförmigen Kristalliten bestehen. Dazwischen befindet sich amorphes Matrixmaterial. Diese Strukturänderung kennt man von Dehnversuchen. Dort wird sie allerdings als Funktion der Zeit beobachtet. Man kann also sagen, dass in unserem Material die verschiedenen Stadien der Kaltverformung („cold forming“) in den Raum abgebildet worden sind.

SEM-Untersuchungen und Dichtemessungen wurden durchgeführt, um weitere Auswirkungen der Material-Aufhellung zu überprüfen. Die SEM-Ergebnisse zeigen die Mikrostruktur des Materials mit einer Auflösung von 10 μm . Bei den Dichtemessungen wurden keine signifikanten Änderungen festgestellt. Mit der Röntgen-Weitwinkelstreuung wurde festgestellt, dass auch keine Änderung der Kristallmodifikation des PVDF auftritt.

Ein zweiter Großversuch (“Mid-scale swelling test“) wurde durchgeführt und in dieser Arbeit beschrieben. Leider versagte der Test. Er wird in nächster Zeit wiederholt. Ziel des Tests ist es, die Belastung des Flexlok durch eine Quellung des Flexbarrier festzustellen.

Acknowledgments

I would like to thank Prof. Dr. Stribeck for her support during the execution of this PhD program. I also would like to thank Dr. Stefan Buchner for several valuable technical discussions concerning polymers, PVDF under supercritical conditions, etc., contributing to my understanding. I also recognize that without his help and friendship, it would have been difficult to perform such a PhD program in Hamburg. I also would like to thank my colleagues at Hamburg University, in particular Farhad Jokari-Sheshdeh for his friendship and prompt attention when claimed.

Many thanks also to GE Oil & Gas for such a great professional and personal opportunity. Special thanks to Judimar Clevelario and Fabio Pires for their support and patience during my absence from Rio de Janeiro.

Chapter I

Introduction

'Imagination is more important than knowledge. For knowledge is limited, whereas imagination embraces the entire world, stimulating progress, giving birth to evolution.'

...Albert Einstein

1.1. Unbonded Flexible Pipes

The oil and gas industry is one of the sectors with the highest number of production systems employing high technology. Inside the production chain, a great part of the oil and gas produced is conveyed through flexible pipes, which connect the production wells to the platforms ⁽¹⁾.

Unbonded flexible pipe has been employed for more than 25 years as static flowlines and dynamic risers, with fixed and floating production systems and has recently been qualified and applied in water depths of up to 2500m. Specifications and recommended practices for bonded and unbonded flexible pipe design are included in API standards 17B, 17J and 17K. An unbonded flexible pipe is made up of successive thermoplastic and steel layers, while bonded flexible pipe is made up of steel reinforced with elastomers.

The use of flexible pipes is increasing, as advantages for installation and layout accommodation on the seabed, in deep and ultra-deep waters, become more promising in this market.

Unbonded flexible pipes consist of highly engineered concentric layers of metallic wires, tapes and extruded polymers designed to form a structure that address the specific environmental requirements and characteristics of the transported production fluids. The flexibility of the pipe is engineered and controlled by designing the reinforcement layers to allow small relative movements between the layers ⁽²⁾.

In flexible pipes, the internal pressure sheath, Flexbarrier™, works as a sealing layer. As the carcass, the innermost metallic layer, does not provide the sealing of the fluids, because of its interlocked conformation, a polymer layer – typically Polyamide 11 (PA11), Polyamide12 (PA12) or Poly(vinylidene fluoride) (PVDF) is extruded onto the carcass, in order to prevent fluid leakage into the subsequent layers, see Figure 1.

The polymer which constitutes the Flexbarrier must also be compatible with the operating conditions and with the conveyed fluids. In PVDF structures, an additional extruded layer, Flexwear™, can also be used as sacrificial layer.

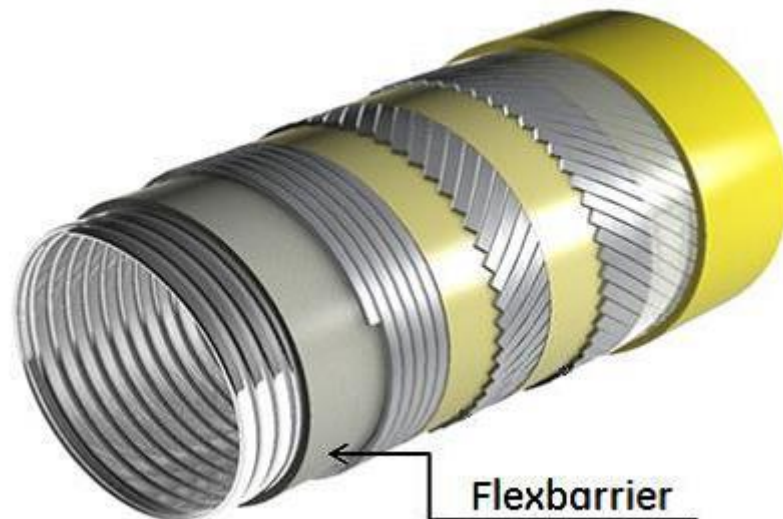


Figure 1 – Schematic view of Flexbarrier position on unbonded flexible pipes, comprising typically of Polyamide 11 (PA11), Polyamide12 (PA12) or Poly(vinylidene fluoride) (PVDF). It is extruded onto the carcass in order to prevent leakage of oil and gases to the upper layers, as well as into the surrounding environment.

It is important to highlight that the Flexbarrier, when in service, is in direct contact with the internal fluids from wells since, as already noted, the carcass is merely an interlocked structure with no sealing function, only structural, as shown in Figure 2 ⁽²⁾.

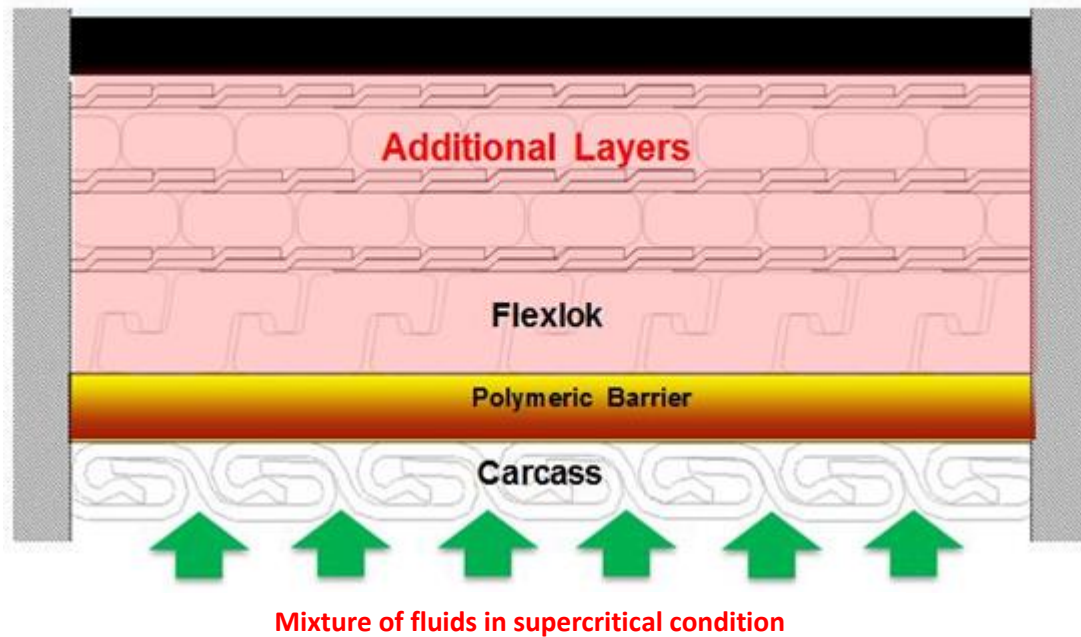


Figure 2- Sketch of a typical structure of an unbonded flexible pipe. Technical terms are labelled. The innermost metallic layer, the carcass, is surrounded by the Flexbarrier, which provides the sealing of the flexible pipe.

The Flexlok™ sits right above the Flexbarrier and is also an interlocked structure, like the carcass. In the interlocking regions of the Flexlok and carcass wires, there are some gaps; such conformation is very important in providing the pipe's flexibility. Figure 3 presents a sketch showing, in general lines, the gaps between the carcass wires and the Flexlok.

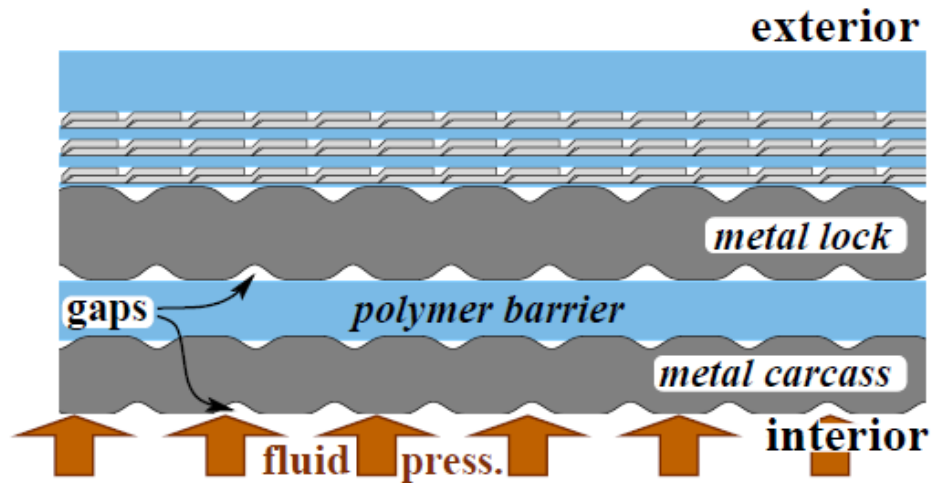


Figure 3 – Schematic representation of the gaps between the carcass and Flexlok, which give the pipe its flexibility.

The selection of each material relates to the field conditions in terms of fluid composition, temperature and pressure.

One of the biggest challenges currently faced by the offshore industry is related to the discovery of the reserves off the Brazilian coast, between Santa Catarina and Espirito Santo, around 800km offshore. Such reserves contain over 8 billion barrels of oil, along with high levels of carbon dioxide (CO₂).

The almost impermeable rock formation and the saline cap acts as a physical barrier avoiding leakage of the CO₂. Thus the CO₂ remains stored efficiently. Such geological formation can also benefit enhanced light oil production, permitting the application of sustainable technologies ⁽³⁾. Such a cluster is called the pre-salt, since it is located beyond a salt layer of ≥ 2000m thickness. Figure 4 shows a sketch of a pre-salt formation.

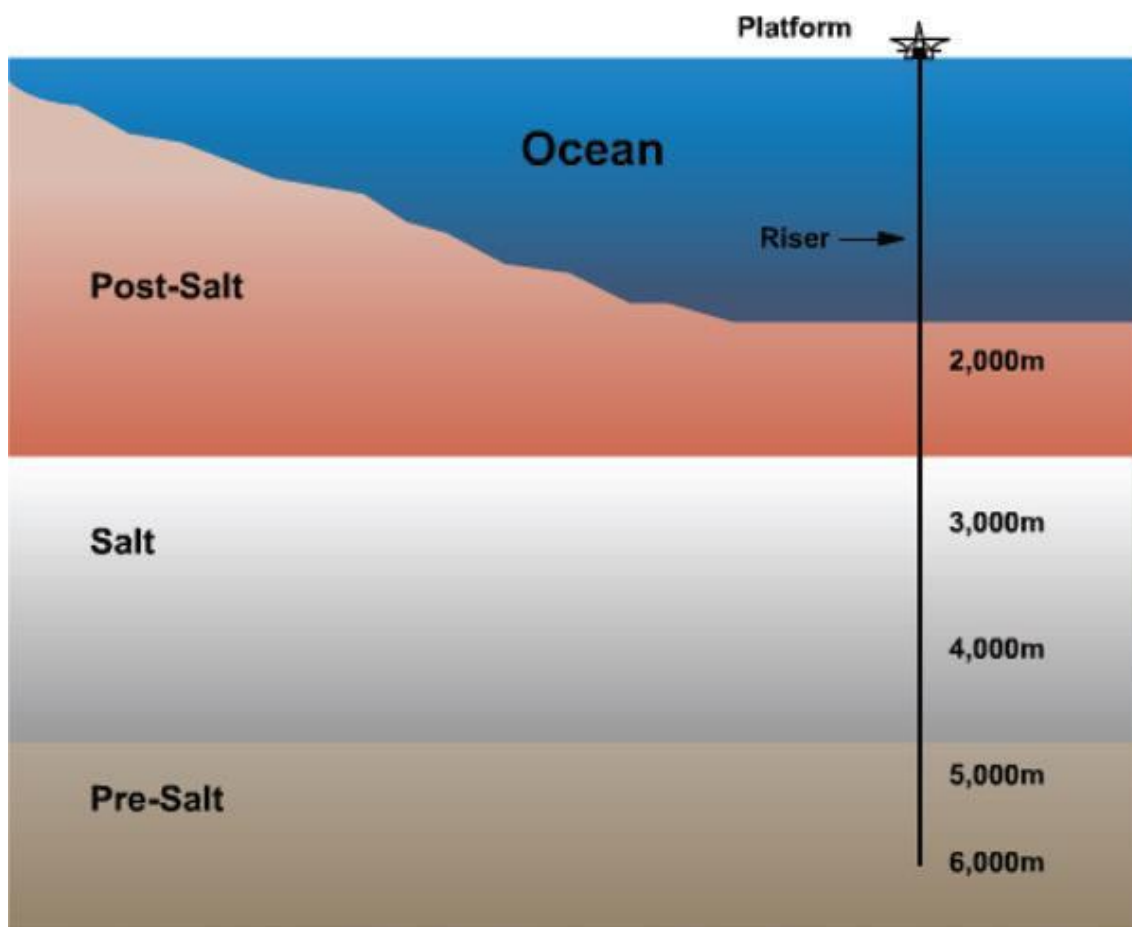


Figure 4 – Sketch of the arrangement of pre-salt formation between the platform of exploration of oil and gas and the oil and gas reservoirs.

Due to the high pressure and temperature of such wells, the CO₂ can be under supercritical condition.

Pre-salt wells represent a great opportunity and probably the most important recent oil field discovery, which is going to be a great challenge for the production project.

From a production point of view, this new frontier has technological challenges and special attention must be paid to anticipate potential problems ⁽⁴⁾. This thesis forms part of such anticipation.

One of the technological challenges are rapid gas decompression operations, which are well known in the offshore industry from 'stop for maintenance' events

or due to other specific service conditions. Previous surveys have already been performed on polymers applied as Flexbarrier layers covering supercritical CO₂, in order to ascertain the effects of such decompression operations on the morphology of the polymers used as Flexbarrier ⁽²⁾. It is important to highlight that the decompression rates can reach up to -70bar/min.

Thus it is considered important to determine whether a Flexbarrier layer can withstand such rapid gas decompression operations under severe service conditions, since a flexible pipe is manufactured for a period of ≥30 years use.

The influence of the supercritical media on the microstructure of the current qualified polymeric materials, in particular PVDF, is being performed by flexible pipe manufacturers in order to provide better understanding of the effects of the supercritical CO₂.

PVDF is widely used in the manufacture of flexible pipes for instance, as the Flexbarrier. PVDF is a semi crystalline polymer, developed in the 1970s, which presents good thermal mechanical properties ⁽⁵⁾. Further and recent investigations have shown the notably good resistance to aging, as well as good resistance to crude oil ⁽⁶⁾.

Recent tests have demonstrated the occurrence of whitening in PVDF after exposure to supercritical CO₂, followed by rapid gas decompression operations ⁽⁶⁾. In addition, the occurrence of whitening under mechanical loading has already been reported for PVDF. Further studies and understanding regarding the appearance of this whitening are required for upcoming applications of PVDF under extreme conditions. The surveys related to the mechanical properties of the polymer after whitening and also the microstructure of the material may help to assess the importance of this effect, however there is little information regarding this topic available in the literature ⁽⁷⁾.

In this context, this research program intended to investigate the microstructural changes of PVDF, which may be observed in the whitened zones and their environment. For that, a pipe segment was subjected to a supercritical CO₂

environment, followed by a rapid gas decompression operation. Following the test, some samples were retrieved for further investigations. Whitening was studied by microbeam small-angle X-ray scattering (SAXS), and scanning electron microscopy (SEM), among other techniques.

1.2. Poly(vinylidene fluoride) (PVDF)

PVDF is a plastic material in the fluoropolymer family. It is used generally in applications which require highest purity, strength, resistance to solvents, resistance to acids and bases, thermal stability and low smoke generation during a fire event. Compared to other fluoropolymers, it has an easier melt process because of its relatively low melting point of around 177°C. Figure 5 shows the chemical structure of PVDF.

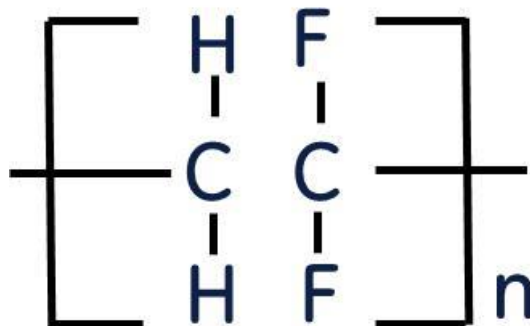


Figure 5 – This figure illustrates the structural arrangement of PVDF, a plastic material in the fluoropolymer family.

As we entered the decade of 1980s, PVDF, a polymer known for decades, yet little studied before 1970, found itself at the center of polymer science attention. Perhaps no other single polymer has generated so much excitement or, with the possible exception of PE (Polyethylene), received so much attention. Indications of this can be found in more than a thousand papers published on PVDF in the previous decade, in the many hundreds of patents associated with it, in the sessions concerned solely with it during recent national and international scientific meetings, and in special journal issues devoted primarily to this polymer ⁽⁵⁾.

PVDF, also commonly abbreviated as PVF2, has been intensely investigated because of its interesting ferroelectric properties and technological applications ⁽⁸⁾. PVDF is a semi-crystalline polymer, with crystallinity varying between 40 –

60%. It can exist in several crystalline phases. It can crystallize into five possible modifications namely ^(9,10), α , β , γ , δ and ϵ , depending on the crystallization condition. The mutual transformation of these crystalline phases can be achieved by thermal, mechanical, or electrical treatment ⁽¹¹⁻¹⁴⁾.

Of the five known modifications, the α - and β -phases are the most common. The α -form, the more common and stable, arises usually from the melt when PVDF crystallizes in quiescent conditions.

The β -form offers the highest piezo-, pyro-, and ferroelectric properties. To obtain β -PVDF, a technological process involving stretching and poling of extruded thin sheets of the polymer is used, resulting in a permanent polarization. Uniaxial stretching provides the alignment of molecular chains ⁽⁸⁾.

PVDF has offered one of the most interesting and fruitful subjects for structure analysis in the entire domain of engineering materials ^(15,16). No material combining both the mechanical and the electrical properties required has been available until the advent of PVDF ⁽⁵⁾.

1.2.1. Synthesis of PVDF

PVDF is generally produced by the free-radical polymerization of 1,1-difluoroethylene (VF₂)⁽¹⁷⁾, a monomer commonly synthesized from acetylene or vinylidene chloride via 1-chloro – 1,1 – difluoroethylene.

The most prevalent polymerization processes take place in suspension or emulsion. Water is generally the medium, with peroxy compounds serving as the chosen catalysts for both suspension⁽¹⁸⁾ and emulsion⁽¹⁹⁾ polymerizations.

Under most circumstances, the reaction temperatures range from 10 to 150°C and pressures from 10 to 300atm⁽¹⁷⁾. The polymerization temperature has a significant effect on the formation of the units within the molecular backbones⁽²⁰⁾. The precise conditions of the polymerization may influence the molecular weight⁽²¹⁾ or the crystalline structure of the as-synthesized material^(22,23). Radiation-polymerization in polar solvents promotes formation of the β -phase^(22,23), while non-polar solvents (or gaseous polymerization) yield the α -phase⁽²³⁾.

1.2.2. Crystallization from the Melt

The most common polymorph produced during the crystallization from the melt is the α -form. It is essentially the sole crystalline phase obtained at all temperatures up to approximately 150°C. The first morphological studies of crystallization of PVDF, as a function of the temperature, were conducted by Gianotti et al.⁽²⁴⁾ and Prest et al.⁽²⁵⁾. Both groups reported the formation of a second spherulitic phase at crystallization temperatures higher than 150°C.

Figure 6 shows large spherulites, which belong to the α -form and are characterized by high birefringence and extremely tight concentric banding. The small spherulites belong to the γ -form, which is generally obtained in temperatures higher than 150°C. Figure 7 shows the spherulitic morphologies of PVDF in 30/70 (w/w) PVDF/PHB blends crystallized isothermally at 145 °C⁽⁵⁾.

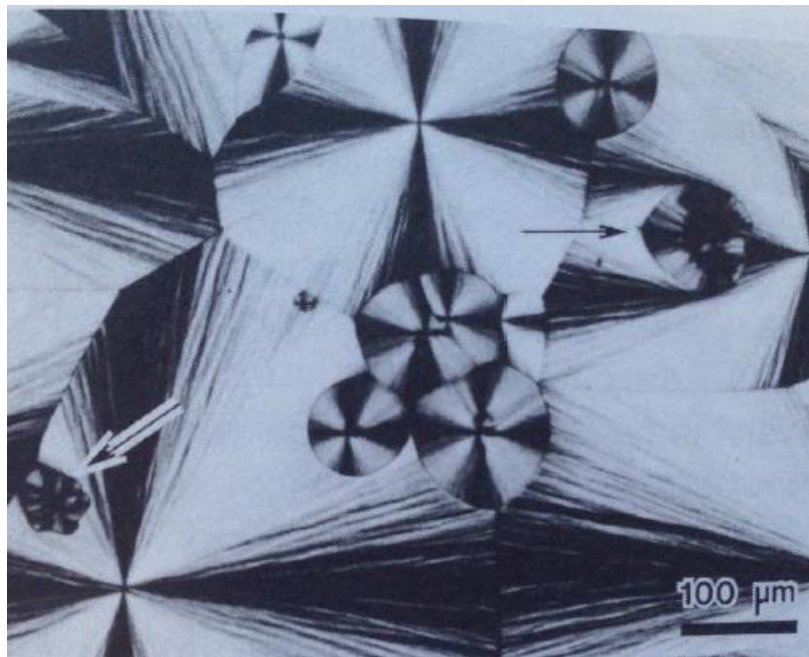


Figure 6 – Appearance of PVDF spherulites (crystallized at 160°C) in polarizing microscope. The large spherulites belong to the α -phase, the small to the γ . Irregular γ -spherulites are identified by arrows⁽⁵⁾.

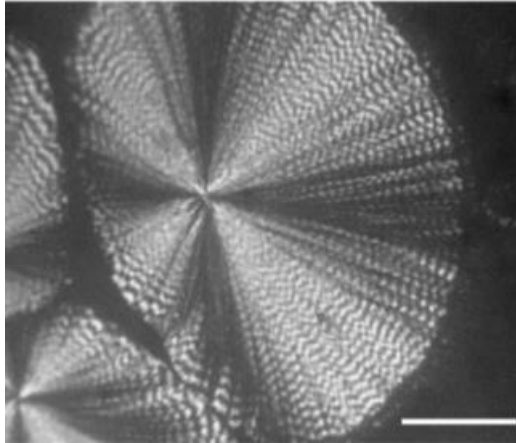


Figure 7 - Spherulitic morphologies of PVDF in 30/70 (w/w) PVDF/PHB blends crystallized isothermally at 145 °C (size bar 100 μm).

The melting behavior and attendant thermo-dynamical properties of PVDF have been reported by a number of authors ⁽⁵⁾. Melting in PVDF is complicated by the number of polymorphous, by inter-conversions among them, by effects of H-H, T-T defects and deviations from the traditional behavior ⁽⁵⁾. However, the semi-crystalline morphological form obtained during the crystallization of PVDF is extremely important for the final material's properties.

1.2.2.1. α -Phase

The α -phase is the most common polymorph of PVDF and is normally obtained by crystallization from the melt at moderate or high undercooling ⁽⁵⁾.

The α -phase is frequently established when mechanical performance is required. Among others, it shows greater stability. It is a nonpolar phase and it has a conformational chair structure of the type trans-gauche (TGTG').

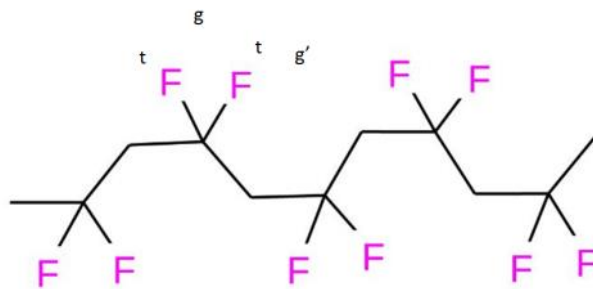


Figure 8 – Sketch of the space arrangement of the α -form of PVDF.

From the α -phase, by means of thermal, mechanical or electrical treatments, other phases can be obtained ^(26,27). Figure 8 shows the space arrangement of the α -form.

The α -form is the PVDF conformation used in the production of Flexwear and Flexbarrier.

1.2.2.2. β -Phase

The β -phase is used extensively in piezoelectric and pyroelectric applications. It is routinely obtained by mechanical deformation of melt-crystallized films ⁽⁵⁾.

Materials having piezoelectric property are part of a class that can convert mechanical energy into electrical energy or electrical energy into mechanical energy. The piezoelectric effect is constituted by a linear coupling between an electric field applied to an induced voltage, or a mechanical energy producing an electrical polarity ⁽²⁸⁾. Figure 9 shows the space arrangement of the β -form.

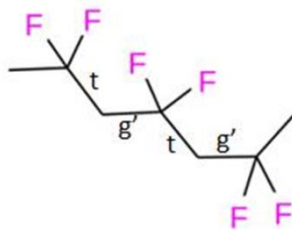


Figure 9 – Sketch of the space arrangement of the β -form of PVDF.

The β -phase is a polar phase with conformational structure of the planar zig-zag, type (TTT) with unit cell also in the orthorhombic form.

The microstructure of PVDF in the β -phase strongly depends on the way in which the phase is obtained ^(11,12). By stretching from the α -phase at precise stretch ratios, at defined temperatures, the microstructure changes from a spherulitic to a microfibrillar structure, from α -phase to β -phase ^(29,30). No further information was found in the literature regarding these conditions, beside that as described by J. Serrado Nunes et al ⁽³¹⁾.

Figure 10 shows the microstructural conformation of the different samples prepared by J. Serrado Nunes et al ⁽³¹⁾. Figure 10a shows a spherulitic conformation of α -PVDF, isotropic material. Figure 10b shows the β -PVDF obtained by stretching of the α -phase. The material no longer presents spherulites, being characterized by an oriented microfibrillar microstructure.

PVDF films with thickness between 20 and 30 μm were produced by spreading a PVDF/dimethylformamide (DMF, Merck 99.5%) solution with an initial concentration of 20 wt% PVDF on a clean glass substrate.

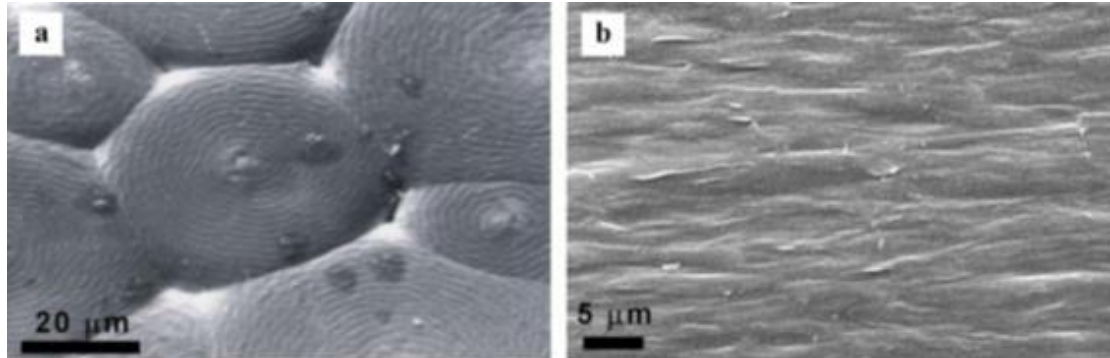


Figure 10- Scanning electron microscopy (SEM) surface images of (a) α -PVDF; (b) β -PVDF stretched at 80°C (31). α -PVDF shows a spherulitic conformation and β -PVDF is characterized by an oriented microfibrillar microstructure.

1.3. Yielding in Polymeric Materials

The yielding behavior of polymer materials has been studied for years ⁽³²⁻³⁵⁾. Respective experiments reveal characteristic parameters for the predication of suitability of the polymer material in load-bearing applications. However, they indicate fundamental mechanisms, and some of them are still not well known. For a viscoelastic polymer, the yielding point can be associated with the onset of significant plastic flow ^(36,37). On a molecular level, the yielding is associated with inter-chain sliding, chain segmental motion and chain re-conformation, which are characterized as rate processes ⁽³⁸⁾. This means that the yielding behavior of such polymer materials is sensitive to changes in temperature, strain rate and pressure ^(39,40,41). Under tension, the spherulitic texture which frequently forms a semi-crystalline polymer is deformed. Above the yield point, the spherulitic structure is destroyed and transformed into a fibrillar structure ^(42,43). Additionally, during yielding, stress-whitening of the material may occur ^(44,45).

1.4. Whitening in PVDF

It has been observed that polymeric materials under conditions of mechanical deformation such as tensile, impact, or fatigue loading, or mechanically induced scratch have the tendency to exhibit a whiter appearance. That is, an initially transparent or translucent polymeric material exhibits enhanced opacity and a whiter color leading to increased optical brightness, referred as 'stress whitening' ^(46,47). In general, it is believed that the formation of voids and microcrazes, the agglomeration of voids, lead to stress whitening in polymeric materials. It was observed in the studies regarding the mechanism of crazing that the nucleation of craze initiates with the formation of deformation bands, and the growth occurs by a process that involves existing voids advancing finger-like extensions into the bulk polymer, linking up the stretched fibrils in their wake ^(46,47).

The tensile deformation of spherulites in semi-crystalline polymers has received considerable attention including several reviews ⁽⁴⁸⁻⁵²⁾, as well as numerous experimental investigations ⁽⁵³⁻⁵⁹⁾.

Several authors have noted that the earliest damage takes place by voids in interlamellar regions within the spherulites ⁽⁴⁸⁻⁵⁴⁾, primarily in the equatorial plane, perpendicular to the stress axis. Other studies have observed interspherulitic voids in addition to trans-spherulitic void formation ^(49-52,57,59). The structure of these void regions is not clear, but numerous studies have reported voids in semi-crystalline polymers ^(52, 54-57, 59).

As in other crystalline polymers (e.g. Polyethylene (PE), Polypropylene) (PP) ⁽⁶⁰⁾ and Polyoxy Methylene (POM) ^(61,62)) the voids can change some of the mechanical properties of the PVDF when strained.

Mechanical properties of PVDF have been already studied by some authors, who analyzed the macroscopic tensile and creep behavior over several strain rates and over a large range of temperatures ^(63,64). During the viscoplastic deformation, the material whitens after the onset of necking due to nucleation

and growth of voids, as already evidenced using small and wide angle X-ray diffraction ⁽⁶⁵⁾. This increased scattering is regarded by many authors as the macroscopical evidence of voids and/or a microcracking process ^(60,66-69).

As per Castagnet ⁽⁶⁵⁾, microvoids in PVDF are nucleated within the amorphous phase. In tension, the void starts in the amorphous layers between the crystalline lamellae perpendicular to the stress axis. As the elongation of spherulites increases, the void spreads out progressively to the amorphous layers more inclined towards the stress axis. The void is emerging due to the 'negative pressure' between crystallite lamellae when they are separated by the applied stress. When amorphous material can flow rapidly enough to fill the volume created between drawn lamellae, this negative pressure is significantly reduced, so that the void no longer occurs.

Figure 11 shows the elongation at yield (ϵ_y) and at break (ϵ_b) of 2 α -PVDFs vs temperature. Close to room temperature, the yielding of the α -PVDF occurs at around 10% of elongation. These grades of PVDF are also used in the manufacture of flexible pipes from a non-disclosed source.

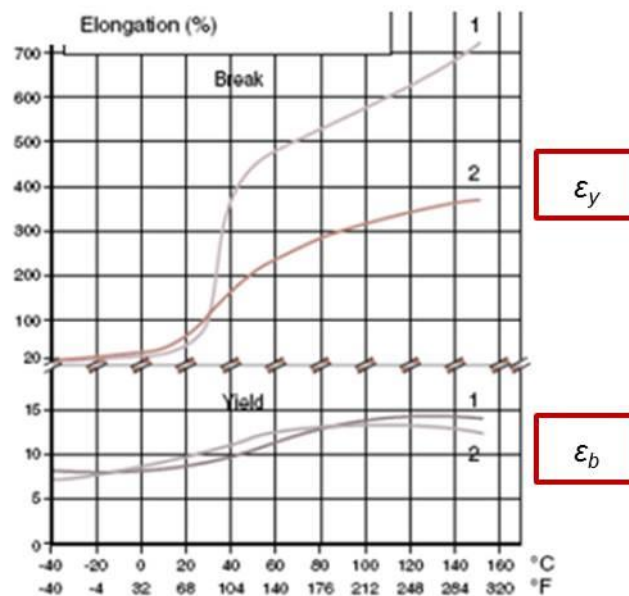


Figure 11- Elongation at yield and at break of α -PVDF vs temperature. Curve 1 is related to one grade of PVDF, and Curve 2 is related to a second grade also used for the manufacture of flexible pipes.

In order to investigate the occurrence of whitening close to the yielding of the PVDF, further internal surveys have already been performed for PVDF used as the Flexbarrier. The elongation of the specimens was stopped at specific degrees of elongation (%), in order to investigate the occurrence of voids by means of scanning electron microscope (SEM) ⁽⁷⁰⁾.

Figure 12 shows SEM images at 10.000x magnification for specimens elongated up to 1, 5, 10, 12, 15, 18 and 25%. The beginning of the voids formation is observed at 15% elongation, increasing up to 18% elongation. At 25% elongation no voids were observed anymore, probably related to the coalescence of the voids, leading to a typical morphology characterized by crazes.

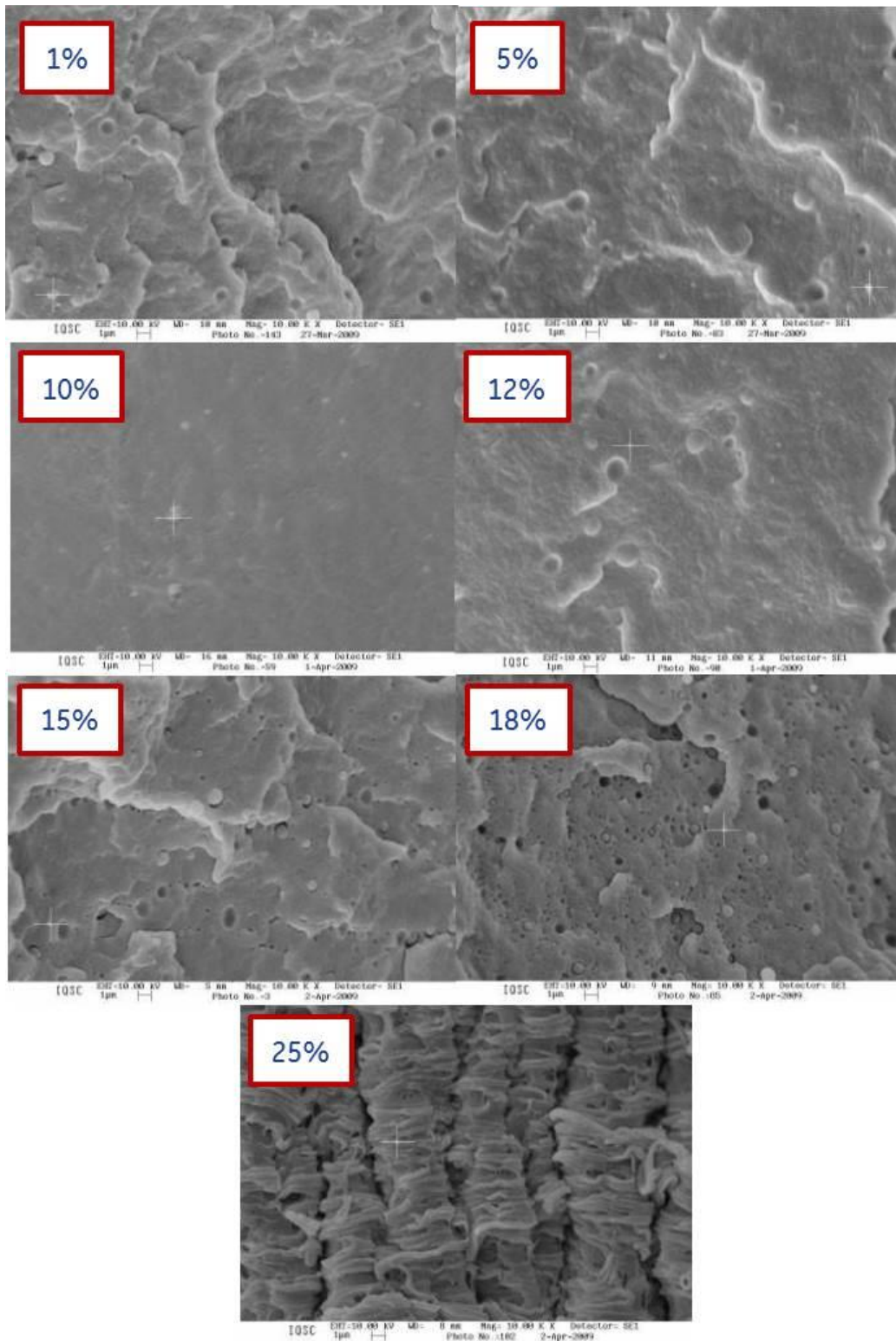


Figure 12- SEM images at 10.000x magnification for specimens elongated up to 1, 5, 10, 12, 15, 18 and 25% respectively. The samples were retained from a Flexbarrier and the specimens elongated in the direction of the extrusion of the pipe.

The whitening is reported to make the products more susceptible to diffusion of liquids and gases and more susceptible to fracture ⁽⁷¹⁾.

1.4.1. Cold Forming in Polymers

The deformation of material at temperatures below the melting point is generally referred to as cold forming. For Nylon 6 it has been reported in the literature ⁽⁷²⁾, that this can alter the crystallinity, orientation and morphology of the material. SAXS and WAXS were proved to be the ideal analysis techniques to detect such changes.

For PVDF which has been solidified at low cooling rates, it has been reported that the cold forming would lead to the occurrence of whitening ⁽⁷³⁾.

After cold forming of PVDF at temperatures between 60°C and up to 160°C, improvements in mechanical properties have been found ^(74,75). In addition, a more or less pronounced change in crystal modification has been reported, but even if the crystal modification persists, the isotropic small-angle scattering pattern changes into a layer line pattern ⁽⁷⁶⁾.

Plastic deformation of crystals is not assumed in the initial stage of the cold-forming process, that is, the energy-elastic crystal deformation is reversible. Crystals orientate with the chain axis parallel, perpendicular, or at an intermediate angle to the draw, respectively, depending on the shape and the local orientation within the amorphous structure. Irreversible, plastic deformation of crystals is observed when the local stress exceeds a critical value ⁽⁷⁷⁾.

1.5. CO₂ Supercritical Conditions

A large amount of work has recently been developed on the solubility of fluorinated polymers and copolymers in CO₂. However, studies have been done and proved that for poly(vinyl fluoride) (PVF) or PVDF even at temperatures of 300 °C and pressures of 2750 bar the polymer would not dissolve ⁽⁷⁸⁾.

Supercritical CO₂ has attracted much attention because the environmentally friendly, chemically inert, inexpensive, and nonflammable CO₂ can be an alternative to substitute organic solvents.

CO₂ has a critical temperature near room temperature, at a modest critical pressure, ((T_c) 31.1 °C and (P_c) 72.8 atm) and it has a higher density than most supercritical fluids, which means that at temperatures slightly above room temperature, it is possible to obtain liquid-like densities and, by implication, liquid-like solvent characteristics. CO₂ has proven to be a very good supercritical fluid solvent for a select variety of polymers and copolymers.

The solubility of polymers in supercritical CO₂ is, fortunately, very low due to a lack of strong interactions between polymer and CO₂ and to a very low entropy driving force for mixing CO₂ with polymers. The supercritical CO₂ used as a solvent for synthesis, modification, and processing of polymers is thus qualitatively different from the organic solvents.

Although very few polymers were reportedly soluble in supercritical CO₂, especially true for crystalline polymers, some polymers with carbonyl groups ^(79,80), ether linkages ^(79,81), or C-F linkages have specific interactions with CO₂ ^(82,83).

It has also been shown recently that it is possible to dissolve poly(tetrafluoroethylene-co-hexafluoropropylene) with 19 mol % hexafluoropropylene in CO₂ at temperatures in excess of 175 °C and pressures near 1000 bar ^(84,85).

Beckman and co-workers argue that the solubility of the copolymer depends on a somewhat complex manner on the number of fluorinated side groups and on

the molecular weight of the side groups relative to the molecular weight of the hydrocarbon main chain ⁽⁸⁶⁾. Very recently, Howdle and co-workers have synthesized polymers with fluorinated heptyl-acrylates that are soluble in CO₂ ⁽⁸⁷⁾.

Krukonis has shown that CO₂ at or near room temperature and at pressures typically below 600 bar can be used to solubilize polymeric oils, such as many poly-(dimethylsilicone) and poly(phenylmethylsilicone), perfluoro-alkyl polyethers, and chloro- and bromotrifluoroethylene polymers ^(88,89,90).

Beckman and co-workers have described the solubility of poly(perfluoropropylene oxide) and poly(dimethylsiloxane) in CO₂ ^(91,92). Barton ^(93,94) and Kiran ⁽⁹⁵⁾ have also reported on the high solubility of poly(dimethylsiloxane) in CO₂ at approximately 450 bar. It is possible to dissolve very low molecular weight, slightly polar polymers, such as polystyrene or telechelic polyisobutylene, with molecular weights below 1000 in supercritical CO₂ ^(88-90, 96, and 97).

The pressures and temperatures needed to dissolve a given polymer in CO₂ depend on the intermolecular forces between solvent-solvent, solvent-polymer segment, and polymer segment-segment pairs in solution and on the free volume difference between the polymer and CO₂, normally they are represented by rigorous and complicated expressions.

1.6. Permeability of Gases Through Flexbarrier

The permeation rate through the polymeric barrier is one of the most important parameters for the design of a flexible pipe ⁽⁹⁸⁾. The aim of this section is to demonstrate the complexity of the topic involving the permeability behavior of a polymer, concerning the number of parameters, which shall be considered, in order to predict the permeation rate of gases through a Flexbarrier layer in service. However it is important to reiterate that the Flexbarrier will be saturated with CO₂ or a mixture of gases in supercritical condition, considering the permeation rates of the mixture.

Gas permeation has been studied for over 150 years. However, significant advances in the comprehension of gas permeation through polymeric barriers have been made only in the last three decades. The interest in the field was generated from developments of new membrane applications ⁽¹⁰⁴⁾.

It is well known that the polymers used as Flexbarrier, in operating conditions, will be saturated with gases from the bore of the pipe. For the design of a flexible pipe, there are some tools based on numerical modeling, which can predict the concentrations of the retained gases considering the pipe configuration, gaps of carcass and Flexlok, temperature of the pipe bore, pressure, gas composition and other parameters. Such tools were developed based on tests applying segments of the pipe, comparing such results to the results acquired in small-scale labs tests.

The diffusion of small molecules into polymers is a function of both the polymer and the diffusant. Factors which influence diffusion include ⁽⁹⁹⁾: the molecular size and physical state of the diffusant ⁽¹⁰⁰⁾, the morphology of the polymer ⁽¹⁰¹⁾, the compatibility or solubility limit of the solute within the polymer matrix ⁽¹⁰²⁾, the volatility of the solute ⁽¹⁰³⁾, and the surface or interfacial energies of the monolayer films ⁽⁹⁹⁻¹⁰²⁾.

Researchers have attempted to identify specific mechanisms by which diffusion occurs in polymeric systems, but there is no general explanation to this phenomenon ⁽¹⁰³⁾.

Formulation of the gas transport phenomena through polymer membranes is directed in two areas: development of quantitative theories based on the thermodynamics and kinetic properties of the gas-polymer system ⁽⁹⁹⁾, and experimental study of gas transport through various polymers ⁽¹⁰⁰⁾. Most quantitative theories are primarily based on regular polymer solution theories. Empirical studies observe behaviors for gas-polymer systems and then correlate these findings to known phenomenological models. Based on the focus of these empirical studies, either microscopic (molecular) or macroscopic (continuum) theories are employed ⁽¹⁰⁴⁾.

There are two related parameters derived from Fick's first law can be measured. They assess the barrier properties of plastic films and similar materials. These properties are the permeability coefficient and the vapor transmission rate.

Fick's first law applies only to the gases that obey Henry's law on proportionality of penetrant solubility in the barrier to the partial pressure of the penetrant. Therefore, the permeability coefficient can be measured only for gases that become liquid at pressures and temperatures far from ambient conditions (1 atm and 0°C, respectively). These gases include air, oxygen, argon, and CO₂. There are other theories, which tie the permeation to the temperature of the media in general ⁽¹⁰⁴⁾.

Fick's first law states that the volume (V) of a substance that penetrates a barrier wall is directly proportional to the area (A) of the wall, partial pressure differential (p) of the penetrant, and time (t) and inversely proportional to the wall thickness (s), if the wall is homogeneous in the direction of the penetration. The coefficient P in the equation representing Fick's first law is the permeability coefficient, see Equation 1.1.

1.7. Characterization of Structure Gradients in Polymers after Mechanical Loading

In the literature there are abundant papers studying the structure-property-relationships of polymers after mechanical load. The methods can be split into two groups according to the applied structure-analysis techniques. The group including the techniques of direct observation of the structure in physical space, e.g. microscopy techniques and the group of the indirect observation by monitoring a parameter, e.g. by FT-IR, Solid-state NMR and X-ray scattering methods ⁽¹⁰⁵⁾.

X-ray scattering and diffraction are among the principal tools for studying polymers ⁽¹⁰⁶⁾. X-ray scattering is, probably, the most versatile method for structure-characterization during the deformation. This technique provides abundant information about structural variations from a molecular level up to several micrometers ^(107,108). Most techniques provide complementary information to X-ray scattering data and can often be applied in parallel with X-ray techniques.

The small-angle X-ray scattering SAXS regime reveals the typical nanostructures observed in semi-crystalline materials, thermoplastic elastomers, copolymers and multi-phase blends. The structure of lamellae-stacks ⁽¹⁰⁹⁻¹¹²⁾, orientation of lamellae ^(111,113,114), lamellae-distortion ⁽¹¹⁵⁾, crazing and yielding ^(115,116) can be studied in this region.

Microbeam scanning small-angle X-ray scattering generates micro-structure information as function of the scan coordinate in the space. The spatial resolution is given by the dimension of the microbeam.

Chapter II

SAXS Theory

'Anyone who has never made a mistake has never tried anything new.'

...Albert Einstein

2.1 X-ray Scattering

The application of X-ray scattering for the study of soft matter has a long tradition. By shining X-rays on a piece of material, representative structure information is collected in a scattered pattern. In addition, over the last three decades, X-ray scattering has gained new attractively because it has been developed from a static to a dynamic method ⁽¹⁰⁶⁾.

X-rays are electromagnetic waves of very short wavelength. The X-rays used in matter studies have wavelengths of about 0.01–10 nm. When waves of any kind are scattered from structures with which they interact, the angles of scatter are large when the lengths within the structure are comparable to the wavelength, and small when the lengths are large compared with the wavelength of the waves.

Two types of X-ray scattering experiments are therefore frequently used in the study of polymers; wide-angle X-ray scattering (WAXS), and small-angle X-ray scattering (SAXS), depending on the scale of the features studied ⁽¹¹⁷⁾. However, middle-angle X-ray scattering (MAXS) and ultra-small-angle X-ray scattering (USAXS) can also be used.

Classical X-ray diffraction and scattering is carried out in the sub-area of wide angle X-ray scattering, WAXS. The corresponding scattering patterns yield information on the arrangement of polymer-chain segments, e.g., orientation of

the amorphous phase, crystalline structure, size of crystals, crystal distortions, WAXS crystallinity.

The sub-areas of WAXS cover the characteristic scattering of liquid-crystalline structure and rigid-rod polymers. For example, intercalation of layered-silicates (clay) is studied in this region ⁽¹¹⁸⁾. In the literature, this angular region is often referred to as small-angle due to the similarities in data-analysis in both regions.

The SAXS regime reveals the typical nanostructures observed in semi-crystalline materials, thermoplastic elastomers, copolymers and multi-phase blends. The structure of lamellae-stacks ⁽¹⁰⁹⁻¹¹²⁾, orientation of lamellae ^(111,113,114), lamellae-distortion ⁽¹¹⁵⁾, crazing and yielding ^(115,116) can be studied in this region. SAXS tomography ^(119,120) is used to study structure gradients of polymer samples with fiber symmetry.

The USAXS extends the accessible structure towards the micrometer range ⁽¹²¹⁾.

In practice, with the variation of the sample-detector distance, it is possible to obtain good resolution in the desired angular region ⁽¹²²⁾. Equation 2.1 shows the relation between the length-scale of order d , radiation wavelength λ and scattering angle 2θ .

$$d = \frac{\lambda}{2 \sin \theta} \quad 2.1$$

2.2. Small Angle X-ray Scattering

SAXS is one of the few minimal non-destructive methods, which can be used to study structural changes that take place on a nanometer scale during fiber spinning or stretching of semi-crystalline or other multiphase polymer materials. Utilizing a synchrotron, as the most powerful X-radiation source and a high-resolution detector, enables the recording of detailed scattering patterns with high accuracy during short exposure times ⁽¹²³⁾.

SAXS experiments are often performed with apparatus that consists simply of a long box, at one end of which is a set of pinholes to collimate the X-ray beam from a generator and at the other end of which is a piece of film or a two-dimensional X-ray detector. The sample is placed in the X-ray beam near the collimator end and a beam-stop to block the direct, un-diffracted X-ray beam is placed near the film or detector. The box is usually evacuated to avoid scattering of the X-rays by air. More elaborate cameras are also sometimes used. Because of the long distance between sample and detector time-resolved, fast measurements are preferable carried out at synchrotron radiation sources.

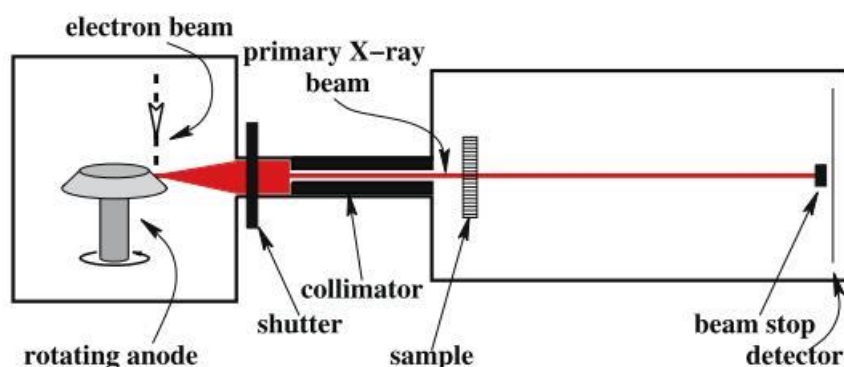


Figure 13 - Sketch of a laboratory setup comprising of a rotating anode, conventional beam sharpening optics, and an X-ray camera with the sample in normal-transmission geometry ⁽¹⁰⁶⁾.

The progress achieved currently on SAXS experiments is closely linked to the development of both powerful detectors and brilliant X-ray sources (synchrotron radiation, rotating anode).

Today, the structure evaluation can be tracked in-situ with a cycle time of less than a second. Moreover, if a polymer part is scanned by the X-ray beam of a microbeam setup, the variation of structure and orientation can be documented with a spatial resolution of 1 μm .

For the application of X-rays, no special sample preparation is required and as the beam may travel through air for at least several centimeters, manufacturing or ageing machinery can be integrated in the beamline with ease. Therefore, in-situ X-ray measurements are usually done at synchrotron radiation facilities. Details of a synchrotron radiation ring are presented in Figure 14.

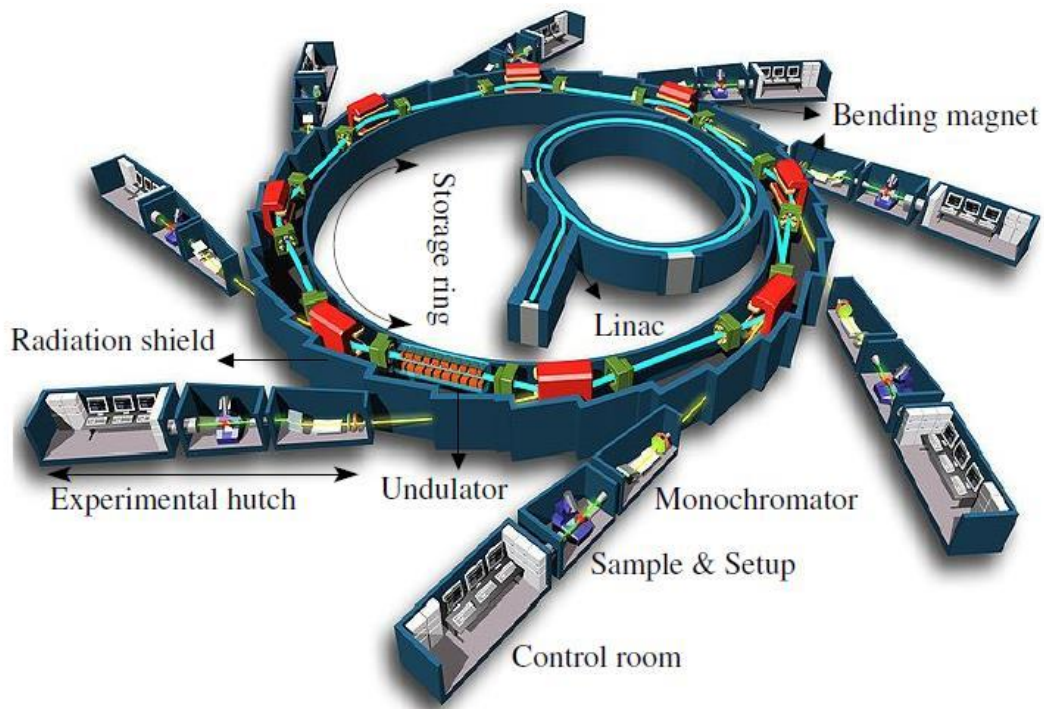


Figure 14 – Sketch of a typical synchrotron radiation ring for the application of technical X-rays ⁽¹⁰⁵⁾.

Figure 15 presents a schematic of the normal transmission setup, which is frequently used for in-situ X-ray scattering experiments ⁽¹²⁴⁾. The sample and detector are oriented at right angles (normal) with respect to the X-ray primary beam.

The primary beam penetrates a relatively thin sample (ca. 1-10 mm). The scattering intensity $I(x,y)$ is recorded by means of a planar detector in transmission mode.

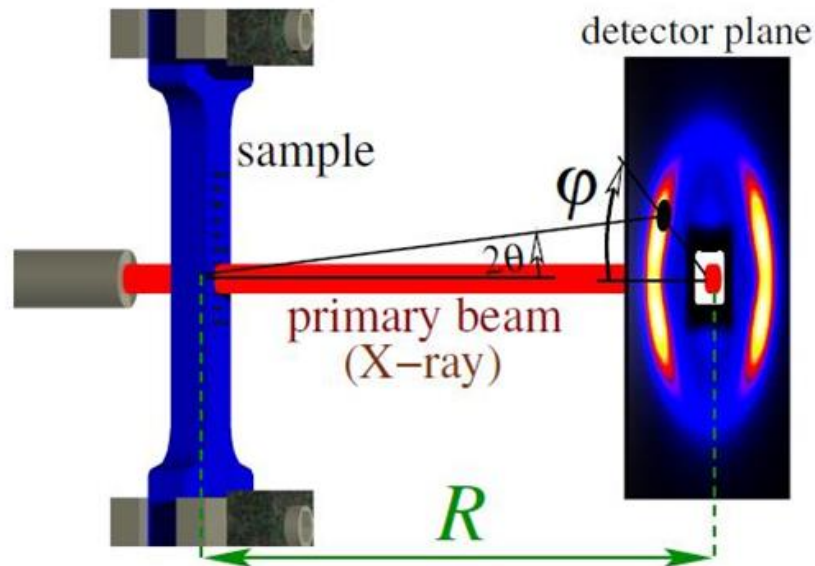


Figure 15 - Normal transmission setup of an X-ray scattering experiment. The intensity at a chosen point (circular mark) on the planar detector, $I(2\theta, \varphi)$ is a function of the scattering angle 2θ and the azimuthal angle φ . R is the sample-detector distance ⁽¹⁰⁵⁾.

The angular range of the recorded pattern is controlled by the sample-detector distance R . Equation 2.2 shows the relation between the scattering-related coordinates, $(2\theta, \varphi)$, and the pixel coordinates (x, y) on the detector with scattering angle 2θ , and azimuthal angle φ ⁽¹⁰⁵⁾.

$$\tan 2\theta = \frac{\sqrt{(x^2 + y^2)}}{R} \quad 2.2$$

$$\tan \varphi = y/x$$

As stated by the kinematic scattering theory, the relation between the structure of matter and the scattered intensity can be better understood, if the latter is treated in the so-called reciprocal space $\mathbf{s} = (s_1, s_2, s_3)$ ⁽¹⁰⁵⁾. See the relation in Equation 2.3.

$$I(2\theta, \varphi) \rightarrow I(\mathbf{s}) \quad 2.3$$

with $s_1 = x/(\lambda R)$, $s_2 = 0$, $s_3 = y/(\lambda R)$

In the case of isotropic scattering, the scattering intensity $I(\mathbf{s})$ is only a function of the modulus of the s-vector,

$$s = \sqrt{s_1^2 + s_2^2 + s_3^2} \quad 2.4$$

For a sample with fiber symmetry, rotating the sample about the fiber axis does not change the scattering pattern. Then $s_1 = s_2 = s_{12}$ is valid.

where $s_{12} = \sqrt{s_1^2 + s_2^2}$ is the transverse coordinate in cylindrical coordinates, and s_3 is the longitudinal coordinate of reciprocal space in the fiber direction. Thus, $I(\mathbf{s})$ is a function of s_{12} and s_3 only. A fiber symmetric material studied by SAXS using a 2D detector provides an excellent setup for in-situ monitoring of the structure evolution.

The PILATUS 1M detector is a hybrid pixel array detector with over one million pixels operating in single photon counting mode. The detector, designed for macromolecular crystallography, is the largest pixel array detector currently in use in a synchrotron and it has been demonstrated that single photon counting potentially provides data of superior quality.

When a monochromatic X-ray beam passes through some polymers, peaks of scattering are observed at angles 2θ of the order of 1° , or about a fiftieth of a radian, when the X-ray wavelength used is about 0.2 nm.

Figure 16 shows a SAXS pattern from a non-oriented polypropylene structure. The SAXS scattering is the dark ring-shaped reflection which is at its darkest equal to about half the side of the outer square. This diameter corresponds to approximately 1° .

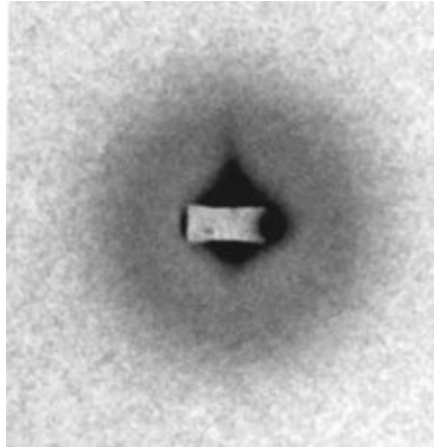


Figure 16 - Small-angle X-ray scattering from a non-oriented polypropylene. The SAXS scattering is the dark ring-shaped reflection of diameter at its darkest, equal to about half the side of the outer square. This diameter corresponds to approximately 1° .

The result of the scattering method is not a common image of the structure. There is no way in which to reconstruct it from scattering data, except for the cases in which either anomalous scattering is employed, or a diffraction diagram of an almost perfect lattice structure is recorded ⁽¹⁰⁶⁾.

If a polymer part is conventionally irradiated by an X-ray beam, the recorded pattern is an integral superposition of all the SAXS patterns emerging from the sequence of volume elements along the beam path. From the mathematical point of view, such a superposition is a projection. A single projection is of little use for the study of nanostructure gradients in materials. As a historical result, the material has been sliced mechanically ^(125,126), and every slice had to be studied using SAXS.

In an X-ray scattering experiment, we are interested in the relation of the measured scattering intensity to the structure inside the volume V that is irradiated by the X-ray beam. X-rays interact with the electrons of the materials, thus the structure is defined by the electron density $\rho(\mathbf{r})$. Here $\mathbf{r} = (r_1, r_2, r_3)$ is

the vector in real space. X-rays are scattered when $\rho(\mathbf{r})$ varies inside the irradiated volume. Thus phases without electron-density-contrast cannot be distinguished by means of X-ray scattering ⁽¹⁰⁵⁾.

The purpose of an in-situ X-ray measurement is to monitor the variation of the materials structure. Generally, the structure of polymers can be considered to be made from domains which can be discriminated easily from each other by a sufficient difference of their electron densities.

Examples are copolymers consisting of soft and hard domains, semi-crystalline polymers (crystalline phase is denser than the amorphous regions) and porosity (voids) within a material. In this case, it is advantageous to perform an edge enhancement by applying the Laplacian operator Δ , instead of directly studying the correlation function $P(\mathbf{r})$ ^(106,124). See equation 2.5.

$$z(\mathbf{r}) = P(\mathbf{r}). \quad 2.5$$

Here $z(\mathbf{r})$ is the chord distribution function (CDF).

The main challenge of such experiments is the huge number of recorded patterns. Moreover, the scattering data is recorded in the reciprocal space. Thus, direct analysis of the as-recorded patterns can be confusing or misleading. Therefore, a combination of theoretical tools that transform the scattering data from the reciprocal space into the real space and fast automated computer programs is required to obtain a thorough understanding of the structure evolution ⁽¹⁰⁵⁾.

2.2.1. The Magic Square

As mentioned in previous publications ⁽¹⁰⁶⁾, the fundamental relations between the electron density distribution inside the sample, $\rho(\mathbf{r})$, and the observed scattering intensity, $I(\mathbf{s})$ are conveniently combined in a sketch, which is known by the name “magic square of scattering” ⁽¹⁰⁶⁾. $A(\mathbf{s})$ is the scattering amplitude and $P(\mathbf{r})$ the Patterson function. See equation 2.6.

$$\begin{array}{ccc}
 \rho(\mathbf{r}) & \xleftrightarrow{\mathcal{F}_3} & A(\mathbf{s}) \\
 & \Leftrightarrow & \\
 \star 2 \Downarrow & & \Downarrow |||^2. \\
 P(\mathbf{r}) & \xleftrightarrow{\mathcal{F}_3} & I(\mathbf{s})
 \end{array} \tag{2.6}$$

Options of data analysis can be deduced from the magic square and our notions concerning the structure. As an example, let us consider the case of SAXS. Here it is, in general, assumed that the structure is described by a continuous density function. Although there is no way back from intensity to density, there are several options for data analysis:

1. Utilize theory and find out how some structure parameters can be determined from the intensity directly;
2. Walk from the intensity along the lower edge of the magic square (Eq. (2.8)) half-way back to real space, where the transformed data are closer to human perception;
3. Model a structure and fit it to the intensity; or
4. In addition to item 2, carry out 'edge enhancement' in order to visualize structure by means of the CDF, $z(\mathbf{r})$, and interpret or fit it.

For that, SAXS patterns can be evaluated by means of the multidimensional chord distribution function (CDF) method, introduced by N. Stribeck in 2001 ⁽¹⁰⁶⁾.

The CDF is an extension of the one-dimensional chord distribution called the interface distribution function (IDF), $g_1(r)$ originally proposed by Ruland ⁽¹²⁷⁻¹²⁹⁾ for the study of lamellar systems. The basic idea of this technique goes back to 1965, when Méring and Tchoubar ⁽¹³⁰⁻¹³³⁾ introduced the (radial) chord length distribution (CLD), $g(r)$.

2.2.1. Chord Distribution Function

CDFs computed from anisotropic scattering patterns visualize the multi-phase nanostructure information in direct space. The interpretation of a CDF is straightforward, since it has been defined ⁽¹³⁴⁾ by the Laplacian of Vonk's multi-dimensional correlation function ⁽¹³⁵⁾. Scattering patterns computed from simple model nanostructures (uncorrelated particles, microfibrils, lamellar stacks) yield the expected CDFs ⁽¹³⁴⁾. The CDF method has successfully been applied to the analysis of oriented semi-crystalline polymers ⁽¹²⁶⁾ and various thermoplastic elastomers studied during straining experiments ⁽¹³⁶⁻¹³⁹⁾. In the earlier studies, it has been compared to the classical method (discussion of peak position and shape as a function of strain or temperature).

As stated by Zeinolebadi ⁽¹⁰⁵⁾, the advantage of the CDF is that the only required assumption is a multi-phase structure ^(106,124). This assumption is correct for most polymeric materials. Thus, the structure of the material is revealed in real space without any adjusting parameters. The main prerequisites for computing the CDF are 'fiber symmetry' and completeness of the data.

2.2.1.1. Step 1: Projection on the Representative Plane

For the analysis of the structure, we are interested in a multidimensional image in real space, but not in a projection of the structural image ^(106,124). In reciprocal space, however, we have to perform a projection on the representative plane (s_1, s_3) of the fiber pattern, and compute

$$\{I\}_2(s_1, s_3) = 2 \int_0^{\infty} I\left(\sqrt{s_1^2 + s_2^2}, s_3\right) ds_2. \quad 2.7$$

This step has two advantages ^(106,124). See Equation 2.7. First, it converts the related visualization of structure from a smeared (projected) to a clear one. Second, it reduces noise in the pattern. The latter is due to the averaging nature of the integral. Thus, it makes it possible to decrease the exposure-time during experiment and increase the time resolution of an in-situ structure study.

2.2.1.2. Step 2: Laplacian and Background Correction

The next step of a proposed solution extracts the discrete scattering from the pattern ⁽¹³⁴⁾, which has already been subjected to the Laplacian in real space. For this purpose, first, an estimated density fluctuation background is subtracted. It is computed from the data points outside the inscribed circle of the image by the definition (Equation 2.8):

$$I_{Fl}(s_1, s_3) \approx c_0 + c_1 s_1^2 + c_3 s_3^2 \quad 2.8$$

This definition conforms to the rule that the density fluctuation background is expanded in even powers of the scattering vector ^(106,124). After the subtraction, the discrete intensity is multiplied by $4\pi^2 s^2$. This multiplication is equivalent to the Laplacian edge-enhancement operator, as is evidenced by the double application of the derivative theorem.

Now a correction for the non-ideal character of the multiphase topology must be performed. In the classical analysis this is a manual evaluation step which results in the subtraction of a slowly varying background ^(124,140,141). Here the background determination is replaced by the result of a low-pass filter, applied to the scattering image at the present state of evaluation ⁽¹⁴²⁾.

2.2.1.3. Step3: Fourier Transform

After background subtraction, an interference function $G_2(s_1, s_3)$ is obtained. Its 2D Fourier transform is the sought-after multidimensional chord distribution function. Because of fiber symmetry, the plane (r_1, r_3) is representative for the 3D structure, hence it is permitted to identify $r_1 \rightarrow r_{12}$. Thus $z(r_{12}, r_3)$ has been obtained. See equation 2.9.

$$I_{Fl}(s_1, s_3) = -\mathcal{F}_2(G_2(s_1, s_3)) \quad 2.9$$

with $\mathcal{F}_2()$ indicating the 2D Fourier transform. CDFs are computed from scattering data, which are anisotropic and complete in reciprocal space. Thus the minimum requirement is a 2D SAXS pattern of a material with fiber symmetry taken in normal transmission geometry⁽¹⁰⁶⁾.

As such, it shows the autocorrelation of the surfaces from the (nanometer size) domains in space in a similar manner as Ruland's interface distribution function does⁽¹²⁷⁻¹²⁹⁾ for one-dimensional structures as a function of distance. For samples with fiber symmetry, the CDF $z(r_{12}, r_3)$ is a function of two coordinates only (lateral direction r_{12} and fiber direction r_3). Therefore, it can be displayed in a plane. The height of the CDF signal is proportional to the area of *surface* contact between the domains of the nanostructure and those of its imagined displaced ghost as a function of the displacement, r .

The main steps from the recorded pattern towards the CDFs are schematically depicted in Figure 17. It shows a representative recorded SAXS pattern, the corrected fiber diagram $I(s_{12}, s_3)$, the absolute values of the corresponding CDF $z(r_{12}, r_3)$ and a slice of the CDF along the meridian, $z(0, r_3)$. Plotting and fitting the $z(0, r_3)$ curve is a simple way to analyze the structure along the principal axis (e.g. injection molding direction) of a material with uniaxial orientation⁽¹⁰⁵⁾.

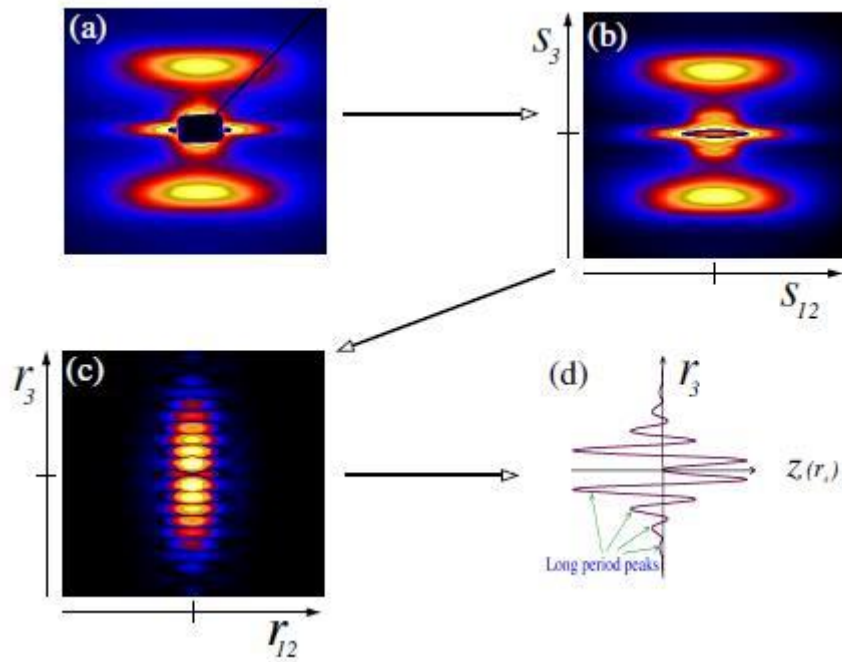


Figure 17 - Representative X-ray scattering data of oriented polymers (e.g. MFC precursors): (a) the recorded SAXS pattern. The blind area arises from the shadow of the primary beam-stop (b) the corrected fiber diagram $I(s_{12}, s_3)$, (c) absolute value of the CDF $|z(r_{12}, r_3)|$, and (d) a one-dimensional slice of the CDF along the meridian $z(0, r_3)$ showing the negative long period peaks and the positive peaks (above the r_3 -axis). Image intensities on logarithmic scale. Displayed regions: $-0.1 \text{ nm}^{-1} < s_{12}, s_3 < 0.1 \text{ nm}^{-1}$, $-100 \text{ nm} < r_{12}, r_3 < 100 \text{ nm}$. The s_3 - and r_3 -axes represent the orientation direction of the sample.

2.3. Objective

The objective of this thesis was to investigate the rearrangement of the microstructure of PVDF caused by exposure to supercritical CO₂ after rapid gas decompression.

For this purpose, a segment of a flexible pipe was exposed to a gas mixture with 75% CO₂ and 25% Methane, a temperature of 90°C and a pressure of 414 bar, followed by a rapid gas decompression operation.

From this segment of flexible pipe samples were retrieved for SAXS measurements, SEM investigations, density measurements and WAXS measurements. These investigations were performed in order to improve the understanding of the whitened regions encountered along the pipe segment. Virgin samples were also used as reference in this thesis.

In addition, a mid-scale test was also carried out as part of this thesis to measure the strain on the upper metallic layer, Flexlok, caused by the swelling of PVDF. Due to the failure experienced at the commencement of this test, a second mid-scale test shall be performed.

This thesis describes some of the changes in the polymer's microstructure caused by exposure to the supercritical CO₂.

These studies are of fundamentals importance, in order to better comprehend the effects of such conditions to PVDF used as Flexwear and Flexbarrier, as well as to ensure whether these layers can withstand to rapid gas decompression operations under these conditions. This research program is part of the various actual surveys in order to anticipate the challenges of the oil and gas industry.

Chapter III

Experimental

'Try not to become a man of success, but rather try to become a man of value'

...Albert Einstein

3.1. Exposition Test of PVDF to Supercritical CO₂

GE Oil & Gas has manufactured a flexible pipe with Flexwear and Flexbarrier layers in PVDF, in order to ascertain the influence of the supercritical fluids on the polymeric barrier, followed by a rapid gas decompression (RGD). RGD is a required test, as stated by the API 17J, for the qualification of polymers to be used as barriers in flexible pipes in the oil and gas industry. This is particularly important to assess the performance of the polymer during shut down operations.

The test was performed at 414 bar CO₂ (75/25% CO₂/methane, v/v) and 90°C. The sample has been kept at this condition for 1 month, time enough to soak Flexwear and Flexbarrier with CO₂/methane. This soaking time was calculated by internal tools of design of flexible pipes developed by GE Oil & Gas. The use of methane in this test was a client request, however the CO₂ is the focus of this thesis.

After one month, the sample was depressurized at a rate of -70 bar/min. Following the test, the sample was dissected for further investigations as detailed below. The sample was manufactured up to the Flexlok (metallic layer, right above the Flexbarrier) without sealing regions. The whole sample was subjected to the test environment, which does not represent the true application of a flexible pipe since in real applications, only the bore of the pipe is

pressurized with fluids and the Flexlok is only exposed to the permeated gases through the Flexbarrier.

3.2. Pipe Dissection and Specimens Retrieval

PVDF specimens for the SAXS measurements have been retrieved from the sample subjected to RGD from a supercritical environment. It is important to highlight that some of the Flexlok wires broke in the test, creating a damaged site on the sample, as observed in Figure 18 at the lower left side of the sample and circled in red. It is possible to observe the corrosion of the Flexlok wire along the entire sample. Flexlok is a metallic layer made of carbon steel and such breaks are not expected since, as explained above, in a real application, only the bore of the pipe is pressurized with the fluids and the severe corrosion of the Flexlok which contributed to the failure of that layer would not have been experienced.



Figure 18 – Segment of a flexible pipe manufactured up to Flexlok, with PVDF Flexwear and Flexbarrier subjected to a Rapid Gas Decompression test with Supercritical CO₂⁽¹⁶²⁾

During the dissection of the pipe segment, for the complete removal of the Flexlok wires, swelling of the Flexbarrier was observed in between the gaps of the Flexlok, creating some cusps.

In those swollen regions whitening of the PVDF was observed; such whitening was also observed in the damaged region. The level and the profile of whitening were not regular along the sample. The swelling and whitening was also observed for the Flexwear in between the gaps of the carcass, the innermost metallic layer.

Figure 19 shows the Flexbarrier after the complete removal of the Flexlok wires. Due to the presence of oils from the Flexlok and other residues from the test, Figure 19 does not clearly show the presence of the whitened regions along either the Flexbarrier, or the swollen surface.

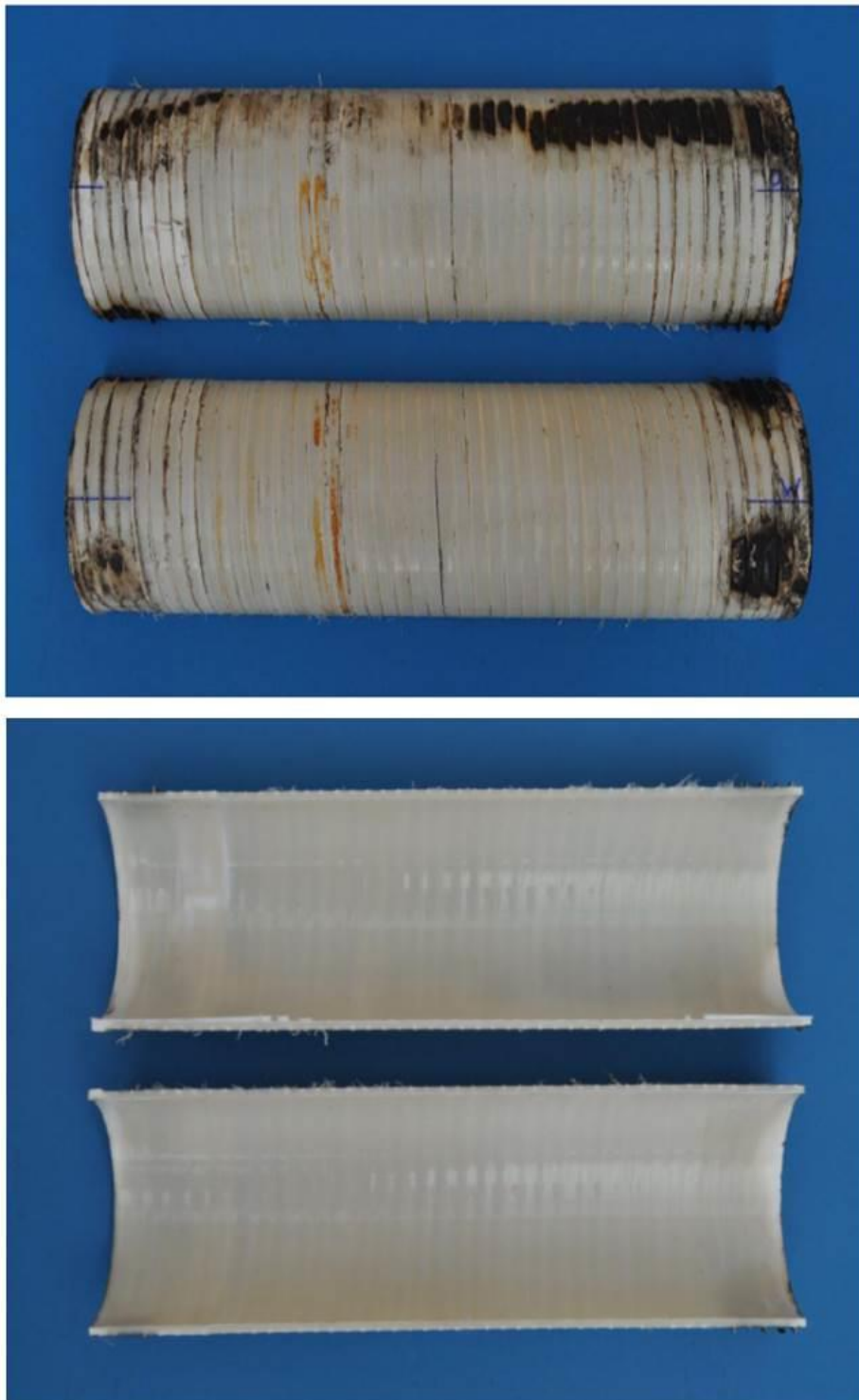


Figure 19 - Flexbarrier subjected to a rapid gas decompression test with supercritical CO_2 after the removal of the Flexlok. External surface (above) and inner surface (below) ⁽¹⁶²⁾

The swollen regions could be better observed along the Flexwear, as well as the whitening, see Figure 20. The whitening and the swelling occur in parallel lines along the body of the sample, on both the outer and inner surface.

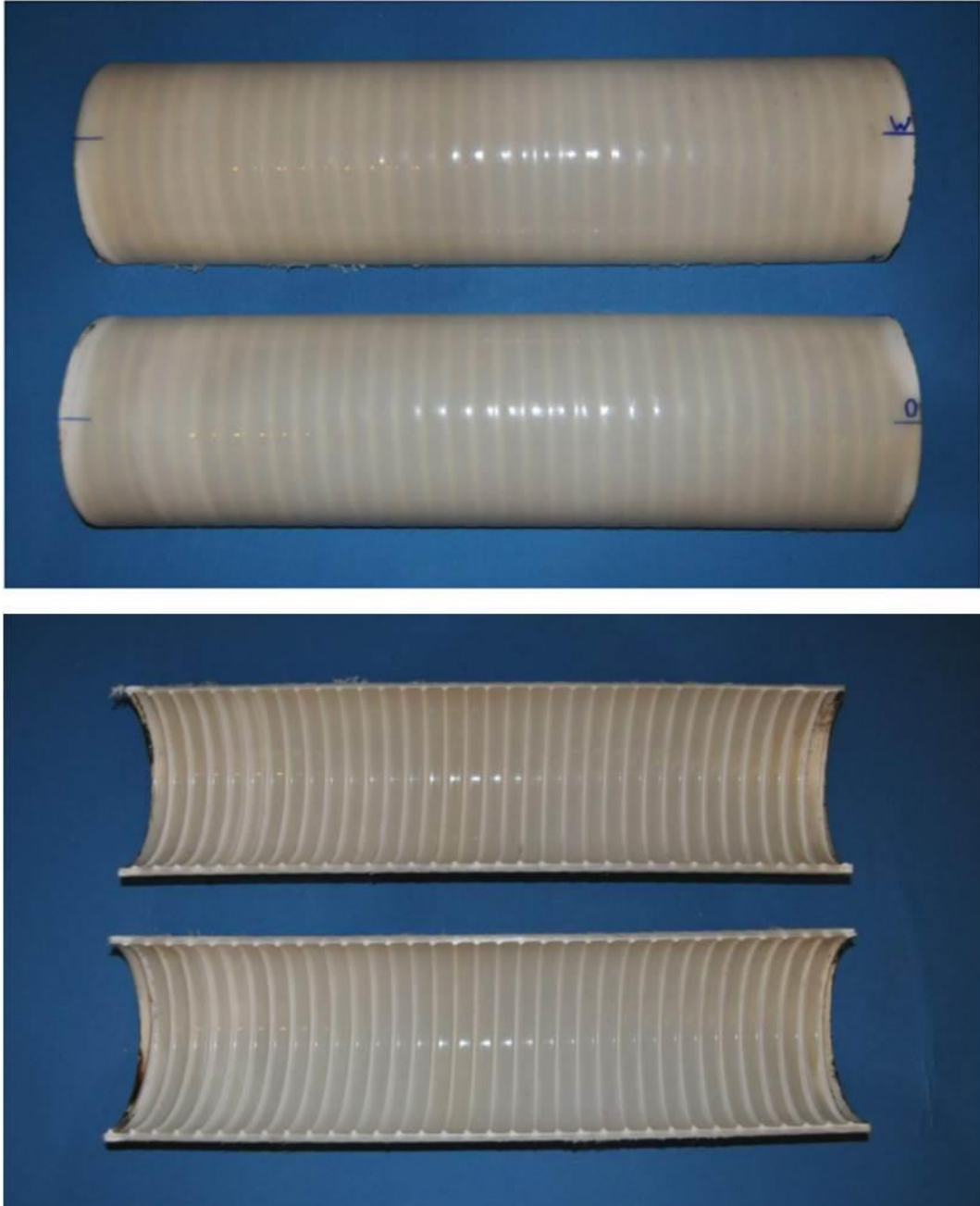


Figure 20 - Flexwear layer subjected to rapid gas decompression test with supercritical CO₂ presenting whitening in parallel lines along the body of the sample. External surface (above) and inner surface (below) ⁽¹⁶²⁾.

Figure 21 shows the carcass after the complete removal of the Flexbarrier and Flexwear. No corrosion was verified as this layer is made of stainless steel.



Figure 21 – Carcass subjected to rapid gas decompression test with supercritical CO₂. No corrosion was verified as this layer is made of stainless steel ⁽¹⁶²⁾

After the complete dissection of the pipe, samples were retrieved from the Flexwear and Flexbarrier, as detailed in the sequence.

Figure 22 shows the samples retrieved from the Flexbarrier, undamaged region identified as 1b, 1b-1 and 1b-2.

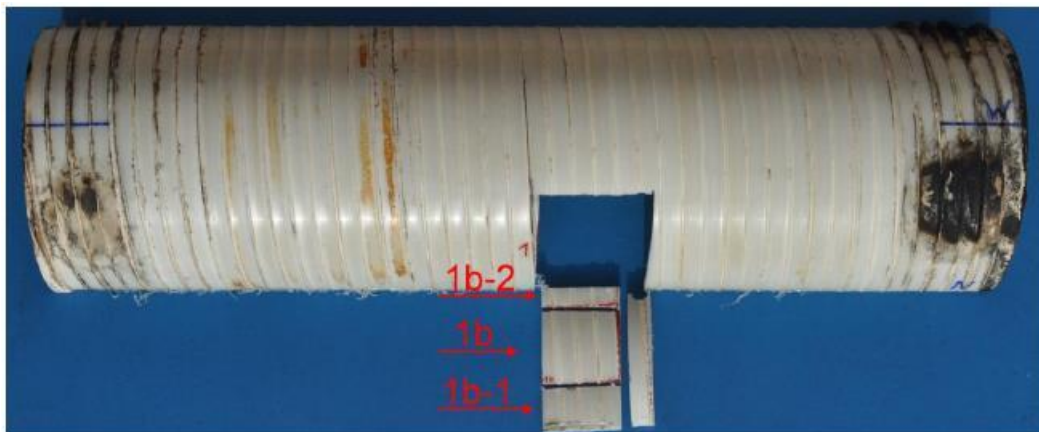


Figure 22 - Flexbarrier samples from the undamaged region. Samples used for SAXS, density and WAXS measurements ⁽¹⁶²⁾

Figure 23 shows the sample retrieved from the Flexbarrier damaged region identified as 2b.

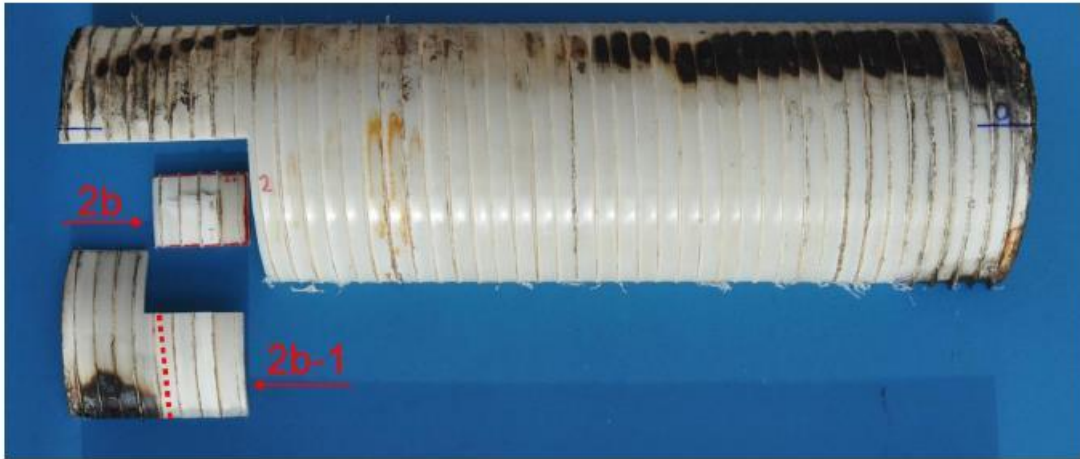


Figure 23 - Flexbarrier samples from the damaged region. Samples used for SAXS, density and WAXS measurements ⁽¹⁶²⁾

Figure 24 shows the sample retrieved from the Flexwear, undamaged region identified as 1w, 1w-1 and 1w-2.

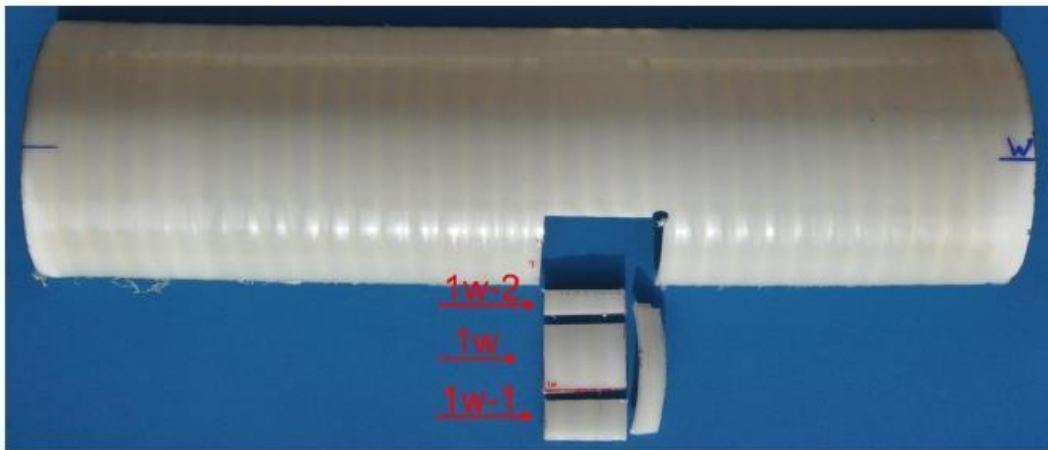


Figure 24 - Flexwear sample from the undamaged region. Samples used for SAXS, density and WAXS measurements ⁽¹⁶²⁾

Figure 25 shows the sample retrieved from the Flexwear, damaged region identified as 2w and 2w-1.

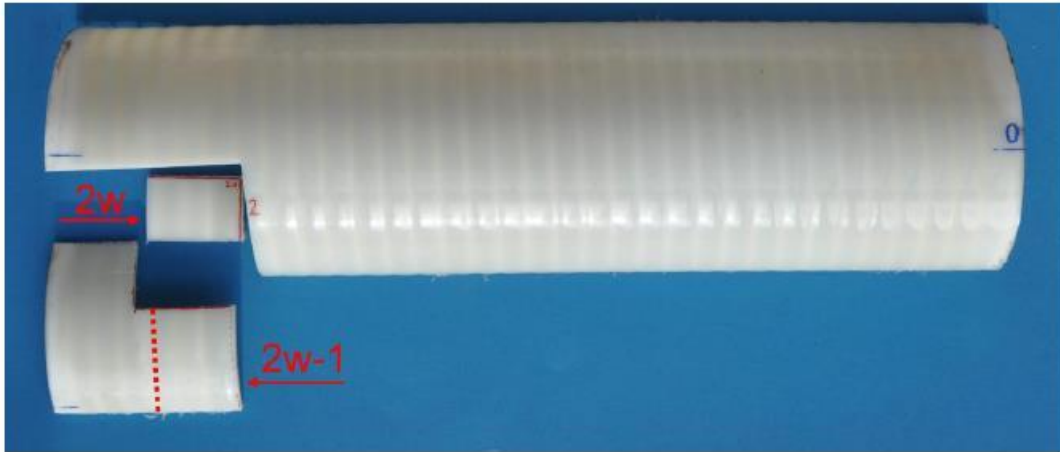


Figure 25 - Flexwear sample from the damaged region. Samples used for SAXS, density and WAXS measurements ⁽¹⁶²⁾

Figure 26 shows the profile, in general, of the swelling observed in both polymeric layers, Flexwear and Flexbarrier, out of the damaged region. It is possible to note the occurrence of whitening in these swollen regions. Flexwear placed (1w-1) on the upper side and Flexbarrier (1b1) below.

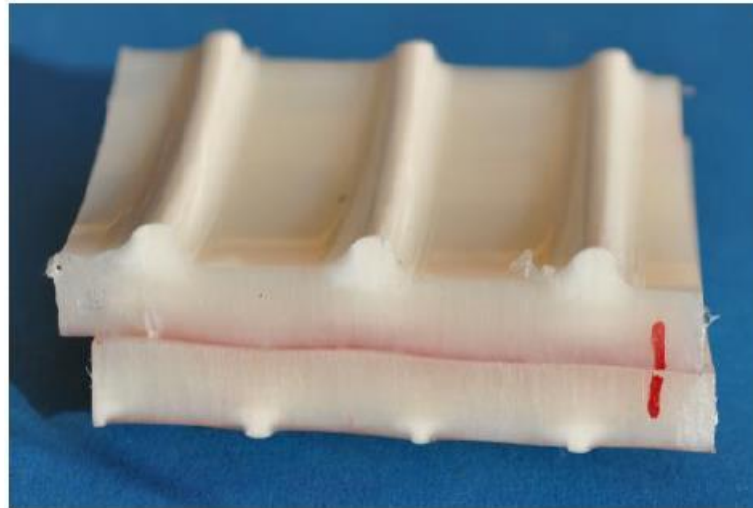


Figure 26 - Profile of the swollen PVDF in the noses regions. Also the whitening profile. Samples retrieved from the undamaged region. Flexwear (1w1) on the upper side and Flexbarrier (1b1) below ⁽¹⁶²⁾

From the samples above, 5 samples were selected for the SAXS measurements, being from damaged and undamaged regions of the Flexwear

and Flexbarrier, as shown in Table 4. A virgin PVDF sample was also used in this study for comparison reasons.

Table 4 – Detailing of Samples for SAXS

Sample Identification	Location
Virgin	-
2b1	Flexbarrier - Damaged
2b	Flexbarrier - Damaged
1b1	Flexbarrier - Undamaged
2w	Flexwear - Damaged
1w1	Flexwear - Undamaged

In the sequence, the samples were sliced with a thickness of 1 mm using a Buehler Isomet 4000 low-speed saw, as shown in Figure 27.



Figure 27 – Slicing process of the PVDF samples with a thickness of 1 mm using Buehler Isomet 4000 low-speed saw.

Figure 28 shows the profile of the swelling as well as the whitening of the Flexwear and Flexbarrier samples from the damaged and undamaged regions. See also in Figure 28 the identification of each sample from the left side to the right side. It is also possible to observe the surface of a PVDF virgin sample used in the SAXS measurements as a reference.



Figure 28 - Virgin PVDF; 2b1 – Flexbarrier sample from damaged region, 2b – Flexbarrier sample from damaged region, 1b1 – Flexbarrier sample from undamaged region, 2w – Flexwear sample from damaged region and 1w1 - Flexwear sample from undamaged region.

In addition, it is possible to observe the occurrence of whitening in the entire thickness of the 2b-1 specimens, being a Flexbarrier sample from the damaged region.

Specimen 2b, another Flexbarrier sample, also comes from the damaged region, albeit from a region less affected. Specimen 1b-1 presented whitening more restricted to the region of the gaps. This Flexbarrier specimen comes from an undamaged site.

The same observations were made on the Flexwear specimens, since the highest level of whitening observed for sample 2w was from the damaged region, propagating itself along the thickness of the specimens. Sample 1w-1 refers to an undamaged region also showing whitening, though more restricted to the gaps in between the carcass wires.

3.2.1.SAXS Measurements

SAXS was carried out on the synchrotron beamline P03 - PETRA III at HASYLAB, Hamburg, Germany with a micro-focus beam of size $38\ \mu\text{m} \times 19\ \mu\text{m}$. The X-ray path was perpendicular to the sample as shown in Figure 29. The sample distance used in the measurements was 2640 mm and the wavelength of radiation was $0.109\ \mu\text{m}$. Scattering patterns were collected by a two-dimensional PILATUS 1M detector (DECTRIS Ltd, Baden, Switzerland) with 981×1043 pixels (pixel size: $172\ \mu\text{m} \times 172\ \mu\text{m}$). The samples are translated through the microbeam stepwise, and SAXS patterns are recorded at each step. The step size in horizontal scans was $100\ \mu\text{m}$. Vertical scans have been performed with a step size of $30\ \mu\text{m}$. The exposure time is 10 s.

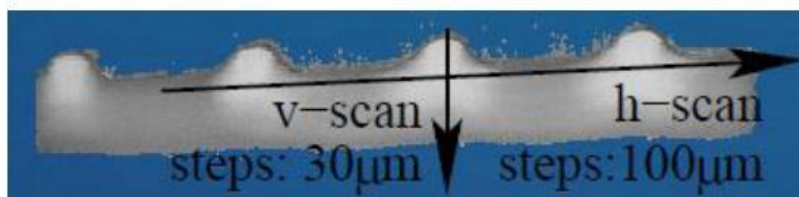


Figure 29 - PVDF with whitened zones for structure analysis by X-ray scattering. The direction of scans by an X-ray microbeam are indicated (vertical scans and horizontal scans).

Figure 30 presents details of synchrotron beamline P03 - PETRA III at HASYLAB, Hamburg, Germany. The images were recorded during the measurements of PVDF. Figure 31 presents the positioning of the sample on the synchrotron beamline P03 - PETRA III.

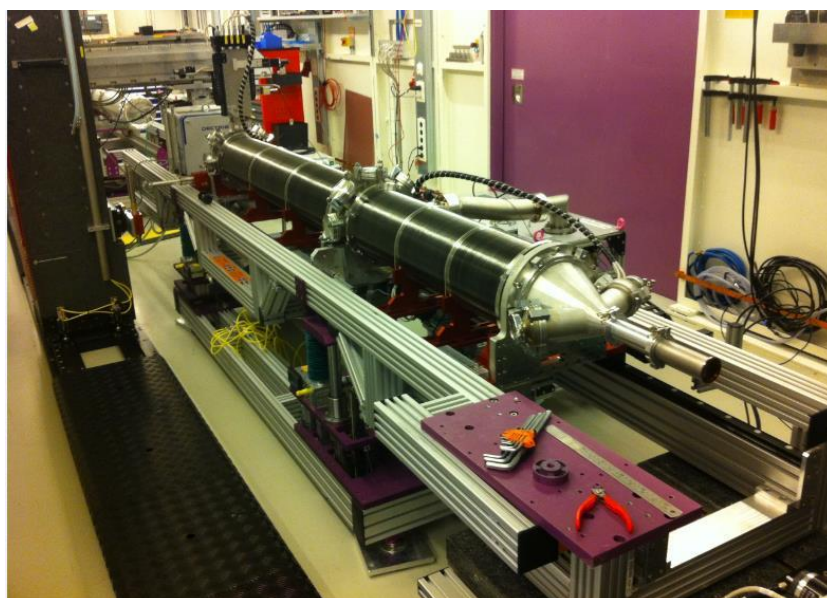


Figure 30 - Synchrotron beamline P03 - PETRA III.

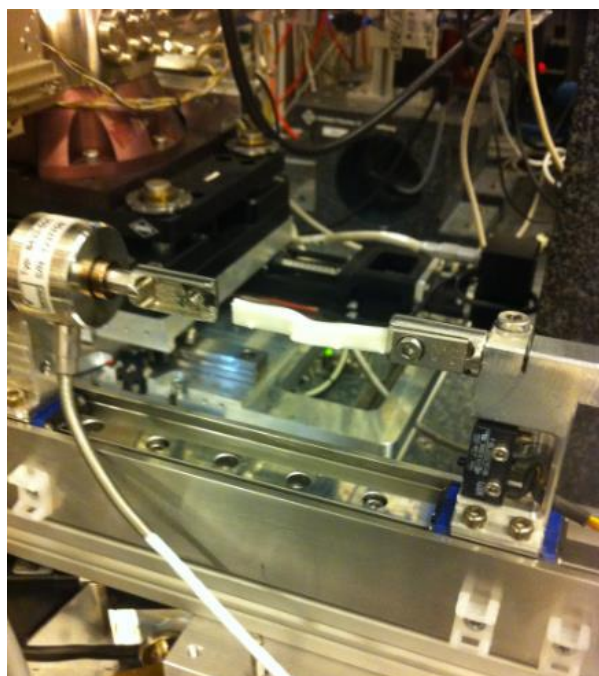


Figure 31 – Positioning of the sample on the synchrotron beamline P03 - PETRA III.

3.2.2.Characterization by SEM

As previously mentioned, samples of Flexwear and Flexbarrier from both the damaged region and undamaged regions were also observed via a scanning electron microscope (SEM). Table 5 shows the samples identification used for SEM observations. The images were recorded at 2 μm and 10 μm and the samples were prepared via freeze-fracturing method with Nitrogen. The measurements were completed by EVONIK using DIN EN ISO/IEC 17025 as standard, equipment - Fa. FEI Typ XL30 Sirion SFEG.

Table 5 – Detailing of the samples used for SEM investigation

Sample Identification	Location
Virgin	-
1b	Flexbarrier - Undamaged
1w	Flexwear - Undamaged
2b	Flexbarrier - Damaged
2w	Flexwear - Damaged

Figure 32 shows the 1b and 1w samples used for SEM, where the Flexlok was undamaged. Figure 33 shows a red line marking the location of the thin cuts.



Figure 32 – Specimens 1b and 1w used for SEM investigation from the undamaged region ⁽¹⁶²⁾

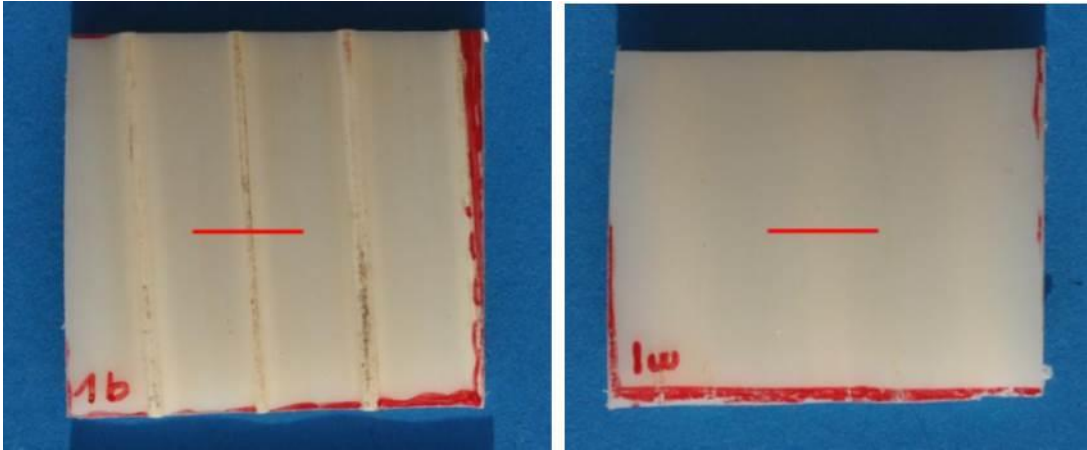


Figure 33 - Specimens 1b and 1w used for SEM investigation with a red line marking the location of the thin cuts ⁽¹⁶²⁾

Figure 34 shows the 2b and 2w samples used for SEM, where the Flexlok was damaged. Figure 35 shows a red line marking the location of the thin cuts.

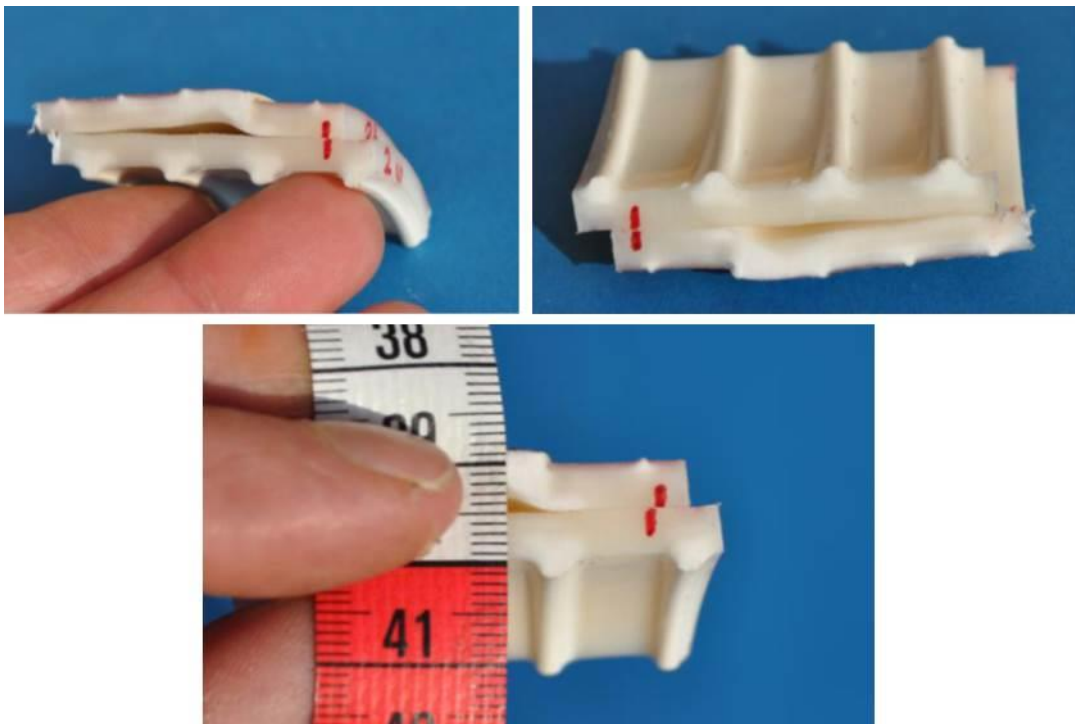


Figure 34 - Specimens 2b and 2w used for SEM investigation from the damaged region ⁽¹⁶²⁾.

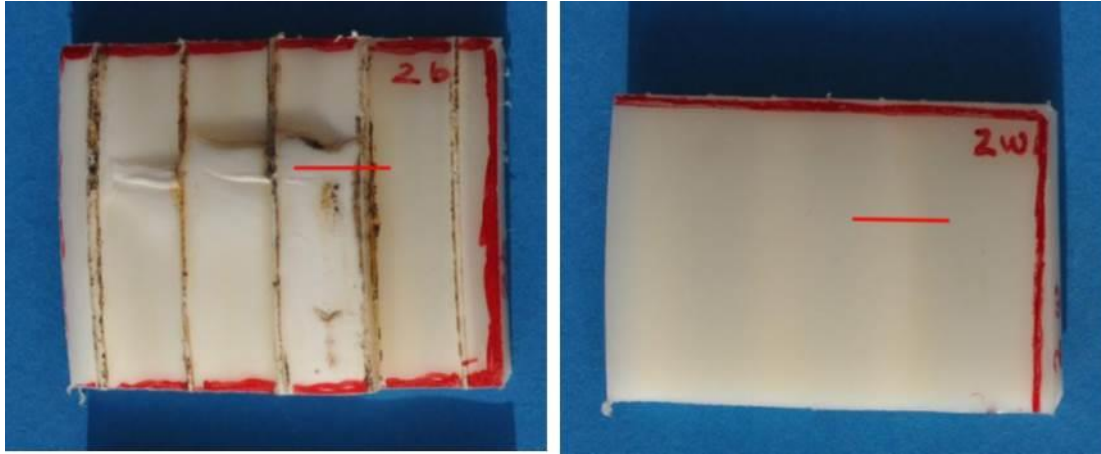


Figure 35 - Specimens 2b and 2w used for SEM investigation with a red line marking the location of the thin cuts ⁽¹⁶²⁾

3.3. Additional Samples for SAXS Measurements

Additionally, further investigations by SAXS were carried out for some samples acquired from different steps of the manufacturing process of the flexible pipes, in order to evaluate whether any PVDF rearrangement would be experienced. Such samples were not exposed to supercritical fluids; therefore only a qualitative evaluation was carried out. No quantitative evaluation was performed. Table 6 summarizes the manufacturing process from which these samples were acquired.

Table 6 – Further Samples

Sample Description	Condition	Sample Identification (SAXS)
C512 Flexbarrier	Pressured at 620bar with water at room temperature for 24h	512
C512 Flexwear	Pressured at 620bar with water at room temperature for 24h	512w
C327	Sealing Region	327

During the tests, only a vertical scan was carried out; see details of the each sample and positioning of the scan in Chapter IV.

SAXS was also carried out at the synchrotron beamline P03 - PETRA III at HASYLAB, Hamburg, Germany with a microfocus beam of size $38 \mu\text{m} \times 19 \mu\text{m}$. The X-ray path is perpendicular to the sample. The sample distance used in the measurements was of 2750 mm and the wavelength of radiation was $0.109 \mu\text{m}$. Scattering patterns were collected by a two-dimensional PILATUS 1M detector (DECTRIS Ltd, Baden, Switzerland) with 981×1043 pixels (pixel size: $172 \mu\text{m} \times 172 \mu\text{m}$). The samples are translated stepwise through the microbeam, and SAXS patterns are recorded at each step. The exposure time is 2s.

Figure 36 shows each sample before the cutting process to obtain the specimens for the SAXS measurements.



Figure 36 - Samples: C327 (left), C512 Flexbarrier (middle) and C512w Flexwear (right).

In the sequence, the samples were also sliced with a thickness of 1 mm using a Buehler Isomet 4000 low-speed saw. For these samples 512w and 512, no visual indication of whitening was observed along the sample. However, some visual whitening was observed for C327 sample.

3.4. Mid-scale Swelling Test

After the execution of the test, as described in Section 3.1, and based on the acquired outcomes in terms of swelling of the Flexbarrier, it was necessary to carry out a mid-scale test under supercritical CO₂ conditions, as a concern relating to the effects of the swelling of the Flexbarrier on the Flexlok had been raised. The aim of the test was to measure the strains caused by the swelling of PVDF, in a fully constrained sample, reproducing the actual service conditions expected for a flexible pipe. This test is also part of this thesis.

The test was performed at 414 bar, 90°C and 100% CO₂, to measure the strains caused by the swelling of the PVDF, being the operating condition of some flexible pipes to be used in pre-salt. GE Oil & Gas has developed a concept of a mid-scale test, which is presented and detailed in this section.

As the test sample was manufactured up to Flexlok only, it was necessary to design adapted end caps to provide the complete sealing of the bore of the sample. Both end caps, one at each end of the sample, were linked to each other by means of 12 external steel bars, which were also responsible for providing axial resistance of the pipe against the loads generated by the internal pressurization of the sample.

The sample had a total length of 1000 ± 50 mm and was also assembled with same strain gauges to register the strains generated by the swelling of the Flexbarrier. An external shell was also used to protect the whole sample; a sketch of the sample is presented in Figure 37.

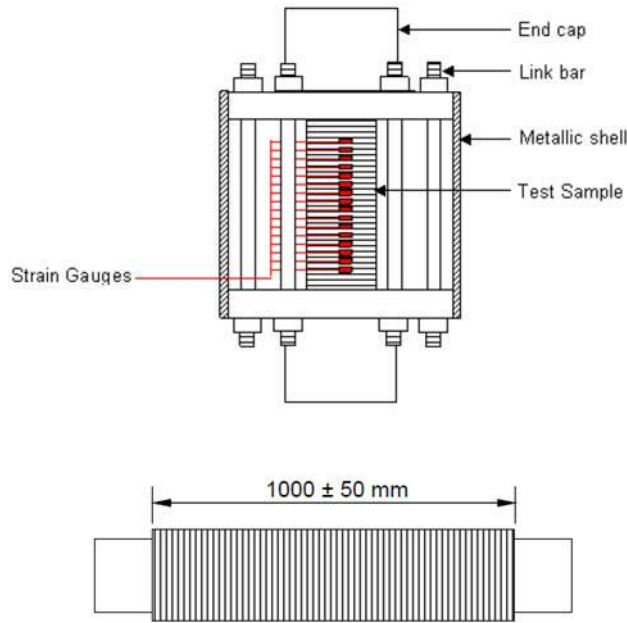


Figure 37 – General view of the sample used for the mid-scale test to measure the levels of swelling of PVDF on the Flexlok.

After the complete assembly of each end cap, strain gauges were bonded over the external surface of the Flexlok, to allow the monitoring of the strains generated during the pressurization of the sample bore with CO₂. The strain gauges were equally distributed along the sample. A minimum of 20 strain gauges were used for the monitoring of the strains. Groups of four strain gauges were used for the monitoring of the strains. Groups of four strain gauges, at every 90° (at the 'compass points' N, E, S, W), were equally distributed in five positions along the sample, as represented in Figure 38. The strain gauges were calibrated by pressurizing the sample with water before the execution of the test.

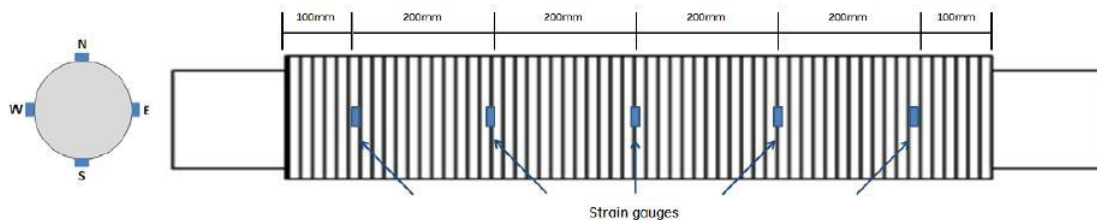


Figure 38 – General view of the positioning of the strain gauges along the sample in order to measure the strains generated with the pressurization of the bore of the sample with supercritical CO₂

Both, the sample internal pressure and temperature should be registered by the strain gauges. The data acquisition frequency should be adequate to monitor each test phase, such as: sample pressurization until 414 bar with CO₂, Flexbarrier soaking time at 414 bar for 30 days with CO₂, 10 rapid gas decompression cycles and 30 days for the degassing of the Flexbarrier.

For this test, 10 cycles of rapid depressurization with a minimum decompression rate of -70 bar/min were required. The hold period after each cycle (dwell time) should be of 1one hour before the next pressurization. The hold period after re-pressurization shall be of 24 hours before each decompression cycle. Figure 39 shows the Flexlok with some attached strain gauges before the installation of the external steel bars, as well as before the insertion of the external shell. Figure 40 shows the sample after the insertion of the external shell ready for delivery at the lab in charge of the execution of the test.



Figure 39 – General view of the sample before the installation of the external steel bars, as well as the insertion of the external shell. General view of some strain gauges along the pipe.



Figure 40 – General view of the sample after the insertion of the external shell.

The sample was assembled by GE in Rio de Janeiro in November 2012 and delivered to Eurotechnica in Germany in December 2012. The test was initiated by Eurotechnica in April 2013. Figure 41a shows the sample inside the tank. The tank was filled with water. The water was used to heat up the sample to 90°C. Figure 41b shows the tank already closed and filled with water. Figure 41c shows the connections used to pressurize the bore of the sample with supercritical CO₂.



Figure 41 – Figure 41a - Sample inside of tank before being filled with water. Figure 41b - Tank already closed and filled with water just before the test. Figure 41c - Connections used to pressurize the bore of the sample with supercritical CO₂.

Figure 42a shows the temperature monitoring system at 90°C before the test. Figure 42b shows the pressure monitoring system before pressurization of the bore sample. Figure 42c shows the strain gauges reading just after the pressurization of the bore sample with supercritical CO₂.



Figure 42 – 42a - Temperature monitoring system at 90°C before the test. Figure 42b - Pressure monitoring system before pressurization of the sample. Figure 42c - Strain gauges reading just after the pressurization of the bore of the sample with supercritical CO₂.

Chapter IV

Results and Discussions

'Insanity: doing the same thing over and over again and expecting different results.'

...Albert Einstein

4.1. Data Evaluation

Firstly, it is important to highlight that PV-WAVE is a comprehensive software environment that integrates state-of-the-art graphical and numerical analysis techniques into a system that is easy to use, easy to extend, easy to apply and easy to learn. PV-WAVE provides the tools we need to find solutions to build applications for complex technical problems ⁽¹⁴³⁾. It is software which provides many kinds of visual data analyses through 2D and 3D plotting.

PV-WAVE provides routines for plotting data in a variety of ways. These routines allow general X versus Y plots, contouring, mesh surface plots, perspective plotting and data clipping in an extremely flexible matter without requiring complicated programs. Such plotting allows the easier visualization of data during the analysis. PV-WAVE was the programming language used in this research, in order to characterize the whitening in the nose regions of PVDF.

Computer programming is required in this case due to the large number of recorded patterns, which are acquired during the SAXS measurements. Most computer programs run automatically after adjustment to the actual experimental conditions. In some programs the users have to define a region of interest (ROI) on the first image and afterwards the program runs automatically.

Evaluation of the SAXS patterns consists of three main stages. Stage I includes

pre-evaluation of raw data whilst in stage II the fiber diagrams, CDFs and scattering power are computed. Stage III includes peak-analysis of the CDFs (or SAXS patterns) and extracting the desired nanostructural parameters ⁽¹⁰⁵⁾. All steps about the evaluation of such data have been reported by Stribeck ⁽¹⁰⁶⁾.

These steps of data evaluation are illustrated in Figure 43. Figure 43a demonstrates the result of pattern harmonization. Blind areas have been filled from symmetry considerations and the data in each quadrant has been averaged. Figure 43b shows the scattering intensity $I(\mathbf{s}_{12}, \mathbf{s}_3)$ after filling the remnant central hole by 2D extrapolation utilizing radial basis functions ⁽¹⁴⁴⁾. This pattern is the fundament of a model-free nanostructure visualization and analysis in real space.

For nanostructure analysis we anticipate the study of a real-space function that is a slice but not a projection and bear in mind that in reciprocal space the fiber symmetrical function $I(\mathbf{s}_{12}, \mathbf{s}_3)$ may be considered as a slice, e.g., $I(\mathbf{s}_1, \mathbf{s}_3)$. Utilizing the Fourier-slice theorem we thus prepare to study a real-space slice by projecting in reciprocal space. See Equation 2.7.

The result is shown in Figure 43c. A 2D Fourier transform of this projected function would be proportional to a 2D slice of the multidimensional correlation function, $\gamma(\mathbf{r}_{12}, \mathbf{r}_3)$.

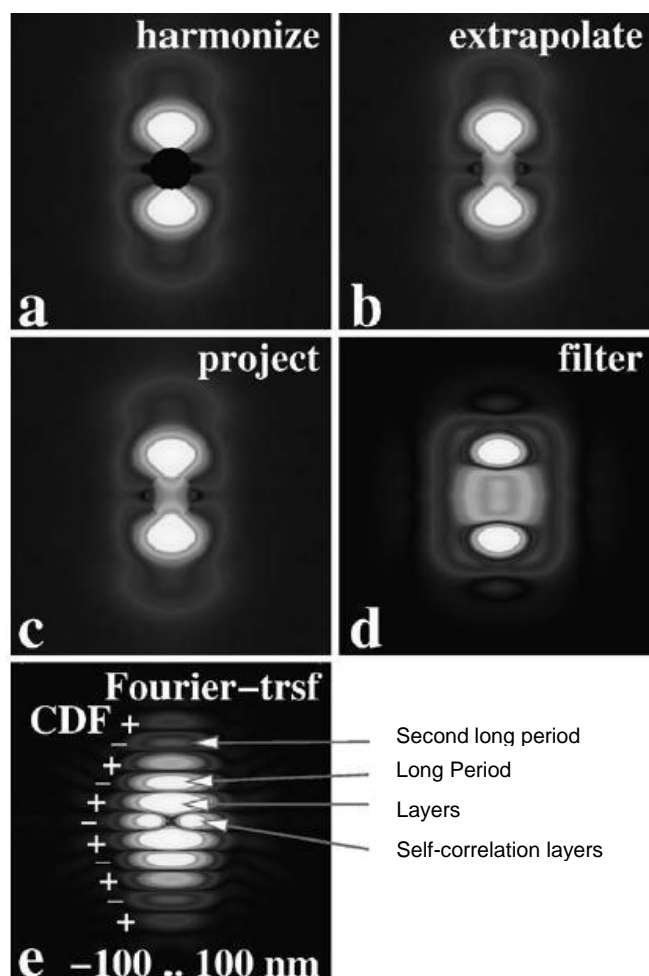


Figure 43 - Conversion of SAXS to CDF. All pseudocolor data on logarithmic intensity scale. (a–d) shows the region $-0.15 \text{ nm}^{-1} \leq s_{12}, s_3 \leq 0.15 \text{ nm}^{-1}$. Fiber axis (s_3) is vertical. (a) SAXS after filling blind areas. (b) After filling the center by 2D extrapolation. (c) Projection on the representative fiber plane. (d) Interference function (absolute values shown) by spatial frequency filtering. (e) CDF (absolute values; original sign of peaks labeled) by 2D Fourier transform. Some characteristics of the nanometer size layer system are indicated. The horizontal extension of the self-correlation layer is a measure of the extension of the lamellae from inside the voxel.

The interference function requires background subtraction according to Porod's law. In the multidimensional case the background is suitably defined by low-pass spatial frequency filtering of the pattern obtained so far ⁽¹³⁴⁾. The determined background is subtracted. In principle, this process of filtering and subtraction may be iterated until the integral of the determined interference function vanishes. Such a recursion should be avoided if possible as it eliminates the effects of domain surface roughness and erases the scattering

effect of small domains from the CDF. Nevertheless, the first application of the filter rarely returns a proper function that vanishes. Thus, in general, we apply the low-pass filter twice, and the interference function $G(\mathbf{s}_{12}, \mathbf{s}_3)$ is obtained. Finally, the multidimensional CDF is received by a 2D Fourier transformation. Figure 37(e) shows $|z(\mathbf{r}_{12}, \mathbf{r}_3)|$ in a pseudocolor representation on a logarithmic scale. The map fills a volume of reciprocal space equivalent to $-100 \text{ nm} < \mathbf{r}_{12}, \mathbf{r}_3 < 100 \text{ nm}$, see Equation 2.9.

In this thesis, the procedure *do_h2harm.pro* has been written and applied.

4.2. Virgin PVDF

A single shot has been performed for the evaluation of the virgin PVDF by SAXS. The polymer layer showed itself as an isotropic structure. Figure 44 shows the scattering on a logarithmic intensity scale, both in a surface plot and in a pseudo-color map. The strong annular wall is the long period peak, which indicates in PVDF an isotropic, well-developed semi-crystalline lamellae stack structure.

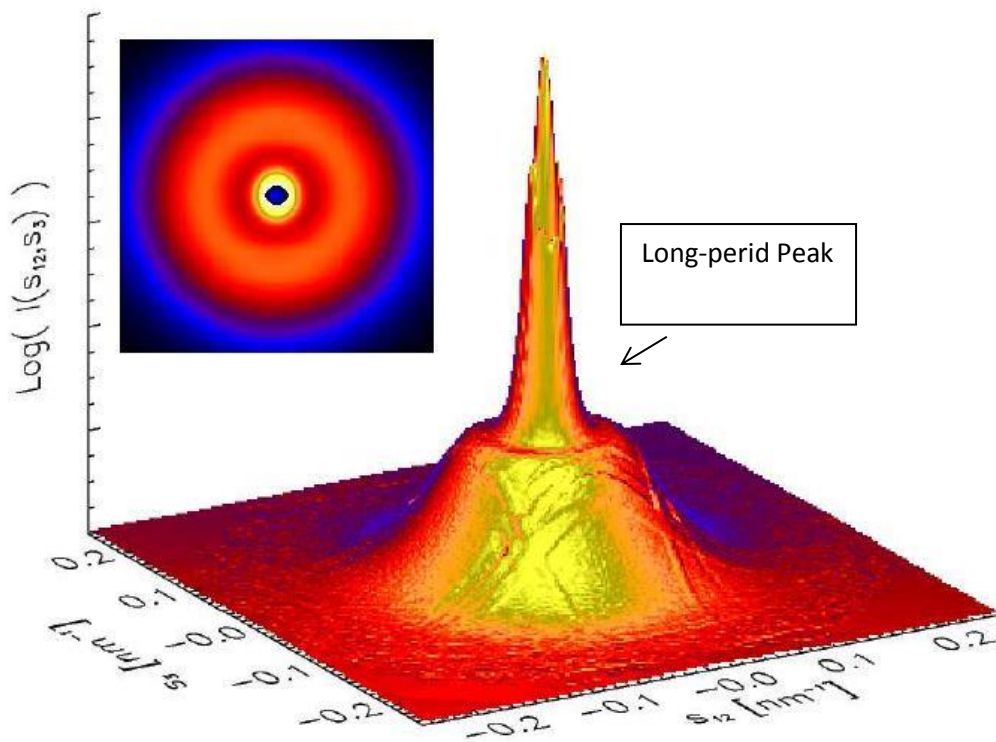


Figure 44 - PVDF from virgin pipe. SAXS intensity $I(s_{12}, s_3)$, $-0.25\text{nm}^{-1} \leq s_{12}, s_3 \leq 0.25\text{nm}^{-1}$ on a logarithmic scale. The inset shows the same data in the pseudo-color representation used in following figures.

Figure 45 shows SEM-micrographs of the virgin PVDF. The virgin material reveals spherical particles with a diameter of about 0.5 to 1 μm , which are bonded to the matrix of PVDF material. Such spherical particles are made up of PE to improve the quality of the extrusion of the material during the manufacturing of the flexible pipes. It is also possible to observe the absence of voids and crazes.

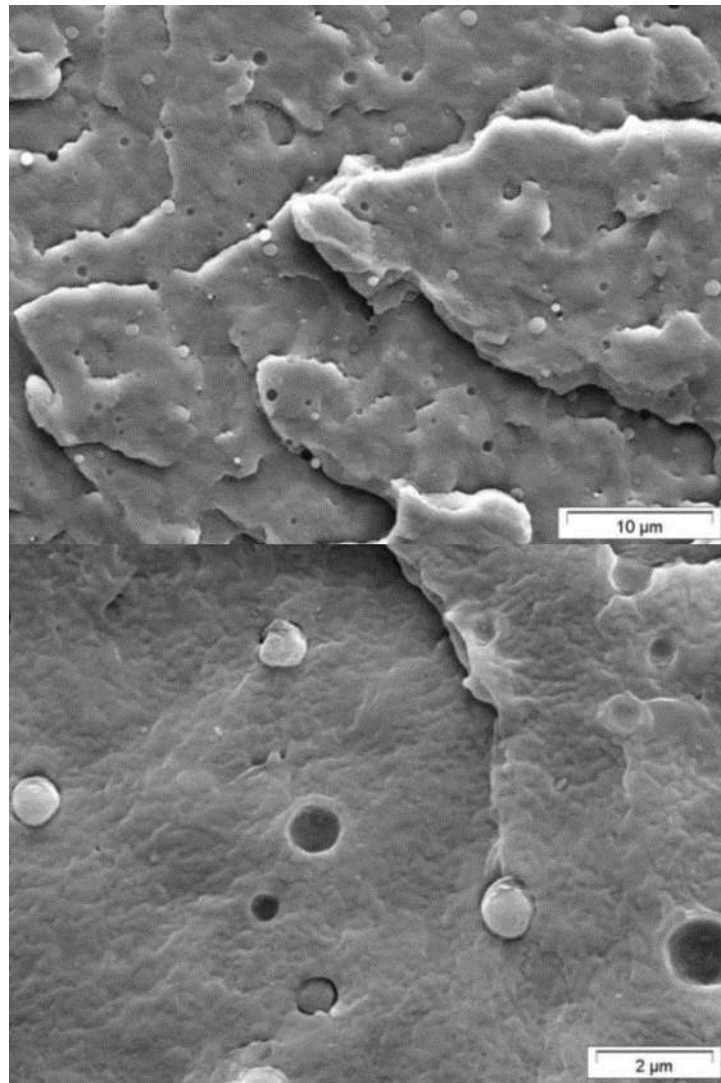


Figure 45 - SEM micrographs of virgin PVDF – top image at low magnification and bottom image at high magnification. There is no indication of voids and crazes ⁽¹⁶²⁾.

4.3. SAXS Results for PVDF Samples Exposed to Supercritical CO₂

4.3.1. Vertical Scans

After the RGD test, the PVDF layers appear significantly changed as the material has swollen into the gaps of the metallic carcass and the Flexlok, where it has formed some whitened noses, as shown in chapter III.

SAXS patterns of micro-beam scans through the noses show the change of the nanostructure of PVDF. Figure 46 shows the pseudo-color map of the scattering on a logarithmic intensity scale done in a whitened region of sample 2b. The type of peak indicates a oriented PVDF material.

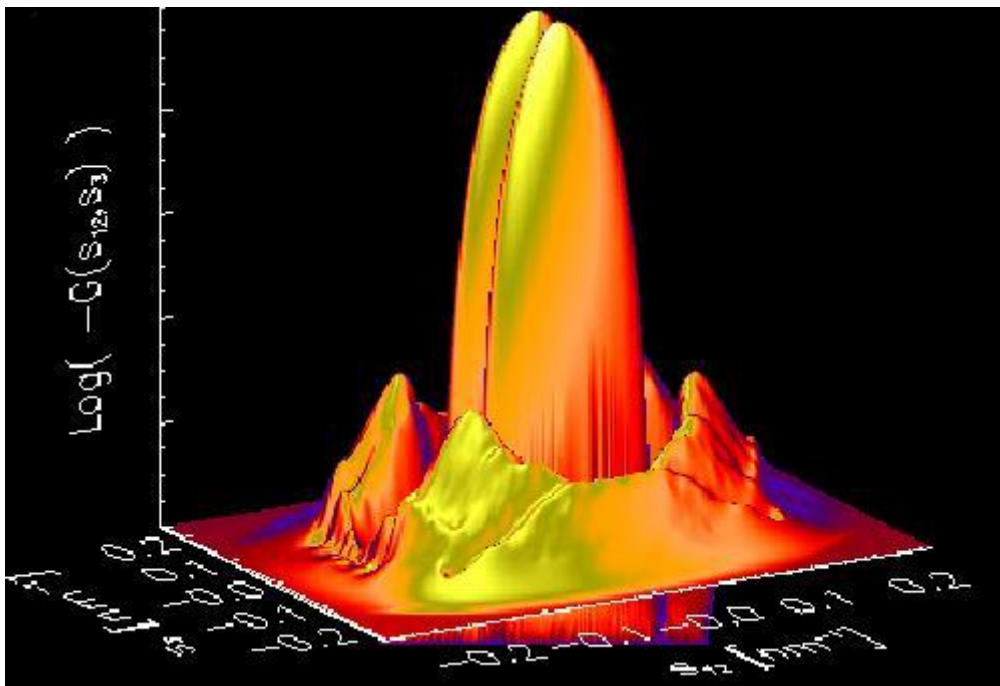


Figure 46 - PVDF from 2b sample, Flexbarrier from the damaged region. SAXS intensity $I(s_{12}, s_3)$, $-0.25\text{nm}^{-1} \leq s_{12}, s_3 \leq 0.25\text{nm}^{-1}$ on a logarithmic scale.

Firstly the scans of the samples 1w and 1b (from the undamaged region) will be discussed. Figure 47 shows the real disposition of Flexwear (1w) and Flexbarrier (1b) in a flexible pipe. Figure 47 also shows the whitening encountered in the regions of the gaps of Flexlok and carcass once more.

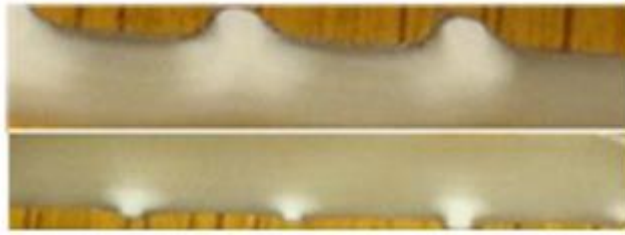


Figure 47 - Disposition of each layer in a flexible pipe. Above: Flexwear – 1w and below: Flexbarrier – 1b.

Figure 48 and Figure 49 respectively show the positioning of the 1b and 1w sample during the scanning by SAXS.

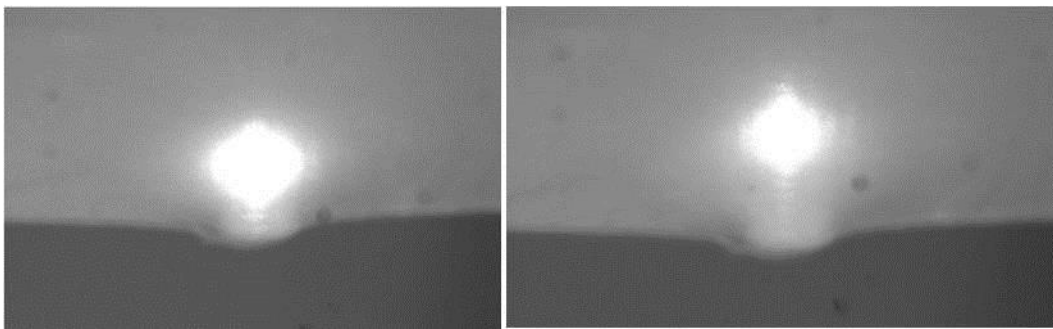


Figure 48 - Positioning of the 1b sample during the scanning by SAXS. Left: horizontal scanning; right: vertical scanning.

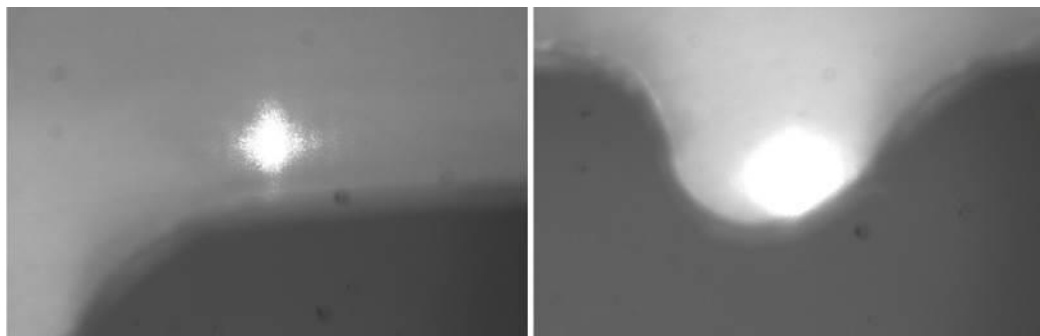


Figure 49 - Positioning of the 1w sample during the scanning by SAXS. Left: horizontal scanning; right: vertical scanning.

Figure 50 shows the selected patterns from vertical micro-beam scans through the center of the noses. The patterns shown in the top row of Figure 50 were taken close to the edge of the nose-whitened region. The patterns in the bottom row are from the opposite edge of the scanned layer.

The numerical labels indicate the distance from the nose-tip in units of micrometers. All the patterns are normalized to identical flux and identical irradiated volume. They are on the same logarithmic intensity scale.

The lower images of the 1w and 1b layers are very similar as expected, since these surfaces are in close contact with each other. Moving upward from the edge of the layers towards the nose, the pattern changes fundamentally as the whitened region is entered. In its center the intensity increases taking the shape of a rather diffuse equatorial streak. It is commonly identified as void scattering⁽¹⁴⁵⁻¹⁴⁸⁾. In other words, the contact region between the Flexwear and the Flexlok; no voids were encountered as the pattern showed itself as an isotropic structure.

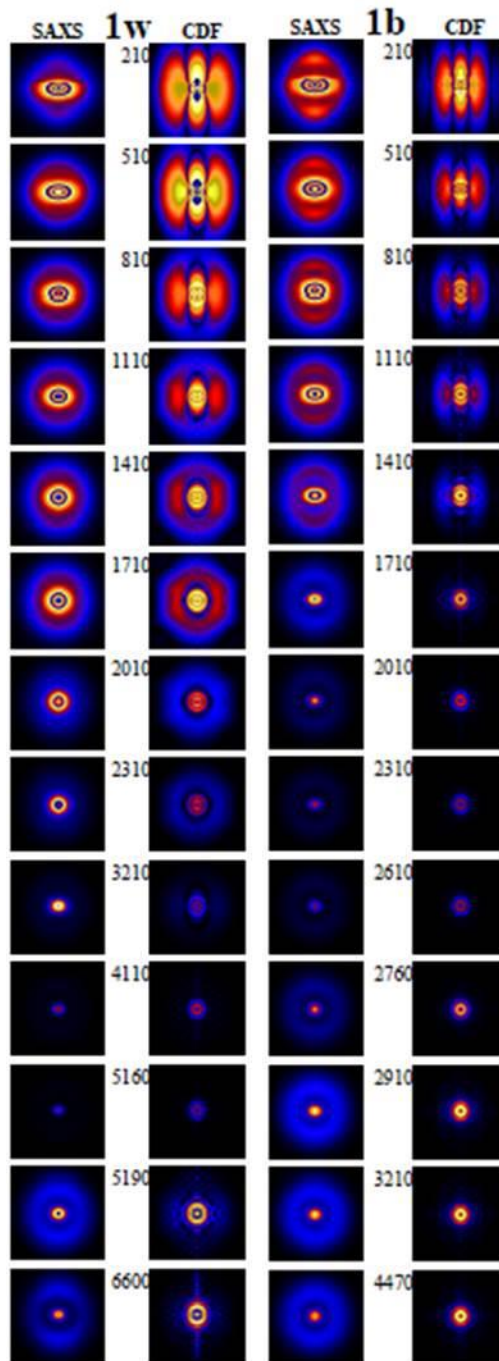


Figure 50 - 1w and 1b vertical SAXS scans of the tested pipe. Numbers indicate the depth in μm below the embossment tip. The bottom patterns are from the opposite edges of the layers. The axes of the fiber patterns are turned vertical by convention. With respect to the scan direction they have been perpendicular. Each double-column shows the SAXS intensity $I(s_{12}, s_3)$, $-0.15 \text{ nm}^{-1} \leq s_{12}, s_3 \leq 0.15 \text{ nm}^{-1}$ on identical logarithmic scale and the CDF $z(r_{12}, r_3)$ in the range $-75 \mu\text{m} \leq r_{12}, r_3 \leq 75 \mu\text{m}$.

Further out, the ring-shaped long-period peak of the lamellar two-phase system deforms. It gradually turns into two distinct reflections. In the top patterns the lateral extension of the reflections (Figure 50) may be taken as an indication that the crystalline domains are not extended lamellae, and the strain-induced conversion into microfibrils ⁽¹⁴⁹⁻¹⁵²⁾ has already set in.

The principal axis of the SAXS pattern indicates the direction in which the polymer has been strained from the cold flow. It is perpendicular to the scanning direction (Figure 55). Such a rearrangement with orientation is frequently observed when thermoplastic polymers are cold-drawn ⁽¹⁵²⁾.

Figure 51 shows the real disposition of the Flexwear (2w) and Flexbarrier (2b) (from the damaged region) in the flexible pipe. Figure 45 also highlights the whitening encountered in the regions of the gaps of the carcass for the Flexwear. For the Flexbarrier the whitened region was not restricted to the nose regions, but over the thickness of the sample.



Figure 51 – Correct disposition of each layer in a flexible pipe. Above: Flexwear – 2w and below: Flexbarrier – 2b.

The same applies to the bottom patterns of the 2w and 2b layers. Moving upward from the edge of the layers towards the nose, the pattern changes fundamentally in the whitened region; this is commonly identified as void scattering ⁽¹⁴⁵⁻¹⁴⁸⁾.

Figure 52 and Figure 53 show the positioning of the 2b and 2w sample during the scanning by SAXS, respectively.

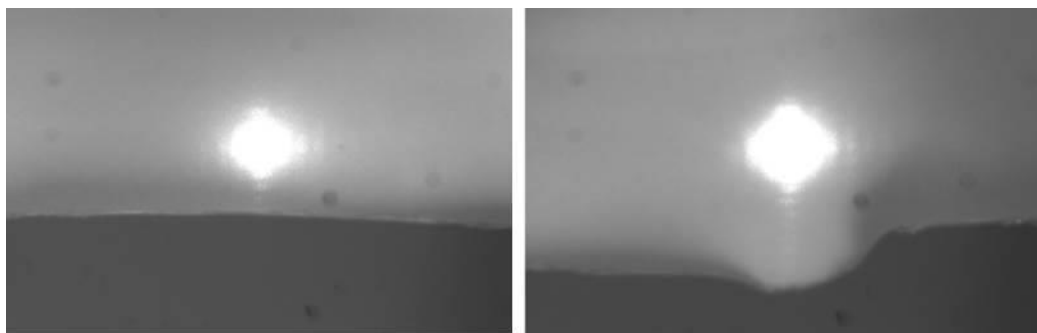


Figure 52 - Positioning of the 2b sample during the scanning by SAXS. Left: horizontal scanning; right: vertical scanning.

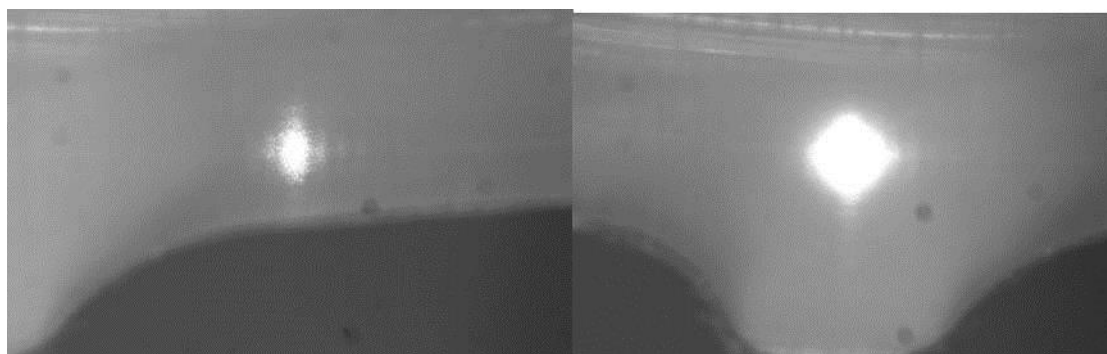


Figure 53 - Positioning of the 2w sample during the scanning by SAXS. Left: horizontal scanning; right: vertical scanning.

The difference compared to the samples taken from the damaged zone (2w and 2b) is that the bottom patterns also exhibit some orientation. Thus, in the damage zone the cold flow took place in the entire polymer layer and created orientation.

Variations of both intensity and orientation are observed along the scan paths. Where the orientation is low, we observe low intensity simply because it is more evenly distributed over the solid angle. The principal axis of the orientation is constant in the vertical scans because of the chosen path (along the central axis through the nose), see Figure 54.

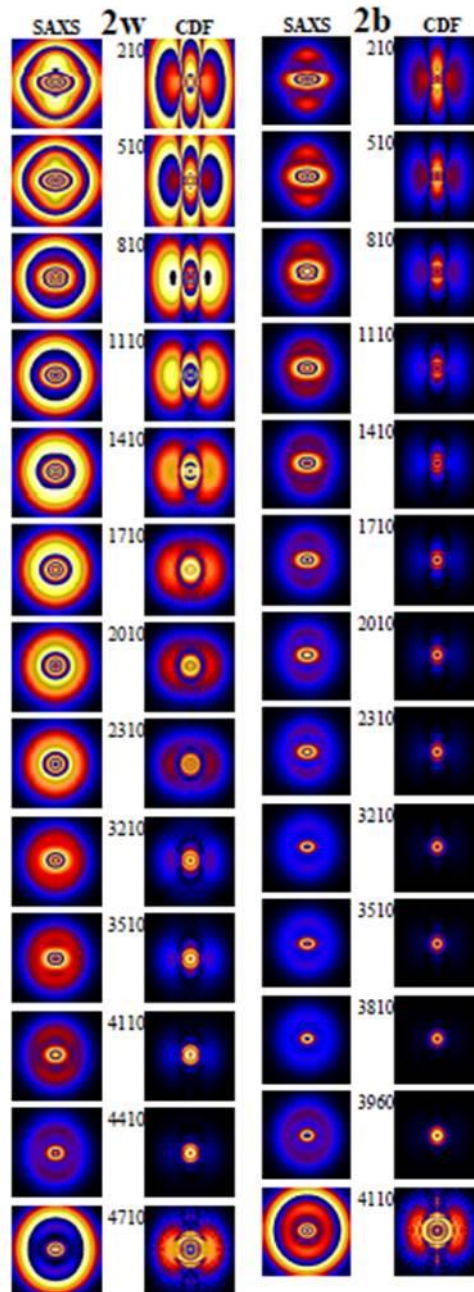


Figure 54 - 2w and 2b vertical SAXS scans of the tested pipe. Numbers indicate the depth in μm below the embossment tip. The bottom patterns are from the opposite edges of the layers. The axes of the fiber patterns are turned vertical by convention. With respect to the scan direction they have been perpendicular. Each double-column shows the SAXS intensity $I(s_{12}, s_3)$, $-0.15 \text{ nm}^{-1} \leq s_{12}, s_3 \leq 0.15 \text{ nm}^{-1}$ on identical logarithmic scale and the CDF $z(r_{12}, r_3)$ in the range $-75 \mu\text{m} \leq r_{12}, r_3 \leq 75 \mu\text{m}$.

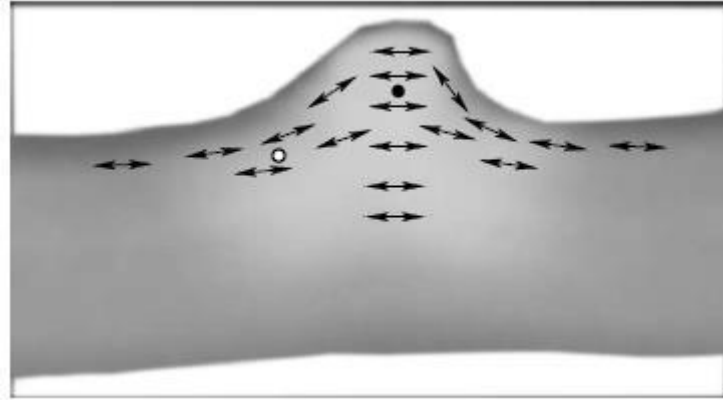


Figure 55 - PVDF after the decompression test. Variation of the uniaxial orientation direction in the vicinity of one of the embossments.

Figure 56 shows SEM-micrographs of Flexbarrier specimen 1b, undamaged region. By means of SEM the observations were acquired at 2 and 10 μ m. It is also important to note that the micrographs were taken in different positions of the sample, basically inside and outside of the whitened regions, along the PVDF layer.

As a result of the exposure and rapid gas decompression, PVDF has swollen into the gaps of the Flexlok, as already highlighted in the previous sections. The micrograph also reveals details of the whitening of the PVDF in this region.

Positions 1, 2 and 3, in the whitened region, exhibit voids in the material with a size of less than 0.5 μ m, in general. In some cases, several fibrils are visible, suggesting that some of the voids have grown and interconnected. In several places, PE particles with an elliptical shape are visible. These particles are partially debonded from the PVDF matrix. The exposure to supercritical media might be related to the debonding of the PE from the PVDF matrix, as well as for the elliptical shape following exposure.

Out of the whitened region, see position 4, at a distance of approximately 3 mm from the gap in the Flexlok wires, the material exhibits no voids. In several places PE particles with an elliptical shape are visible. These particles are all bonded to the PVDF matrix.

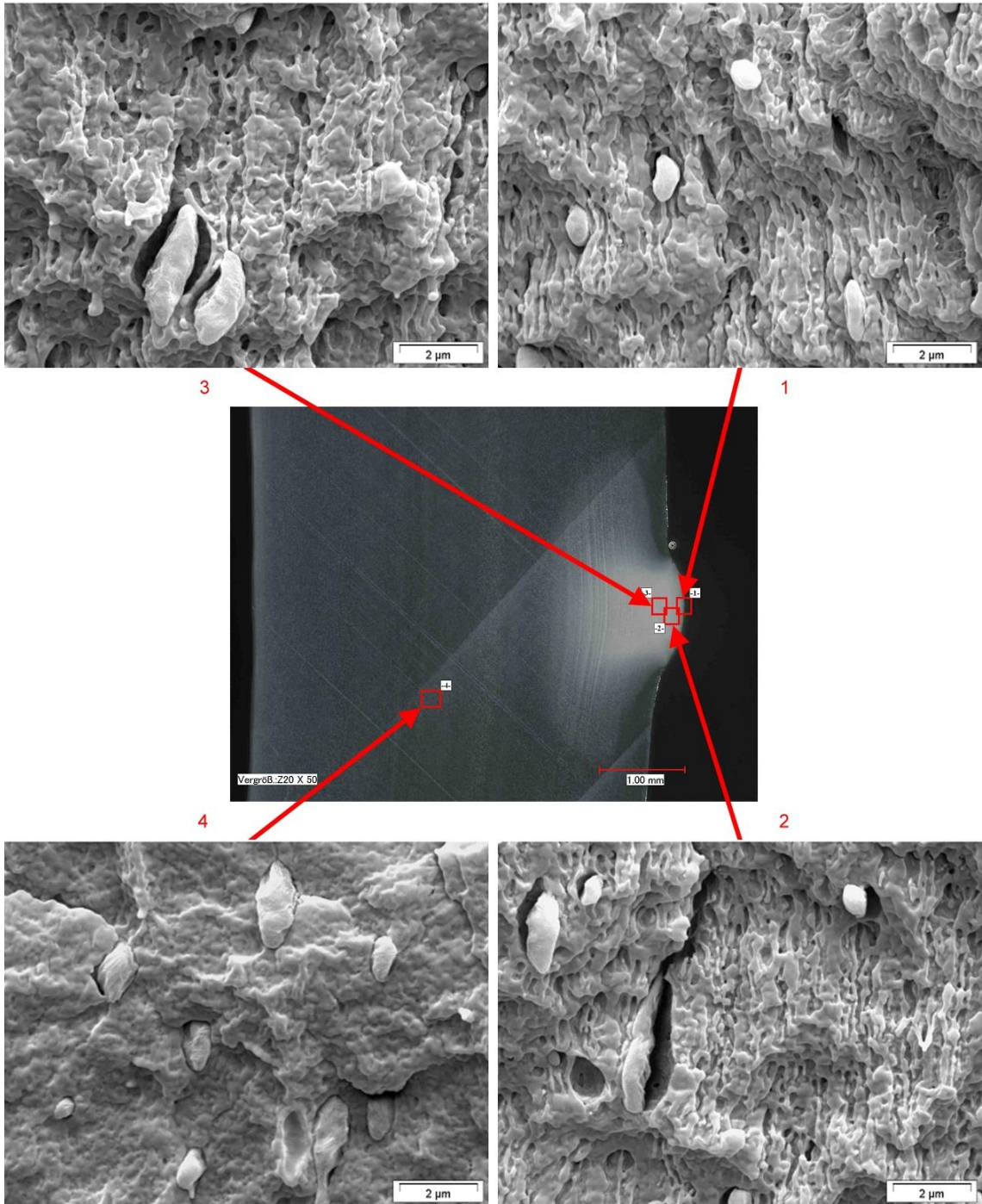


Figure 56 - SEM-micrographs of the Flexbarrier specimen 1b
 In the middle an optical transmission micrograph of the investigated area is shown with red marks at the locations where the different SEM-micrographs were taken. (location 1, where the Flexlok was undamaged) ⁽¹⁶²⁾

Figure 57 shows micrographs of Flexwear, specimen 1w, where the Flexlok layer was undamaged. As also highlighted above, PVDF expanded into the gaps of the carcass. This expansion was the result of the exposure of the polymer to the supercritical media, followed by the rapid gas decompression. The micrograph also shows whitening of the PVDF in the vicinity of this expansion into the gap.

In position 2 the material seems to exhibit very small voids with a size of less than 0.5 μm . In some cases, several fibrils are visible, suggesting that some of the voids have grown and interconnected. In several places PE particles with an elliptical shape are visible. These particles are partially debonded from the PVDF matrix. The exposure to supercritical media might be related to the debonding of the PE of PVDF matrix, as well as for its elliptical shape following exposure.

Larger voids are also visible with a size of about 1 and 2.3 μm , which are most probably imprints from PE particles. At the bottom right of the SEM-micrograph a crack with a length of more than 5 μm is visible.

In position 6, outside the whitened regions, the material exhibits no voids. In several places, PE particles with a flattened shape are visible. These particles are all bonded to the PVDF matrix.

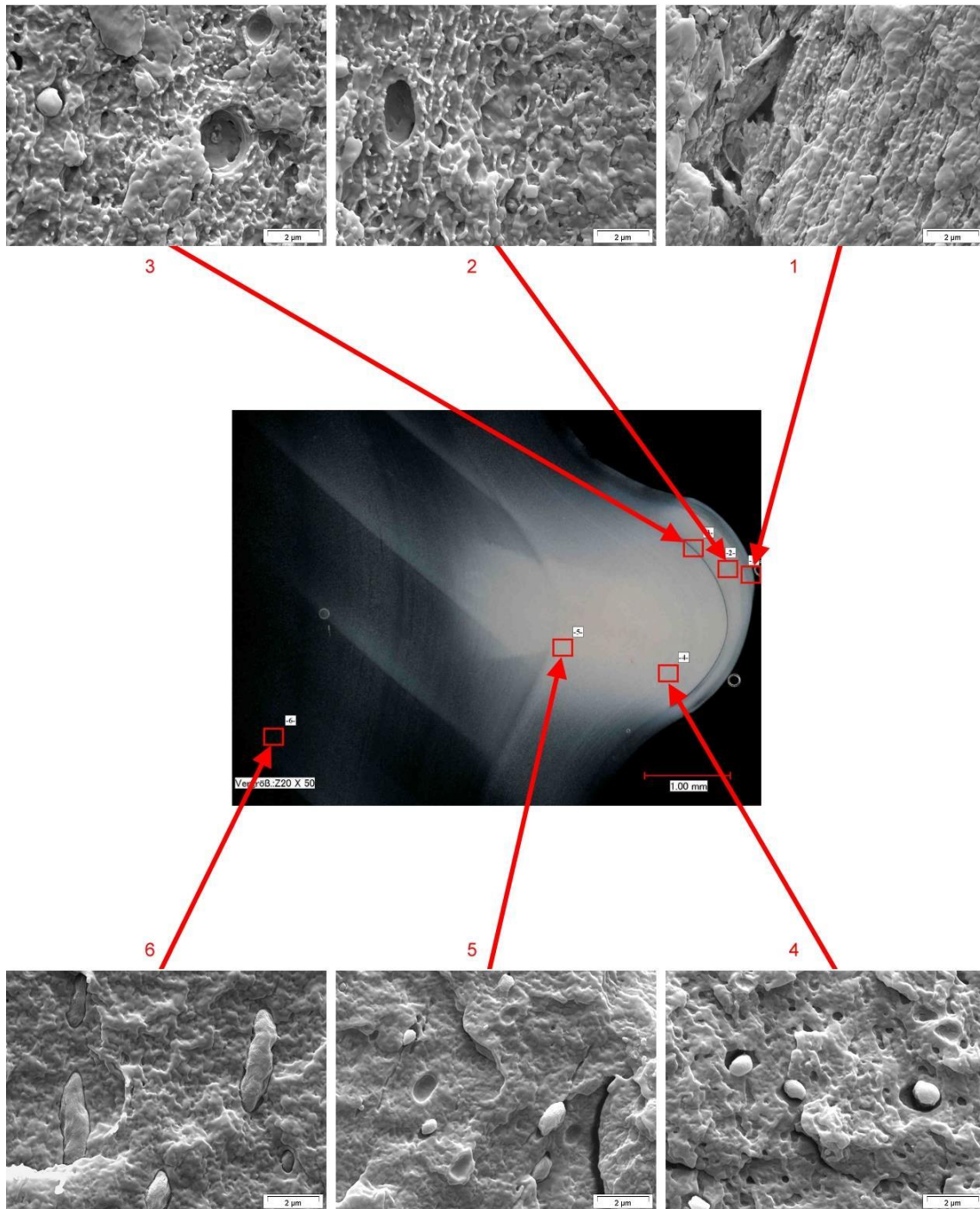


Figure 57 - SEM-micrographs of the Flexwear specimen 1w. In the middle an optical transmission micrograph of the investigated area is shown with red marks at the locations where the different SEM-micrographs were taken. (location 1, where the Flexlok was undamaged) ⁽¹⁶²⁾

4.3.2. Horizontal Scans

In the horizontal scans the principal axis of orientation changes continuously and follows contours that connect locations with an identical degree of whitening, see Figure 55. In Figure 58 the variation of the orientation axis has been compensated. It is vertical in all the displayed patterns.

As outlined in Figures 48, 49, 52 and 53, the horizontal scans have been carried out as close as possible to the outer surface of the layer.

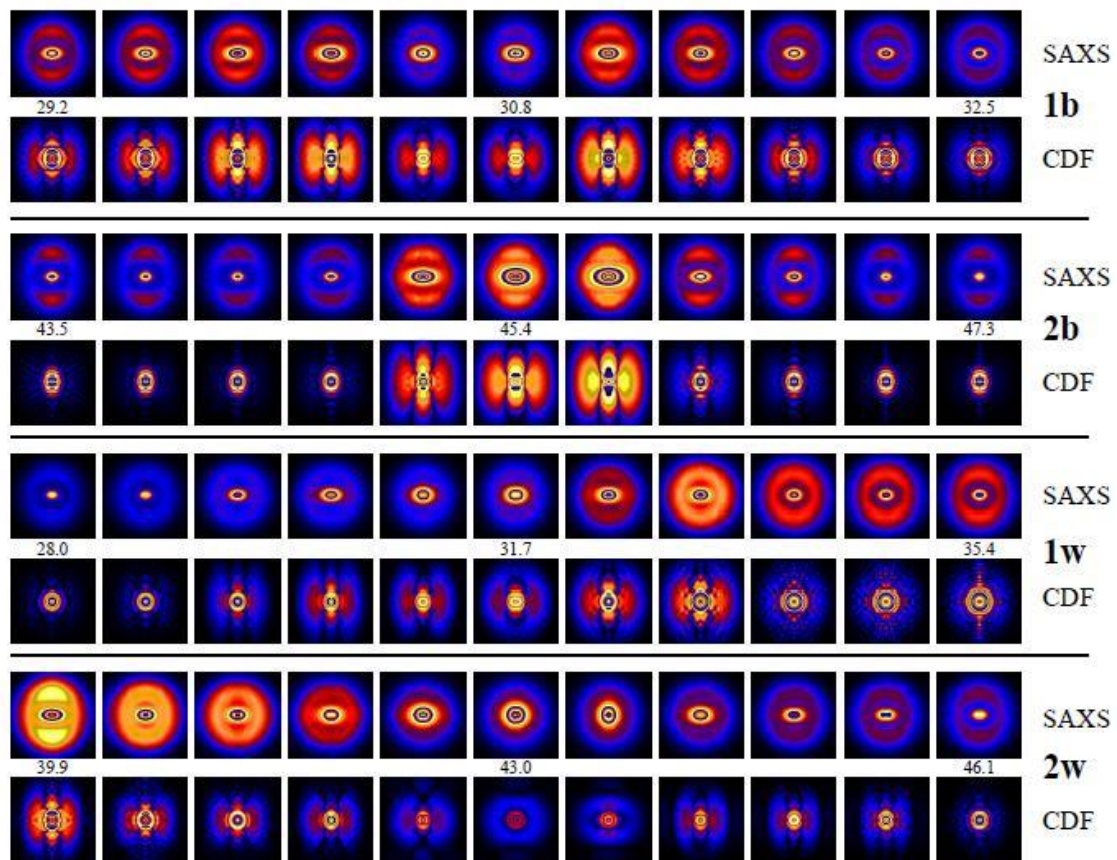


Figure 58 - Horizontal SAXS scans of tested pipe. Numbers indicate beginning, mid-point and end of the whitened zone. The axes of the fiber patterns are turned vertical by convention. Originally they have been parallel to the horizontal scan direction. Each double-row shows the SAXS intensity $I(s_{12}, s_3)$, $-0.15\text{nm}^{-1} \leq s_{12}, s_3 \leq 0.15\text{nm}^{-1}$ on identical logarithmic scale and the CDF $z(r_{12}, r_3)$ in the range $-75\text{nm} \leq r_{12}, r_3 \leq 75\text{nm}$.

Start and end points of the whitened zone are readily determined from the onset of a variation of the orientation direction as a function of the microbeam position. Because the widths of the whitened regions are different in each scanned nose, the presentation in Figure 58 has been adapted row-by-row to display this interval in which orientation axis rotation is observed.

Simultaneously this interval covers the whitened zone. Nevertheless, the formation of anisotropy starts right outside the whitened zones. In this way the data from the horizontal scans indicate that successive mechanisms of the flow are mapped into space. First, axial strain causes breaking and uniaxial orientation of the crystallites (turning lamellae stacks into microfibrils). This mechanism reaches out beyond the whitened nose regions. Second comes both whitening (void formation) and tilting of the orientation axis by the radial flow into the gap.

Comparison of the four scans show that the barrier (1b) develops a higher degree of orientation than the wear layer (1w). The milder cycling conditions in the barrier (away from the fluid) appear to cause higher perfection of orientation. The orientation appears highest in the damage region (2b and 2w). In both samples from the wear layer (1w and 2w) an intensity gradient is observed: The SAXS intensity 'on the left side' is lower than that 'on the right side' of the scanned interval. This unexplained effect may be related to geometry, e.g. a tilt of the scan path with respect to the optimum scan direction along the pipe.

The SAXS patterns in Figure 58 show two dominant features: there is a long-period peak with varying orientation distribution and a central equatorial streak of varying extension. Thus, compared to the unaffected part of the PVDF layer, the white zone is characterized by both an orientation of the crystalline domains and the presence of needle-shaped voids.

The long axis of these voids is parallel to the direction of orientation, i.e. parallel to the double-arrows in Figure 55. Therefore most of these voids should hardly increase the permeability of the PVDF barrier. The exceptions are the voids that form in the vicinity of the sharp edges of the metal coils, where they extend almost perpendicular to the polymer layer.

In Figure 58 the top scan (sample 1b) shows almost perfect symmetry about the center of the white embossment. At the edges of the white zone (outer patterns) the central scattering is weak. Towards the center it develops into a clear equatorial streak, indicating an increasing void fraction. The orientation of the

semi-crystalline stacks appears highest at some offset from the nose center. There, the peak intensity also appears higher. This higher intensity is explained by the higher concentration of intensity in narrower peaks.

For the 2b-material the scan reveals one important difference: here the orientation of the semi-crystalline stacks is highest in the center of the white zone. This finding may be related to deformation of the layer, because the failure of the Flexlok has caused an outward bending of the complete barrier and the 'straight' scan is, in fact, following a curved path with respect to an undamaged layer.

Let us discuss the two bottom scans in Figure 58. In the 1w-material (undamaged zone) the orientation of the semi-crystalline stacks is only moderate. It is much higher in the 1w material from the damaged zone (bottom scan). As with the 1b-material, the 1w-material exhibits an increased amount of voids slightly offset from the center of the white embossment. In the 2w-material the center of the white embossment shows a relatively low amount of voids and a low orientation, whereas the material from the outer part of the whitened embossment exhibits both voids and highly orientated semi-crystalline stacks. An explanation has already been given at the end of the previous paragraph: the scan has been performed straight through the damage-induced bulge of the wear layer.

Figure 59 shows SEM-micrographs of Flexbarrier specimen 2b, where the Flexlok was broken.

In positions 1, 2, 5, 6 and 7, whitened region, the material exhibits voids with a size of less than 0.5 μm . In several places PE particles with a flattened shape are visible. One of these particles is partially debonded from the PVDF matrix; the others are bonded. Two larger elliptical voids are visible with a length of about 2 to 3 μm , which is most probably an imprint from a PE particle. Some of the voids seem to be connected.

In positions 3 and 4 the material exhibits no voids. PE particles with a flattened shape are visible which are oriented in the diagonal direction of the SEM-micrograph. The length of these particles is approximately 1 to 3 μm , the thickness approximately 0.5 μm . These particles are partially debonded from the PVDF matrix. The overall appearance reveals a layered pattern in the diagonal direction.

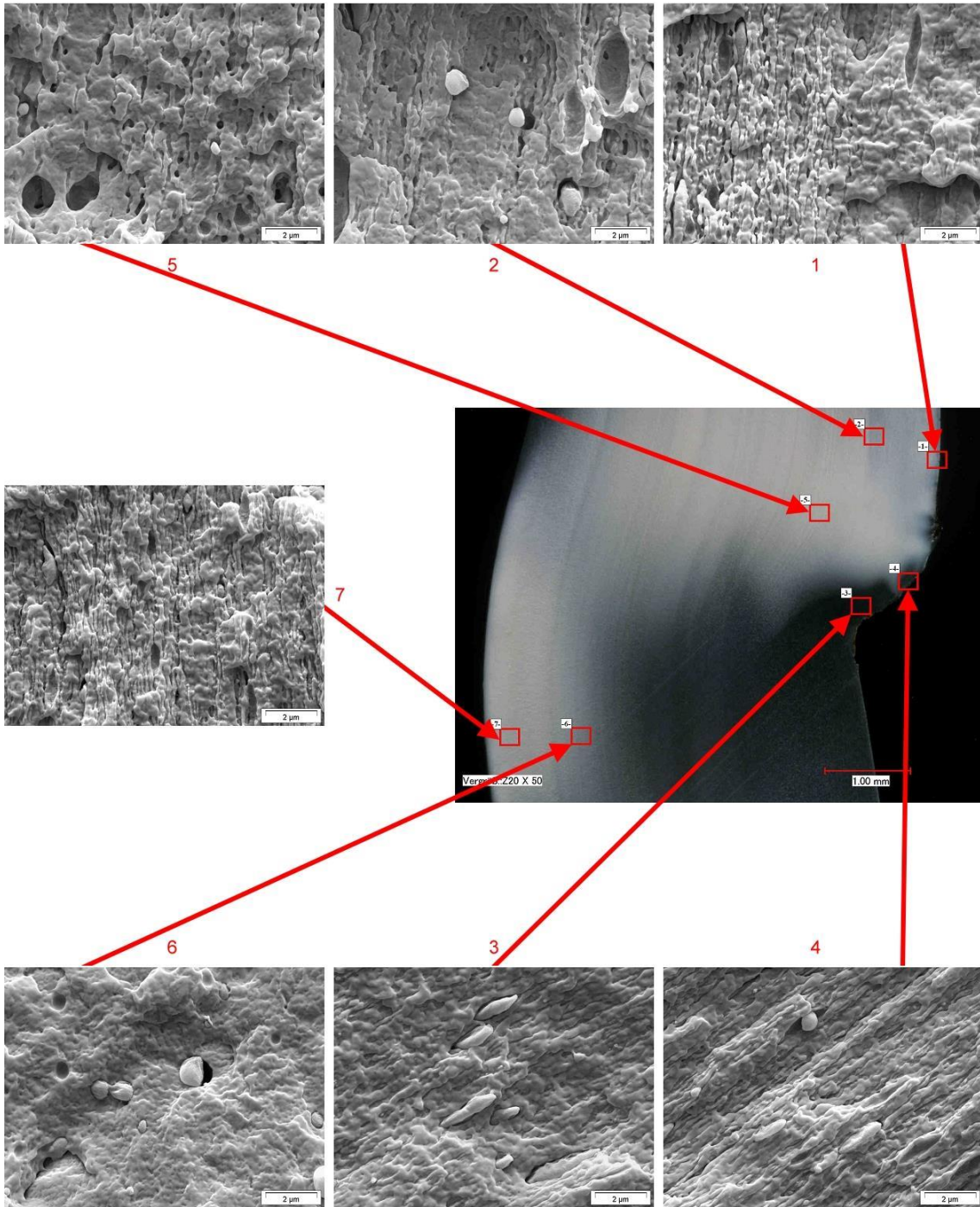


Figure 59 - SEM-micrographs of the Flexbarrier specimen 2b. In the middle an optical transmission micrograph of the investigated area is shown with red marks at the locations where the different SEM-micrographs were taken (location 2, where the Flexlok was broken) ⁽¹⁶²⁾

Figure 60 shows SEM-micrographs of Flexwear specimen 2w, where the Flexlok was broken. As a result of the exposure and rapid gas decompression, PVDF expanded into the gaps of the carcass, as highlighted in the previous sections. The micrograph also shows whitening of the PVDF in the vicinity of this expansion into the gap.

In positions 1, 2 and 3 the material exhibits voids with a size of less than $0.5\ \mu\text{m}$ for which it is difficult to see whether they are connected. Flattened PE particles are visible. One particle is partially debonded from the PVDF matrix.

In position 4, at a distance of approximately 3.8 mm from the surface of the carcass, out of the whitened region, the material exhibits no voids in the bulk of the PVDF matrix. However, two larger voids are visible with a size of about 1.5 to $3\ \mu\text{m}$, which are most probably imprints from PE particles.

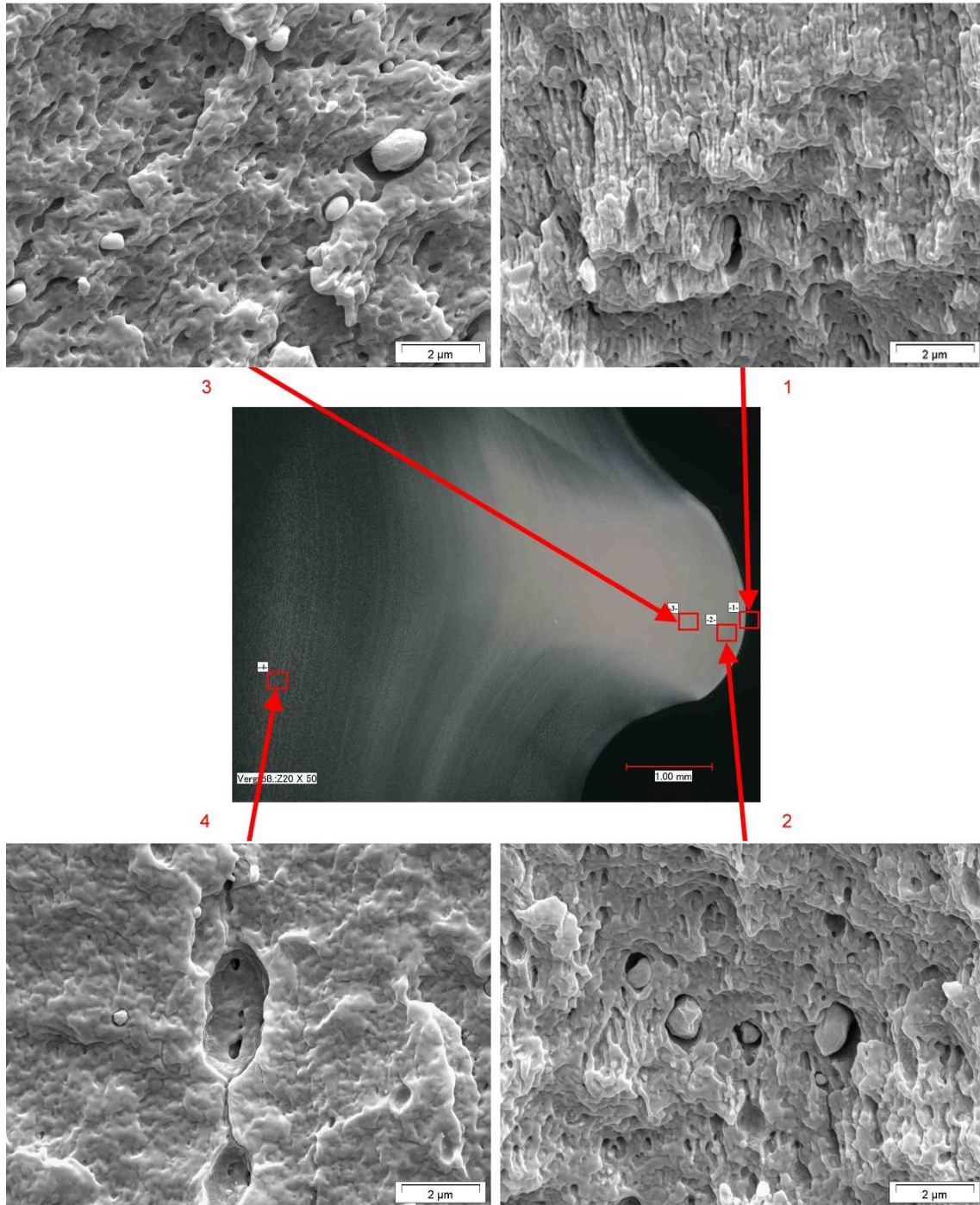


Figure 60 - SEM-micrographs of the Flexwear specimen 2w. In the middle an optical transmission micrograph of the investigated area is shown with red marks at the locations where the different SEM-micrographs were taken (location 2, where the Flexlok was broken) ⁽¹⁶²⁾

4.3.3. Quantitative Analysis

Morphology away from the cold-flow zones. Even for the samples from the tested pipe, there are regions in which the SAXS shows no voids and is isotropic. This is the case for the 1w and 1b samples along a line in the middle between the noses, where the polymer was supported by the metallic layers.

Here the lamellar semi-crystalline structure of PVDF has not been transformed fundamentally. Patterns from opposite sides of the double PVDF layer were analyzed. For this purpose, isotropic scattering curves are extracted. It is assumed that a lamellar two-phase system is present. Ruland's IDF is computed and fitted with a stacking model ⁽¹⁵³⁾.

Figure 61 shows one of the IDFs together with the corresponding fit. Table 7 shows descriptive morphological parameters, which result from fits to the IDF. The estimated intervals of confidence for the parameter values are smaller than the last given digit. The virgin material and the tested material from the wear layer show a volume crystallinity $v_c = 0.5$. This is common with PVDF. In the wear layer the average long period has increased and the distribution of long periods has narrowed; both changes are typical annealing effects.

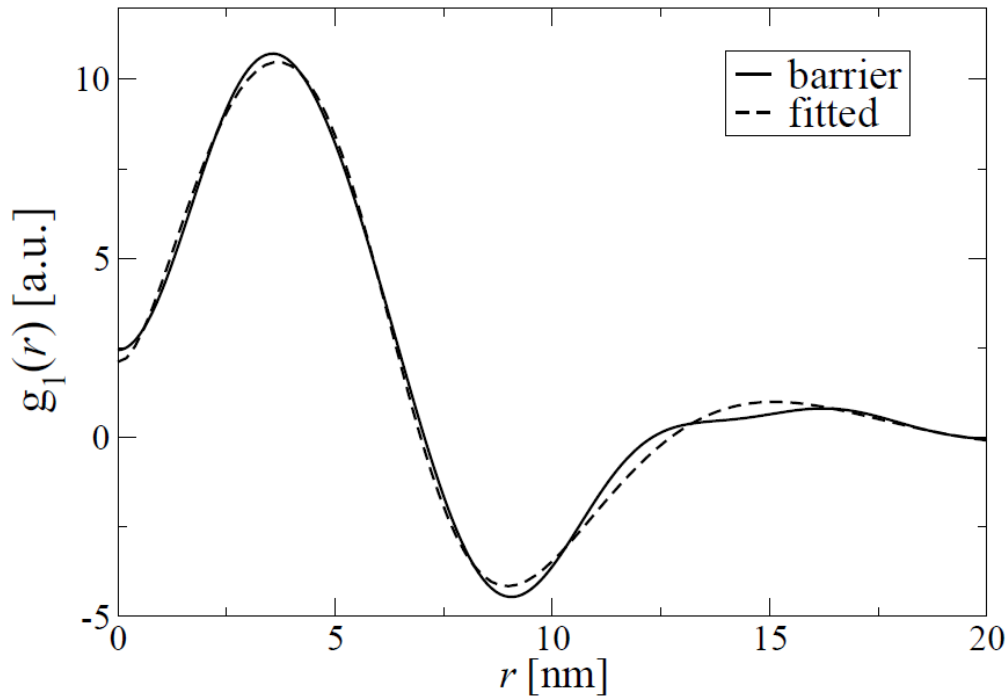


Figure 61 - The interface distribution function $g_1(r)$ as computed from isotropic scattering in the tested barrier layer and its fit by simple stacking statistics of crystalline and amorphous layers. Deviations indicate a weak second component.

Table 7 – Pure semi-crystalline isotropic morphology far from cold-flow zones as determined by IDF analysis. d_c is the number-average thickness of the crystalline layer and v_c is the volume crystallinity in the lamellae stacks. Additionally, the numerical-average long period L_{IDF} , and the relative variance σ_L/L_{IDF} of the distribution are shown.

sample	d_c [nm]	v_c	L_{IDF} [nm]	σ_L/L_{IDF}
virgin	4.5	0.50	8.9	0.38
wear	5.0	0.50	9.9	0.31
barrier	5.4	0.58	9.2	0.33

In the barrier layer the thickness d_c of the crystalline layer is highest. In major part, it has grown at the expense of the amorphous layers, i.e. the crystallinity in the layer stacks has increased. Crystallinity increase is typical for the annealing of semi-crystalline polymers under mild conditions, and during the test the conditions at the surface of the barrier layer (away from the fluid) are presumably milder than those at the surface of the wear layer. The transfer of the IDF evaluation method to the whole series is impossible, because anisotropy and void content vary continuously.

Degree of orientation in vertical scans as a function of depth. It has not been possible to quantify the degree of orientation in vertical scans. The interference of the semi-crystalline stack orientation with the variation of void scattering is too strong.

Long periods. Only by an automated method can the large amount of scattering data be analyzed in reasonable time. A suitable method is the tracking of peak positions and peak shapes. The broad peak in the SAXS does not show a clear maximum for complete series (cf. Figure 44) and most peaks of the CDF are rather unclear, because the arrangement of the crystalline domains is poor. Only the long-period peak of the CDF is clearly separated in all data sets. Thus, it is selected for analysis. The location of the peak maximum on the meridian is a measure of the most frequent distance \bar{L} between adjacent crystalline domains. From the peak shape in the meridional direction (s_3) we calculate the relative variation interval $\sigma_{\bar{L}}/\bar{L}$ of the long periods (¹⁵⁴).

Figure 62 shows the variations of the most probable long period $\bar{L}_{(y)}$ as a function of the depth y below the respective nose tip. In order to assess the significance of the presented curves, we have also directly tracked the broad long-period peak in $I(s)$ where it has been clear enough. We find a coincidence for $y > 2$ mm.

There are similarities for higher y in the curves of material from the damaged and undamaged regions. For example, the top two curves are from the barrier. The 1b shows a constant long period of $13.5 \mu\text{m}$ down to $y \approx 1.5$ mm.

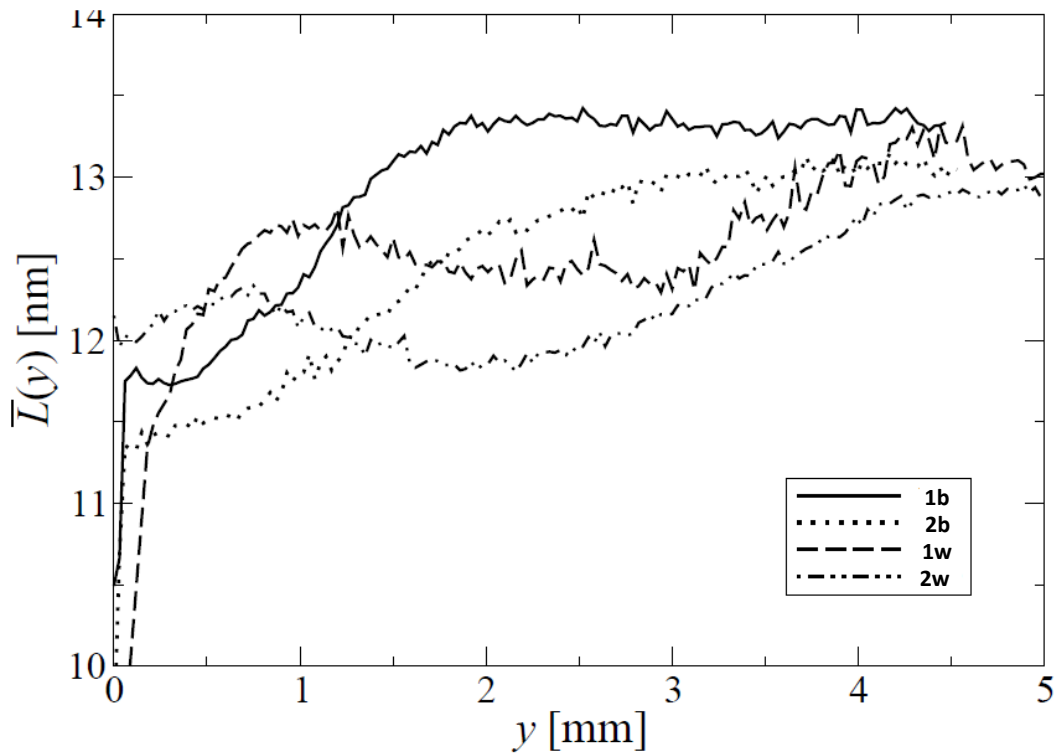


Figure 62 - Most probable long period $\bar{L}(y)$ in vertical scans through the embossments of tested material. y is the depth below the embossment tip

For lower depths the long period decreases smoothly to 12 μm . The 2b sample, from the damage zone behaves similar to sample 1b. In 2b the long-period decrease is observed for $y < 2.5$ mm. The fact that it reaches further down than 1b is probably due to the increased cold flow of the PVDF under the fracture zone. The samples from the wear layer (1w and 2w) do not show the plateau of the 1b and 2b for large values of y . A wavy course of $\bar{L}(y)$ appears to be typical for both samples. Again, the material from the damaged zone exhibits lower long periods, in general.

The curves of the horizontal scans are not shown. For all materials they only demonstrate, that inside the whitened zones \bar{L} decreases slightly from 13 μm to 12 μm , while $\sigma_{\bar{L}}/\bar{L}$ increases from 0.15 to 0.25. Thus, close to the filled gap the main effect of the cold flow is a broadening of the long period distribution.

Voids. SAXS can only detect voids up to a certain limit. The size depends on the optical adjustment of the instrument. It is 160 μm for the experiments presented here. We assume that there are also longer because the nose regions appear white. Such voids cannot be detected by SAXS, but by light scattering.

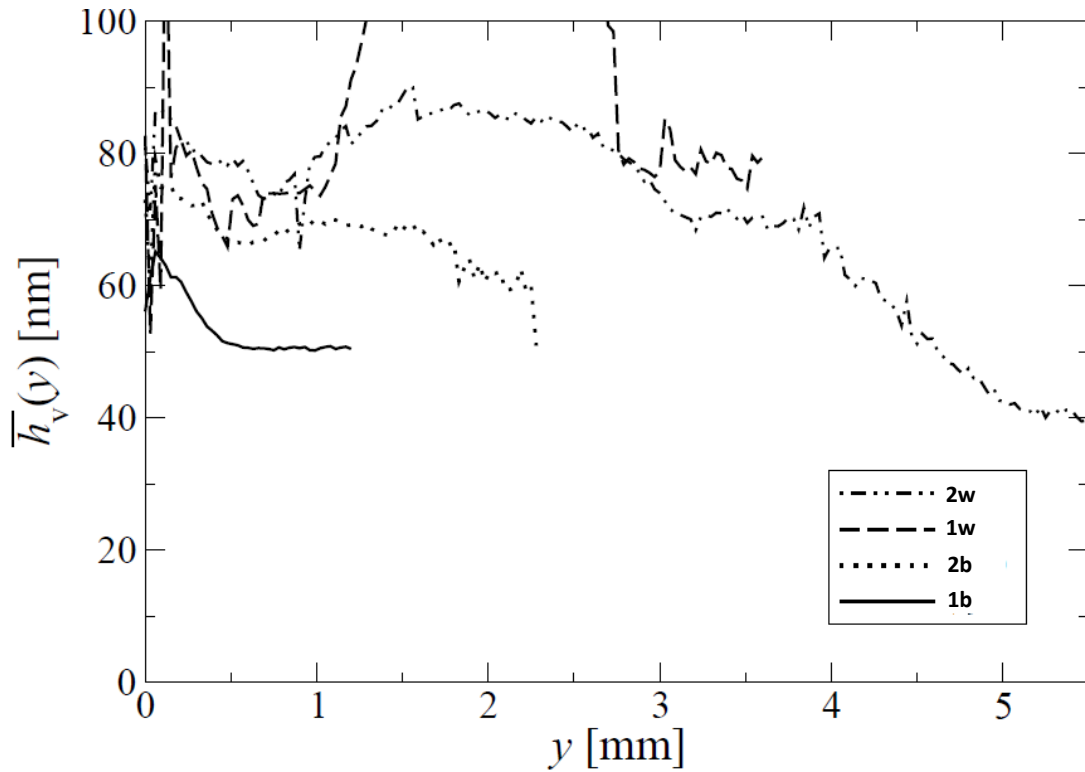


Figure 63 – Average void height $\bar{h}_v(y)$ in vertical scans through the embossments of tested material. y is the depth below the embossment tip.

The relatively diffuse equatorial streak in the scattering pattern can hardly be analyzed automatically. Therefore, we examine the corresponding feature in the CDF. It is represented by two weak, long peaks running parallel to the meridian (in the vertical direction). Its extension in the meridional direction is a measure of the straight height $\bar{h}_v(y)$ of the voids that are detected by the setup, its distance from the meridian characterizes their average diameter \bar{d}_v .

For the vertical scans Figure 63 shows the variation of void heights \bar{h}_v . The curves end at different depths y . Below this level no more voids can be analyzed quantitatively. In 2w voids range farthest down into the layer. This is explained by the harsher test conditions in the wear layer as compared to the

barrier. In sample 1b voids can only be detected up to 1 mm below the embossment tip. In sample 1w the equatorial streak is rather noisy. This fact decreases the accuracy by which the void height can be determined. Nevertheless, in the areas where we trust the values, the heights for sample 1w and 2w match. The void heights are longest 2 mm below the embossment tip. The heights of detectable voids in the barrier are lower than those found in the wear layer (explanation: harsher test conditions). In summary, the barrier is less penetrated by voids than the wear layer. Moreover, the needle-shaped voids detected in the barrier are shorter.

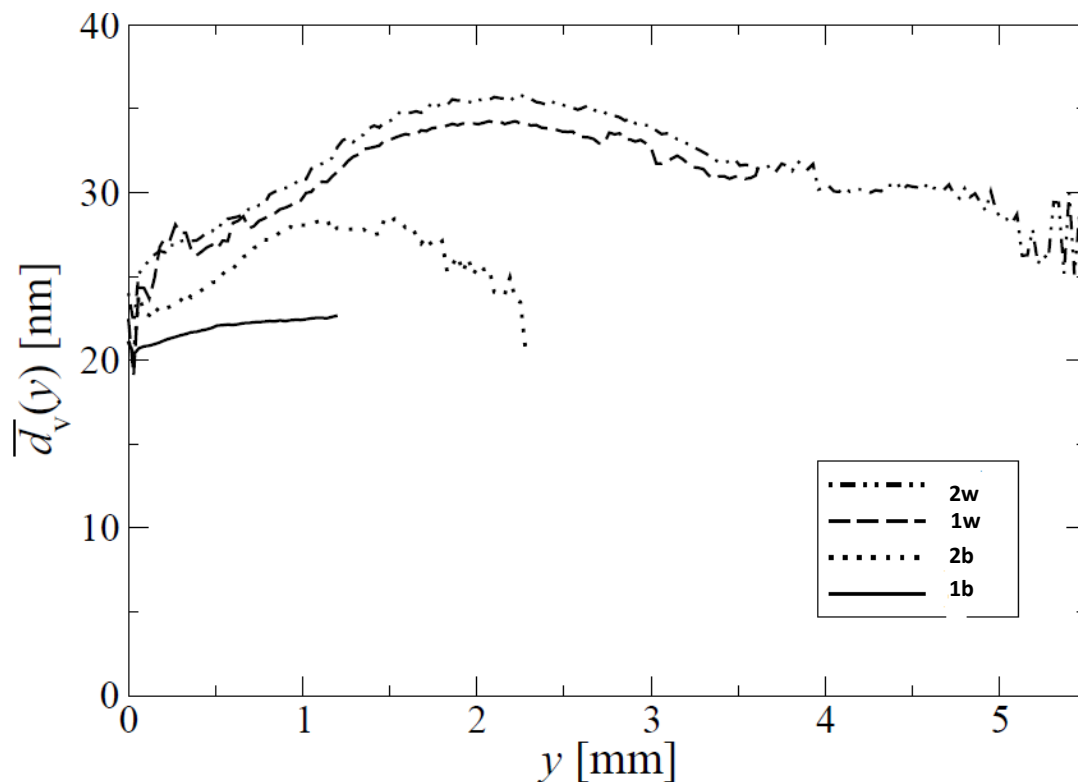


Figure 64 - Void diameter $\bar{d}_v(y)$ in vertical scans through the embossments of tested material. y is the depth below the embossment-tip.

Thus, the wear layer performs its task: it protects the barrier layer. Figure 64 shows the average void diameter $\bar{d}_v(y)$ in the vertical scans. Again, the data of the wear layer appear to be less influenced by the proximity to the damage area, probably because the voids are already fully developed in 1w because of the harsh cycling conditions. All the determined diameters d_v are much lower than the resolution limit of our setup ($160 \mu\text{m}$). This means that we can only expect voids with a very large diameter, if the void diameter distribution is not unimodal.

Horizontal scans give an impression of the lateral extension of the void-rich nose regions. Visual inspection of the samples themselves (Figure 29) shows that the lateral widths of the whitened zones vary considerably from nose to nose. Therefore, it makes no sense to draw detailed conclusions from the shapes of the corresponding curves.

The data indicates that the structure rearrangement propagates from the corrugated metal into the bulk. Close to the nose there is a highly oriented, high-crystalline PVDF. At depths below the end of the white zones the crystallinity is very low, almost no SAXS, and deeper in the 'virgin' material we have the isotropic long-period ring of the virgin PVDF. So the vertical scans are most important, but there is additional information in the horizontal scans – related to a nanoporosity that is observed in the rearranged layer.

4.3.4. Density Results

The density of the specimens from both the Flexbarrier and the Flexwear at both the undamaged damaged regions have been determined and compared. The results are shown in Table 8.

Specimens from the undamaged region exhibited almost the same density as the virgin material. Specimens from the damaged region exhibited a lower density than the virgin material, due to the presence of the voids in about 1% of the PVDF microstructure. The errors of the measurements shall be not disregarded.

For the density, the dimensions of each sample, the inner diameter, thickness of layer, outer diameter, and weight were measured after the test. Before the test the values of reference were acquired from the design of the pipe.

Figure 65 shows the specimens from the undamaged region, Flexwear and Flexlok and Figure 66 shows the specimens from the damaged region, Flexwear and Flexlok.

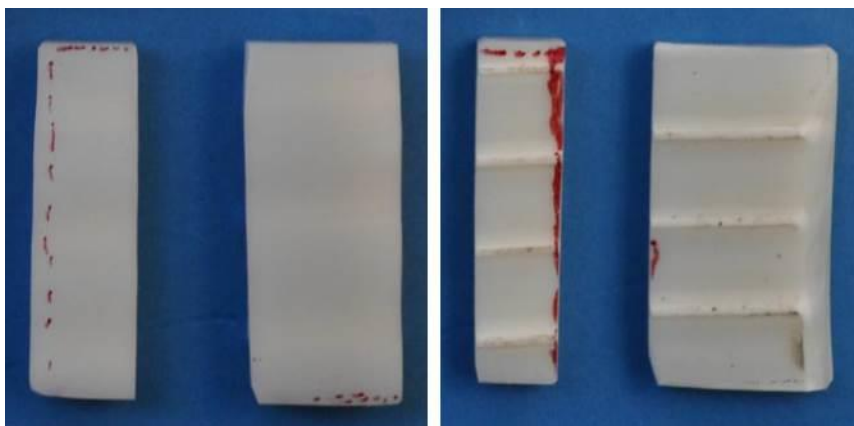


Figure 65 - Photos of the specimens from undamaged region. left: 1w-2 and 1w-1 (Flexwear) and right: 1b-2 and 1b-1 (Flexbarrier) ⁽¹⁶²⁾.

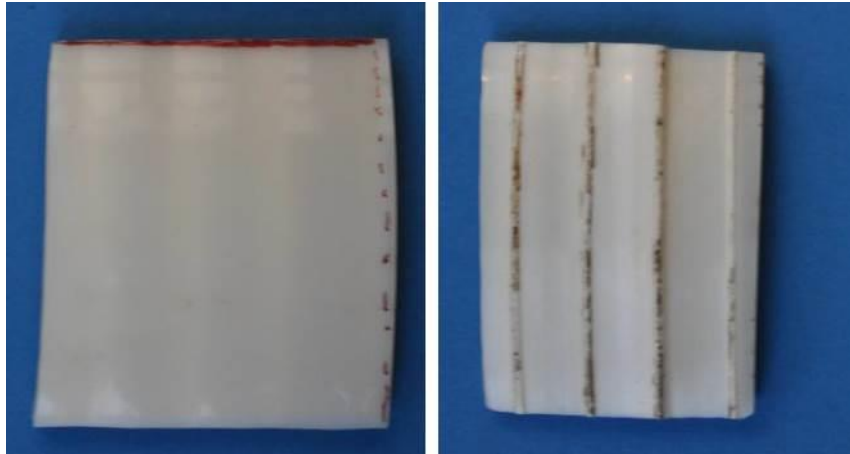


Figure 66 - Photos of the specimens from damaged region. left: 2w (Flexwear) and right: 2b (Flexbarrier) ⁽¹⁶²⁾

Table 8 – Density of specimens

Layer	location	specimen	ρ [g/cm ³]
4" pipe	na	virgin	1.775
Flexbarrier	1	1b-1	1.778
		1b-2	1.774
		average	1.776
	2	2b-1	1.763
Flexwear	1	1w-1	1.771
		1w-2	1.779
		average	1.775
	2	2w-1	1.758

4.3.5. WAXS Measurements

As already discussed in Section 1.2.2.2, the microstructure of PVDF in the β -phase strongly depends on the way in which the phase is obtained ^(11,12). By stretching from the α -phase at precise stretch ratios, at defined temperatures, the microstructure changes from a spherulitic to a microfibrillar structure ⁽²⁹⁾.

During the deformation at this stage, the spherulitic crystalline structures in the PVDF are turned into microfibrils aligned in the tensile direction, which favors the α - β transformation ^(155,156). Creation of defects and a heterogeneous stress distribution in the samples play critical roles in α - β transformation ⁽¹⁵⁷⁾. Moreover, both crazing and shear yielding represent plastic deformation modes with high molecular orientations which, in the case of semi-crystalline polymers, may result in a phase transformation ⁽¹⁵⁸⁾.

Wu et al.⁽¹⁵⁷⁾ carried out in-situ simultaneous synchrotron WAXS and SAXS measurements to investigate PVDF fibers during stretch-hold deformation. Their results suggested that defects induced by yielding and plastic flow played an important role in α to β crystal transformation in PVDF and they also believed that crystallites are sheared apart at high strains. In addition, in high strain the crystallites (mixed α and β form) are linked by extended amorphous chains along the fiber axis and coexisting with the relatively strongly correlated microvoids.

In order to discuss the influence of the structure on the mechanical properties, WAXS has been successfully employed by synchrotron to quantify the crystalline structure of PVDF at different stretching temperature conditions. The scattering intensity profiles along the meridional direction from 2D WAXS patterns dependent strain at both 60°C and 140°C has been published ⁽¹⁵⁹⁾. The profiles of PVDF before stretching at both temperatures show three characteristic peaks, which are assigned to the (100), (020) and (110) diffractions of isotropic α -form PVDF.

Corresponding with the reported results upon further stretching, the emergence of the new peak at $2\theta = 20.8^\circ$, which is generally corresponded to β (110) (200) diffraction, instead of 20.2° is observed ⁽¹⁵⁹⁾. It is accompanied with the disappearance of the three α peak and the decreasing content of α -form, which indicates the α to β form transformation induced by stretching as reported ^(160,157).

Figure 67 shows WAXS results for PVDF, at 60°C and 140°C at different tensile elongation rates and the typical peaks related to the α to β form ⁽¹⁵⁹⁾.

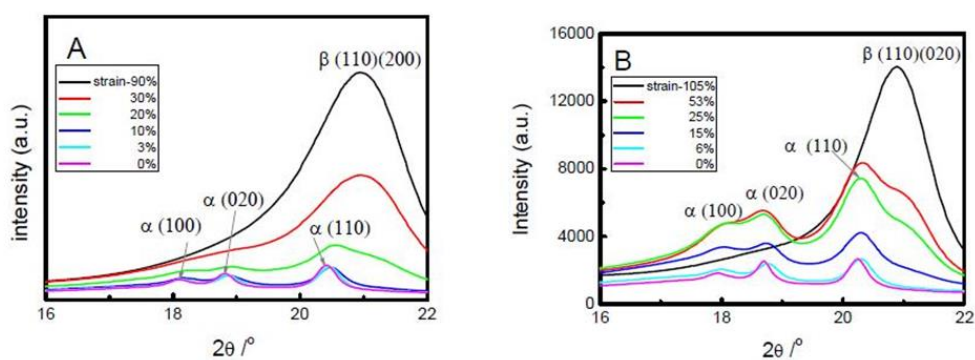


Figure 67 - WAXS profiles along the meridional direction during stretching at 60°C (A) and 140°C (B) ⁽¹⁵⁹⁾.

WAXS measurements were carried out at Hamburg University using the equipment X'Pert Pro MPD Powder Diffractometer from PHILIPS, in order to detect any α - β transformation for PVDF. For the measurements, the same samples adopted for the SAXS measurements were used. A virgin PVDF was also used as reference. Figure 68 shows the selected samples used.

WAXS was carried out as a concern about the possible change of phase of PVDF in the whitening regions of the gaps had already been raised.

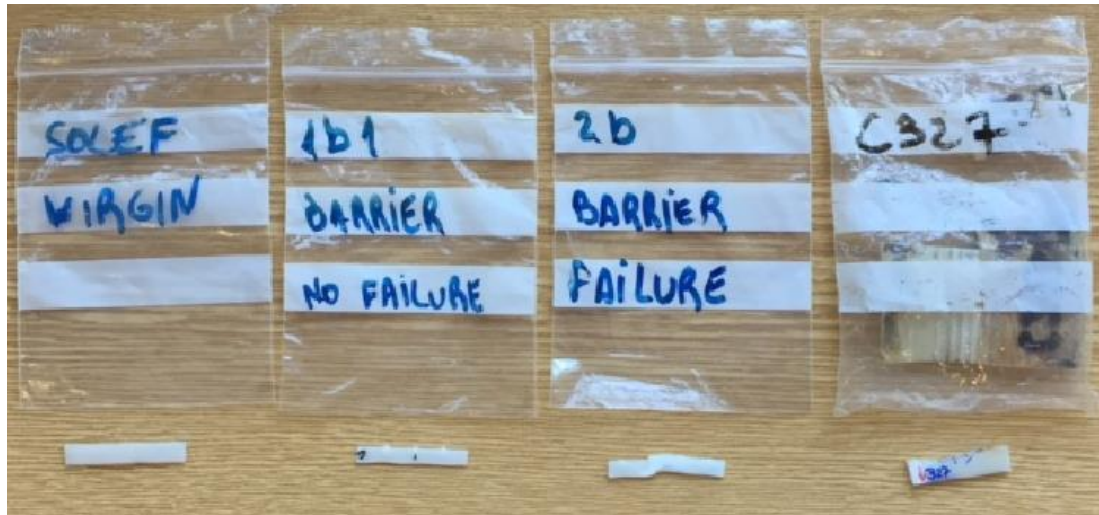


Figure 68 - Samples for WAXS from the left to the right: Virgin PVDF, 1b-1 (no failure), 2b (failure region/with whitening) and 327.

Figure 69 shows the curves acquired for Virgin PVDF, 1b-1 (no failure region), 2b (failure region/with whitening) and 327. In general all curves presented the same profile, with no notary difference among them. The 3 peaks encountered are probably assigned to the (100), (020) and (110) diffractions of isotropic α -form PVDF. No peak was found in the region 20.8° , which is generally corresponded to β (110) (200) diffraction.

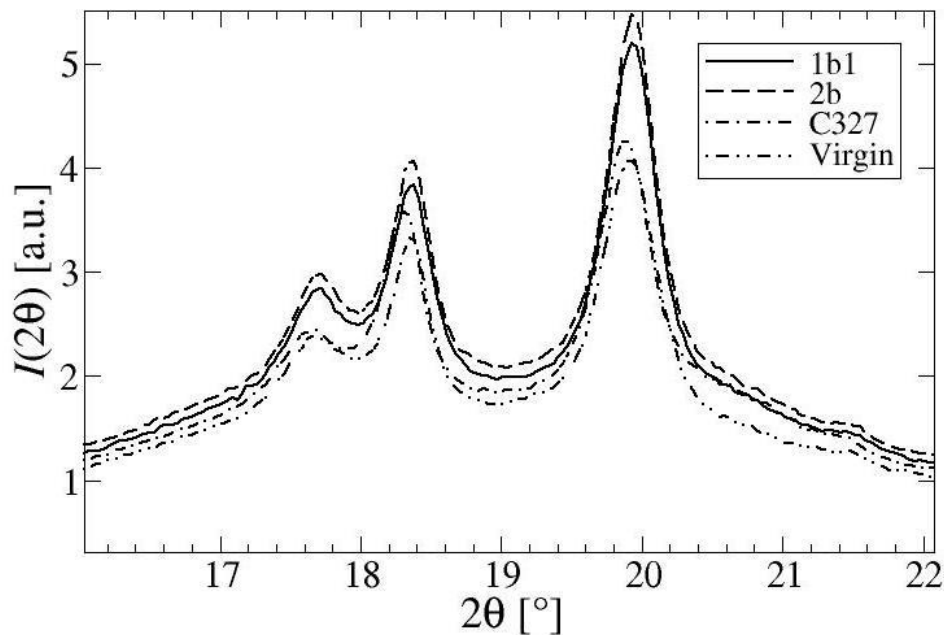


Figure 69 - WAXS profiles for the virgin PVDF, 1b1, 2b and 327 samples. No peak was found in the region 20.8° , which is generally corresponded to β (110) (200) diffraction.

4.4. SAXS – Additional Samples

Figure 70 shows the selected patterns from vertical micro-beam scans through the Flexbarrier of 327 sample. The patterns shown on the left of Figure 70 were taken close to the upper side of the sample. The patterns on the right are from the opposite edge of the scanned layer. See also a picture of the sample showing the positioning of the scan along the sample.

All the patterns are normalized to identical flux and identical irradiated volume. They are on the same logarithmic intensity scale. The scans were taken on the vertical position only for a qualitative investigation. The aim was to observe any structural rearrangement of PVDF after some steps required during the manufacturing of the flexible pipes. In the vertical scans, the measurements were acquired along 5 mm of the length of the sample.

SAXS patterns showed an isotropic along the whole sample, which can be related to some overstrain experienced for Flexbarrier in the sealing region of the pipe, when the sealing connects squeeze the Flexbarrier; details of the sample are presented in Figure 62. Moving downward from the top edge of the sample, the pattern stays fundamentally anisotropic with oriented structure.

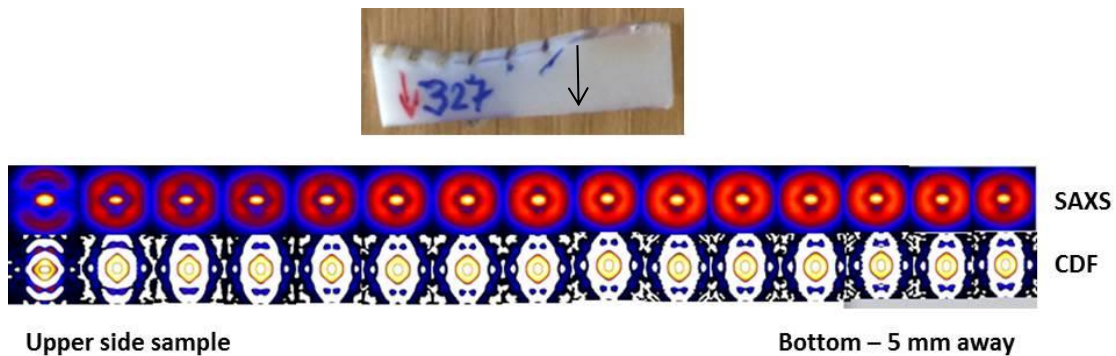


Figure 70- 327 vertical SAXS scans. The initial patterns represent the upper edge of the samples. The bottom patterns are from the opposite edges of the layer. Each double-column shows the SAXS intensity $I(s_{12}, s_3)$, $-0.15\text{nm}^{-1} \leq s_{12}, s_3 \leq 0.15\text{nm}^{-1}$ on identical logarithmic scales and the CDF $z(r_{12}, r_3)$ in the range $-75\mu\text{m} \leq r_{12}, r_3 \leq 75\mu\text{m}$.

Figure 71 shows selected patterns from vertical micro-beam scans through the Flexbarrier of the 572 sample. The patterns shown on the left of Figure 71 have been taken close to the upper side of the sample. The patterns on the right are from the opposite edge of the scanned layer. Figure 71 displays the sample showing the positioning of the scan along the sample.

All the patterns are normalized to identical flux and identical irradiated volume. They are on the same logarithmic intensity scale. The scans were done on the vertical position only for a qualitative investigation. The aim was to observe any structural rearrangement of PVDF after some steps were required during the manufacturing of the flexible pipes. In the vertical scans, the measurements were acquired along 5 mm of the length of the sample.

Moving downward from the top edge of the layers, the pattern showed itself as an isotropic material along the sample. No orientation was registered by SAXS.

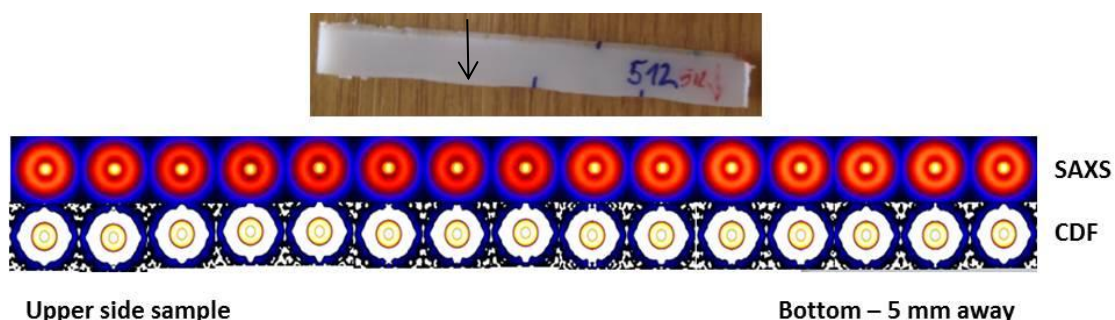


Figure 71 - 572 vertical SAXS scans. The initial patterns represent the upper edge of the samples. The bottom patterns are from the opposite edges of the layer. Each double column shows the SAXS intensity $I(s_{12}, s_3)$, $-0.15 \text{ nm}^{-1} \leq s_{12}, s_3 \leq 0.15 \text{ nm}^{-1}$ on identical logarithmic scales and the CDF $z(r_{12}, r_3)$ in the range $-75 \mu\text{m} \leq r_{12}, r_3 \leq 75 \mu\text{m}$.

Figure 72 shows selected patterns from vertical micro-beam scans through the Flexwear layer of the 572w sample. The patterns shown on the left of Figure 72 have been taken close to the upper side of the sample. The patterns on the right are from the opposite edge of the scanned layer.

All the patterns are normalized to identical flux and identical irradiated volume. They are on the same logarithmic intensity scale. The scans were done on the vertical position only for a qualitative investigation. The aim was to observe any structural rearrangement of PVDF after some steps were required during the manufacturing of the flexible pipes. In the vertical scans, the measurements were acquired along 5 mm of the length of the sample.

Moving downward from top edge of the layers, the pattern showed itself as an isotropic. No orientation was registered by SAXS.

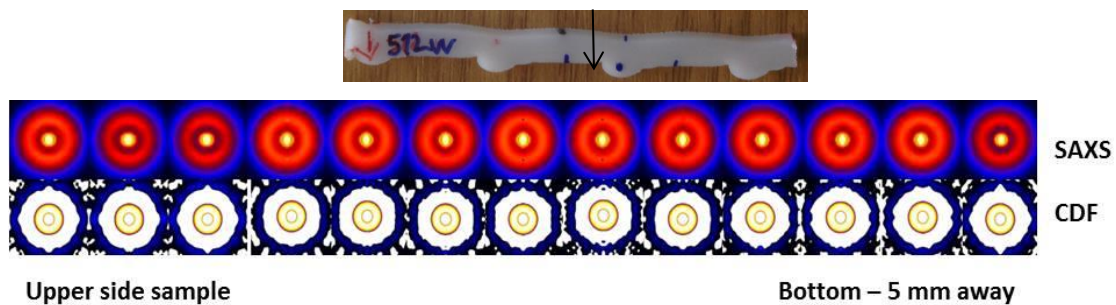


Figure 72 - 572w vertical SAXS scans. The initial patterns represent the upper edge of the sample. The bottom patterns are from the opposite edges of the layer. Each double-column shows the SAXS intensity $I(s_{12}, s_3)$, $-0.15\text{nm}^{-1} \leq s_{12}, s_3 \leq 0.15\text{nm}^{-1}$ on identical logarithmic scale and the CDF $z(r_{12}, r_3)$ in the range $-75\mu\text{m} \leq r_{12}, r_3 \leq 75\mu\text{m}$.

4.5. Mid-scale Swelling Test Result

A test at Eurotechnica was initiated on 25 April 2013. First, the water inside the tank was heated up to 90°C. The room temperature was also monitored.

After reaching the required test temperature, the bore of the pipe was pressurized with CO₂. Figure 73 shows the registered data during the test, such as: tank temperature $T_{(1)}$, room temperature $T_{(2)}$ and bore pressure (P). Each strain gauge was also monitored and the identification (EE) of each strain gauge is also shown in the chart.

When the bore of the sample reached the required pressure of 414 bar, a sudden drop in pressure was observed. There was also a dull sound. Figure 73 showed that strain gauge 12 had registered a drop of strain on the Flexlok wire close to the sealing region. After the depressurization of the sample it was agreed to proceed with the dissection of the sample in order to investigate the cause of such a failure.

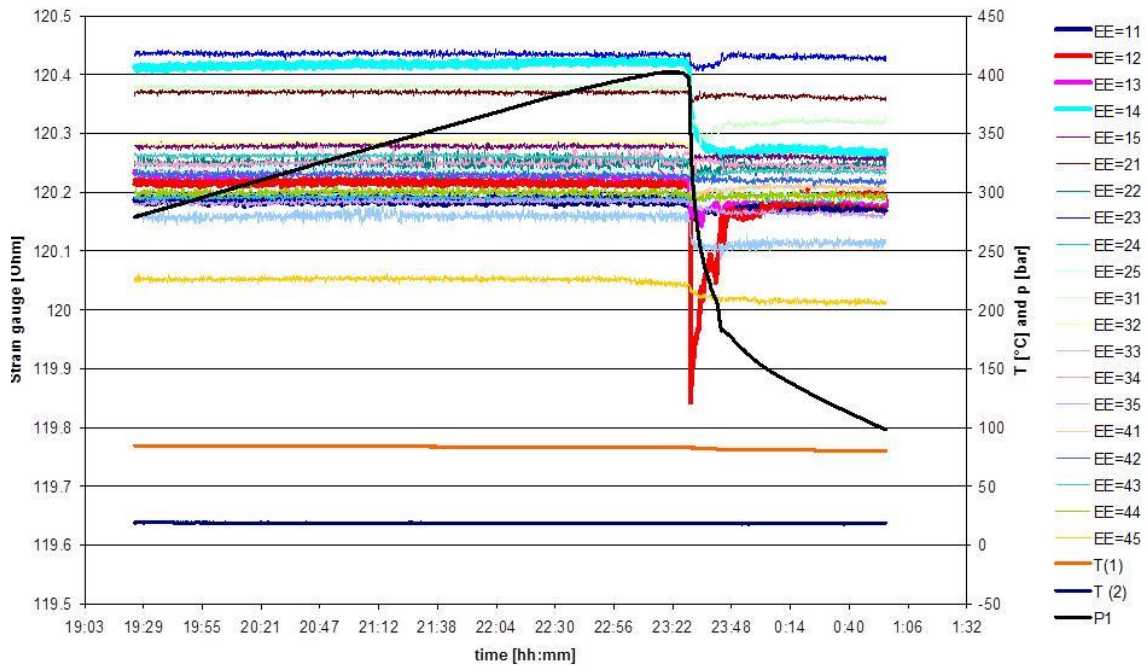


Figure 73 - Tank temperature $T_{(1)}$, room temperature $T_{(2)}$ and bore pressure of the Bore (P). Each strain gauge is also identified in the sequence as (EE).

After the complete dissection of the sample, the rupture of one of the welds close to one of the sealing regions was detected. It is assumed that the rupture of this weld is the most probable source of the failure of the test, as strain gauge EE12, which registered the anomaly, was located on the same side of the broken weld. This rupture resulted in the leaking of CO_2 from the bore of the sample, as it was assumed that the sealing region had slightly twisted after the weld had broken. See Figure 74.



Figure 74 – Broken weld close to one of the sealing regions of the sample, which yielded in the leaking of the CO₂ from the bore of the pipe.

The failure of the sample was not expected. A new sample has been prepared and the test will be repeated in 2015 after the end of this work.

Chapter V

Conclusions and Future Works

'The most beautiful experience we can have is the mysterious. It is the fundamental emotion that stands at the cradle of true art and true science.'

...Albert Einstein

In contrast to the axial loads of polymer layers in flexible risers, respective radial loads have hardly been investigated ⁽¹⁶¹⁾. In the present study, we have shown that the color change of the cold-flowed PVDF material is actually linked to the formation of voids. The white color indicates a probability that even longer voids than those detected exist.

Fortunately, the needle-shaped voids are orientated almost in the axial direction so they do not form suitably directed channels for the passage of gases and liquids through the barrier layer. However, according to our results, sharp edges lead to tilting of marginal voids into the radial direction might influence in the rate of gas permeation through the Flexbarrier.

Nevertheless, the orientation of marginal voids can be controlled by the geometrical shape of the carcass and Flexlok segments, some of which have failed in the test. We have been surprised that the material becomes so strongly orientated by the radial cold flow. A reason may be that the polymer layer is also exposed to tensile stresses in the axial direction due to temperature changes, and radial flow and axial stress interfere constructively.

Remarkably, the morphological differences appear between the two polymer layers. Further investigations could help us to understand them from a fundamental point of view. From the findings of strong polymer orientation the

question arises whether even the mechanical properties of the polymer layers are changed by the cold flow. However, the mechanical properties of a composite flexible pipe are mainly determined by the reinforcing metal coils and not by the polymer barrier.

At location 1, where the Flexlok was undamaged, the PVDF material appears to be unaffected by RGD at some distance from the gaps. At location 2, where the Flexlok broke, the PVDF material showed microvoids through the full thickness.

The Flexlok wires were heavily corroded. This is probably the reason why they broke. In a realistic full-scale test this would not happen, since the carbon steel would not be exposed to high pressure CO₂.

It is also important to highlight that in the region of contact between the Flexbarrier and Flexwear, no voids were detected. The material has remained isotropic, retaining the sealing properties of these layers.

Even under supercritical CO₂, PVDF located outside of the gap regions of the carcass and Flexlok has not presented voids. The presence of the supercritical media alone was not sufficient to affect the microstructure of PVDF. The presence of voids was observed only in the regions where the polymer could flow in line with the cold-flow characteristics.

Void diameter and height were measured in this survey and show their distribution and profile along both the Flexbarrier and Flexwear were reported.

For the Flexbarrier, voids were detected only in depths up to 1 mm in the whitened region. In depths below 1 mm no voids were detected. The SAXS patterns showed an isotropic morphology. Void diameter varied from 20 to 35nm in general.

It is important to highlight once again that in a real application of flexible pipe, the Flexbarrier is not directly exposed to supercritical fluids, and such a level of whitening is not expected.

The SEM images in these regions also show the absence of voids, keeping the properties of the material, even under an extreme condition as reiterated above.

Samples retrieved for SAXS following the manufacture of the flexible pipes without supercritical exposure, have retained their isotropic structure, in other words, the Flexbarrier and Flexwear keep their structure as a virgin PVDF, even after being wound in reels during the manufacturing phases, as well as after the high pressurization with water.

WAXS measurements have been performed and no change of phase has been found for the whitened samples in comparison to the virgin sample. PVDF has kept the arrangement of its morphological structure.

The occurrence of voids in the microstructure of PVDF should be investigated more profoundly in terms of fluid permeation, however, the Flexbarrier has proven suitable for the application when it was exposed to the supercritical media. No failure of the Flexbarrier during the test being experienced. Furthermore the Flexbarrier has preserved its properties in the regions outside of the noses.

It's believed that the supercritical medium used in this research does not jeopardize the operations of the pipes.

Suggestions for Future Work:

1 – Repetition of mid-scale swelling test to measure the strains caused by the swollen PVDF over the Flexlok;

2 – Evaluation of the influence of voids in the permeation rates of fluids through the swollen PVDF and;

3 – Development of a polymeric material for flexible pipe manufacture to work in the presence of CO₂, which is less sensitive to the supercritical media.

References

-
- [1] Aquino, F. G., Estudo do envelhecimento de poliuretanos aplicados na indústria de Petróleo, Universidade do Estado do Rio de Janeiro, **2009**. Master Thesis, 102 p.
- [2] Aquino, F.G., Buchner, S., Pires, F., Clevelario, J., Sheldrake, T., Evaluation of Polymers Applied as Barrier Pressure on Flexibe Pipes when Subjected to Severe Condition, **2012**, Merl Conference.
- [3] Duff, I., Cuminat, J., SIAM News, Volume 44, Number 7, September **2011**.
- [4] Carneiro, R. L. B., Leite, C.S., Lage, A. C. V. M., Netto, J. R. F., Henriques, C. C. D., Pre-salt Santos basin - Challenges and New Technologies for the Development of the Pre-salt Cluster, Santos Basin, Brazil. Offshore Technology Conference, 4-7 May, **2009**, Houston, Texas.
- [5] Bassett, D. C., Developments in Crystalline Polymers - 1, **1982**, New Jersey.
- [6] Aquino, F.G., Unpublished results.
- [7] Silva, M. D. C., Geração do Efeito Whitening em Polifluoreto de Vinilideno (PVDF) Sob Carregamento Cíclico., Dissertação (Mestrado), **2014** – UFRJ/ COPPE/ Programa de Engenharia Metalúrgica e de Materiais.
- [8] Lanceros-Mendez, S., Mano J. F., Costa A. M.,- Schmidt V. H., FTIR And DSC Studies Of Mechanically Deformed- PVDF Films, J. MACROMOL. SCI.— PHYSICS, **2001**, B40(3&4), 517–527.
- [9] Tazaki, M., Wada, R., Okabe, M., Homma, T., J Appl Polym Sci., **1997**, 65, 1517.
- [10] Lee, W.K., Ha, C.S., Polymer, **1998**, 39, 7131.

-
- [11] El Mohajir, B.E., Heymans, N. *Polymer*, **2001**, 42, 5661.
- [12] Takahashi, Y., Matsubara, Y., Tadokoro, H., *Macromolecules*, **1982**, 15, 334.
- [13] Matsushige, K., Nagata, K., Imada, S., Takemura, T., *Polymer*, **1980**, 21, 1391.
- [14] Lu, F.J., Hsu, S.L., *Macromolecules*, **1986**, 19, 326.
- [15] Lovinger, A.J., *Macromolecules*, **1981**, 14, 322.
- [16] Lovinger, A.J., Unpublished results.
- [17] Dohany, J.E., Dukert, A.A. Preston, S.S., III, in: *Encyclopedia of Polymer Science and Technology*, vol. 14, N. M. Bikales, Ed., **1971**, Interscience, New York, p. 600.
- [18] Okazaki, S., Sakauchi, N., *Jap.*, **1968**, Patent 43 – 4867.
- [19] Iserson, H., *US*, **1966**, Patent 3, 245, 971.
- [20] Görlitz, M., Minke, R., Trautvetter, W., Weisgerber, G., *Angew. Makromol. Chem.*, **1973**, 29/30, 137.
- [21] Weinhold, S., Litt, M.H., Lando, J.B., *Polym. Sci., Polym. Lett. Ed.*, **1979**, 17, 585.
- [22] Doll, W.W., Lando, J.B., *J. Appl. Polym. Sci.*, **1970**, 14, 1767.
- [23] Gal'Perin, Ye.L., Kosmyrin, B.P., Aslanyan, L.A, Mlenik, M.P., Smirnov, V.K., *Polym. Sci.*, **1881**, USSR, **1970**, 12.

-
- [24] Gianotti, G., Capizzi, A., Zamboni, V., *Chim. E industry.*, **1973**, 55, 501.
- [25] Prest, W.M.Jr., Luca, D.J., *J. Appl. Phys.*, **1975**, 46, 4136.
- [26] Silva, A., B., *Processamento, Caracterização e Determinação do Perfil de Polarização do Poli(fluoreto de vinilideno)*, Dissertação de Mestrado, **2009**, UFSCar São Paulo, SP, Brasil.
- [27] Gregorio R. J., Borges D. S., *Effect of Crystallization Rate on the Formation of the Polymorphs of Solution Cast Poly(vinylidene fluoride)*, *Polymer*, **2008**, v. 49 pp. 4009–4016.
- [28] Esterly. D. M., *Manufacturing of Poly(vinylidene fluoride) and Evaluation of its Mechanical Properties*. Masters of Science, **2002**, Virginia Polytechnic Institute and State University, Blacksburg, Virginia.
- [29] Sencadas, V., Lanceros-Méndez, S., Pouzada, A.S., Gregorio Jr, R., *Mat. Sci.*, **2006**, Forum 872, 514–516.
- [30] Kholkin, A.L., Kalinin, S.V., Roelofs, A., Gruverman, A., *Scanning Probe Microscopy: Electrical and Electromechanical Phenomena at the Nanoscale*, vol. 1, ed. by S. Kalinin, A. Gruverman, Springer, New York, **2007**, pp. 173–214.
- [31] Serrado Nunes, J., Wu, A., Gomes, J., Sencadas, V., Vilarinho, P.M., Lanceros-Méndez, S., *Relationship Between the Microstructure and the Microscopic Piezoelectric Response of the α - and β -phases of Poly(vinylidene fluoride)*, *Appl Phys A*, **2009**, 95: 875–880.
- [32] Peterlin, A., Baltá-Calleja, F.J., *J. Appl. Phys.*, **1969**, 40, 4238.
- [33] Ward, I.M., *Mechanical Properties of Solid Polymers*. 2nd Edition, **1983**, John Wiley and Sons.

-
- [34] Kammer, H.W., Kummerloewe, C., Greco, R., Mancarella, C., Martuscelli, E., *Polymer*, **1988**, 29, 963.
- [35] Osawa, S., Porter, R.S., *Polymer*, **1994**, 35, 540.
- [36] Lazurkin, Y.S., *Polym. Sci.*, **1958**, 30, 595.
- [37] Robertson, R.E., *J. Chem. Phys.*, **1966**, 44, 3950.
- [38] Marshall, I., Thompson, A.B., *Proc. Roy. Soc. A.*, **1954**, 221, 541.
- [39] Argon, A.S., Andrews, R.D., Godrick, J.A., Whitney, W., *J. Appl. Phys.*, **1968**, 39, 1899.
- [40] Brown, N., *Mater. Sci. Eng.*, **1971**, 8, 69.
- [41] Bochum, A.S., *Kunststoffe*, **1982**, 72, 791.
- [42] Peterlin, A.J., *Polym. Sci.*, **1965**, C9, 61.
- [43] Young, R.A., Sokthivel, A., *J. Appl. Cryst.*, **1988**, 21, 416.
- [44] Lutz, C., Fischer, G., Eyerer, P., ANTEC87, **1987**, 1018.
- [45] Friedrich, K., in *Advances in Polymer Science*, **1983**, 225.
- [46] Young R.J., Lowell P.A., *Introduction to Polymers*. 2nd ed. London: Chapman & Hall, **1991**, p. 177.
- [47] Courtney P.H., *Mechanical Behavior of Materials*. Singapore: McGraw-Hill, **2000**.

-
- [48] Bowden, P. D., Young, R. J. J., *Mater. Sci.*, **1974**, 9, 2034.
- [49] Perkins, W. G., Porter, R. S. J., *Mater. Sci.*, **1977**, 12, 2355.
- [50] Magill, J. H., *Treatise on Materials Science and Technology* (Ed. J. M. Schultz), **1977**, 10A.
- [51] Kausch, H. H., *Polymer Fracture*, Springer Verlag, Berlin, **1978**.
- [52] Kambour, R. P. J., *Polym. Sci. (Macromol. Rev.)*, **1973**, 7, 1.
- [53] Stein, R. S. J., *Polym. Sci. (C)*, **1966**, 15, 185.
- [54] Peterlin, A., *Macromol. Chem.*, **1977**, 8, 277.
- [55] Peterlin, A., *Symposium on Polymer Science and Engineering*, Ed. K. D. Pae, Plenum, New York, **1972**, p 1.
- [56] Olf, H. G., Peterlin, A. J., *Polym. Sci., Polym. Phys. Edn.*, **1974**, 12, 2209.
- [57] Van den Boogart, A., *Physical Basis of Yield and Fracture*, Inst. Phys. and Phys. Soc., **1966**, p 167.
- [58] Todo, A., Hashimoto, T., Kawai, H., *Polym. J.*, **1979**, II, 59.
- [59] Friedrich, K., *Fracture 1977*, ICF4, Waterloo, **1977**, 3, 1119.
- [60] Cessna L.C., *Polym Eng. Sci.*, **1974**, 14, 696.
- [61] Narisawa I., Ishikawa M. ,In: Kausch H.H., editor. *Crazing in polymers*, *Advances in polymer sciences*, 91/92. Berlin: Springer, **1990**. p. 353.

[62] Plummer C.J.G., Kausch, H.H., J Macromol. Sci. Phys., **1996**,35,637.

[63] Castagnet, S., Comportement mecanique du PVDF: Competition entre cavitation et e'coulement visqueux, Thesis, Poitiers, France, **1998** [in French].

[64] Hartmann, B., Lee, G.F., Tensile yield in PCTFE and PVDF. Polym. Eng. Sci., **1991**, 31, 231–8.

[65] Castagnet, S., Girault, S., Gacougnolle, J.L., Dang, P., Cavitation in strained PVDF: mechanical and X-ray experimental studies. Polymer, **2000**, 41(20), 7523–30.

[66] Friedrich K., In: Kausch H.H., editor. Crazing in polymers, Advances in polymers science, 52/53. Berlin: Springer, **1983**. p. 353.

[67] Volynskii, A.L., et al. Polym. Sci., **1991**, 33, 917.

[68] Dettenmaier, M., Kausch, H.H., Polym. Bull., **1980**, 3, 571.

[69] Dettenmaier, M., Kausch, H.H., Colloid Polym. Sci., **1981**, 259, 937.

[70] Aquino, F.G., Unpublished results.

[71] Bakshi, S., Kulshreshtha, A. K., Singh, B. P., Anand , J. S., Polymer Testing, **1988**, 8, 191.

[72] Samon, J.M., Schultz, J.M., Hsiao, B.S., Polymer, 41, **2000**, 2169–2182.

[73] Aquino, F.G., Stribeck, N.,Li, X., Zeinolebadi, A., Buchner, S., Santoro, G.,Macromolecular Materials and Engineering, **2015**, MME-S-15-00064.

[74] Sobhani, H., Razavi-Nouri, M., Yousefi, A. A., J. Appl. Polym. Sci. **2007**, 104, 89.

[75] Nakamura, K., Nagai, M., Kanamoto, T., Takahashi, Y., Furukawa, T., J. Polym. Sci. Part B Polym. Phys., **2001**, 39, 1371.

[76] Hsu, T., Geil, P. H., J. Mater. Sci., **1989**, 24, 1219.

[77] Androsch, R., Stribeck, N., Lupke, T., Funari, S. S., J. Polym. Sci.: Part B: Polym. Phys., **2002**, 40, 1919–1930.

[78] Rindfleisch F., DiNoia, T. P., McHugh, M. A., J. Phys. Chem. **1996**, 100, 15581-15587.

[79] Higuchi, A., Nakagawa, T., J Polym. Sci. Part B Polym. Phys., **1994**, 32, 149.

[80] Mawson, S., Johnston, K.P., Combes, J.R., DeSimone, J.M., Macromolecules, **1995**, 28, 3182.

[81] Su, B., Lv, X., Yang, Y., Ren, Q., J Chem Eng Data, 2006, 51, 542.

[82] Lora, M., Lim, J.S., McHugh, M.A., J Phys Chem B, **1999**, 103, 2818.

[83] Raveendran, P., Wallen, S.L., J Phys Chem B, 2003, 107, 1473.

[84] Mertdogan, C.A., McHugh, M.A., and W.H. Tuminello, "Cosolvency effect of SF₆ on the solubility of poly(tetrafluoroethylene-co-19 mol% hexafluoropropylene) in supercritical CO₂ and CHF₃," Journal of Applied Polymer Science, 74, 2039-2045 (1999).

[85] Tuminello, W. H., Dee, G. T., McHugh, M. A., Macromolecules, **1995**, 28, 1506.

[86] Lapeilleur, C., Beckman, E. J., Schonemann, H., Krukonis, V. J., *Fluid Phase Equilib.*, 134, 285-305, 1997.

[87] Howdle, S., Paper presented at the Fourth Nottingham/Leeds Symposium, *Supercritical Chemistry* **1996**, Nottingham, England.

[88] McHugh, M. A., Krukonis, V. J., *Supercritical Fluid Extraction: Principle and Practice*, 2nd ed., **1994**, Butterworths: Stoneham, MA.

[89] Yilgor, I., McGrath, J. E., Krukonis, V. J. J., *Polym. Bul.* **1984**, 12,499.

[90] Krukonis, V. J. J., *Polym. News*, 1985, 11, 7.

[91] Hoefling, T. A., Enick, R. M., Beckman, E. J. J., *Phys. Chem.*, **1991**, 95, 7127.

[92] Hoefling, T. A., Stofesky, D., Reid, M., Beckman, E. J., Enick, R.M. J., *Supercrit. Fluids*, 1992, 5, 237.

[93] Dris, G., Barton, S. W., *Polym. Mater. Sci. Eng.*, **1996**, 74, 226.

[94] Zhao, X., Watkins, R., Barton, S. W. J., *Appl. Pol. Sci.*, **1995**, 55, 773.

[95] Xiang, Y., Kiran, E., *Polymer*, **1995**, 36, 4817.

[96] Gregg, C. J., Stein, F. P., Radosz, M., *Macromolecules*, **1994**, 27, 4972.

[97] Gregg, C. J., Stein, F. P., Radosz, M., *Macromolecules*, **1994**, 27, 4981.

[98] Aquino, F.G., Unpublished results.

[99] Quijada-Garrido, I., Barrales-Rienda, J. M., Frutos, G., Diffusion of erucamide (13-cisdocosamide) in isotactic polypropylene. *Macromolecules*, **1996**, 29, 7164-7176.

[100] Földes, E., Transport of small molecules in polyolefins. II. Diffusion and solubility of Irganox 1076 in ethylene polymers. *J. Appl. Polym. Sci.*, **1993**, 48, 1905-1913.

[101] Klein, J., Briscoe, B. J., Diffusion of long molecules through solid polyethylene. II. Measurement and results. *J. Polym. Sci., Polym. Phys. Ed.*, **1977**, 15, 2065-2074.

[102] Rawls, A., Diffusion of an erucamide slip additive in linear low-density polyethylene film. M.S., Clemson University, **1997**.

[103] Schlotter, N. E., Furlan, P. Y., A review of small molecule diffusion in polyolefins. *Polymer*, **1992**, 33, 3323-3342.

[104] Stern, S. A., Polymers for gas separations: the next decade. *J. Membr. Sci.*, **1994**, 94, 1-65.

[105] Zeinolebadi, A., In-situ Small-Angle X-ray Scattering Investigation of Transient Nanostructure of Multi-Phase Polymer Materials Under Mechanical Deformation, PhD Thesis, University of Hamburg, **2012**.

[106] Stribeck, N., X-ray Scattering of Soft Matter, Springer-Verlag, Berlin Heidelberg, 2007.

[107] Stribeck, N., X-ray Scattering for the Monitoring of Processes in Polymer Materials with Fiber Symmetry, *J. Macromol. Sci. Part C: Polymer Reviews*, **2010**, 50, 40–58.

[108] Akpalu, Y. A., Scattering from Polymers, *J. Macromol. Sci. Part C: Polymer Reviews*, **2010**, 50, 1–13.

[109] Phillips, A., Zhu, P. W., Edward, G., Simple Shear Deformation of Polypropylene via the Equal Channel Angular Extrusion Process, *Macromolecules*, **2006**, 39, 5796–5803.

[110] Morosoff, N., Petterlin, A., Plastic Deformation of Polypropylene. IV. Wide-Angle X-ray Scattering in the Neck Region, *J. Polym. Sci. Part A-2: Polym. Phys.* **1972**, 10, 1237–1254.

[111] Ran, S., Zong, X., Fang, D., Hsiao, B. S., Chu, B., Phillips, R. A., Structural and Morphological Studies of Isotactic Polypropylene Fibers During Heat/Draw Deformation by in-situ Synchrotron SAXS/WAXD, *Macromolecules* **2001**, 34, 2569–2578.

[112] Baltá Calleja, F. J., Petterlin, A., Crist, B., Plastic Deformation of Polypropylene VII. Long Period as Function of Temperature and Rate of Drawing, *J. Polym. Sci. Part A-2: Polym. Phys.* **1972**, 10, 1749–1756.

[113] Phillips, A., Zhu, P. W., Edward, G., Simple Shear Deformation of Polypropylene via the Equal Channel Angular Extrusion Process, *Macromolecules*, **2006**, 39, 5796–5803.

[114] Nozue, Y., Shinohara, Y., Ogawa, Y., Sakurai, T., Hori, H., Kasahara, Tatsuya., Yamaguchi, N., Yagi, N., Amemiya, Y., Deformation Behavior of Isotactic Polypropylene Spherulite during Hot Drawing Investigated by Simultaneous Microbeam SAXS-WAXS and POM Measurement, *Macromolecules*, **2007**, 40, 2036–2045.

[115] Pawlak, A., Galeski, A., Cavitation during Tensile Deformation of Polypropylene, *Macromolecules*, **2008**, 41, 2839–2851.

-
- [116] Nitta, K. H., Takayanagi, M., Role of Tie Molecules in the Yielding Deformation of Isotactic Polypropylene, *J. Polym. Sci. Part B: Polym. Phys.* **1999**, 37, 357–368.
- [117] Goderis, B., Reynaers, H., Koch, M. H. J., Mathot, V. B. F., *J. Polym. Sci.: Part B: Polym. Phys.*, 37, **1999**, 1715–1738.
- [118] Vaia, R. A., Liu, W., Koerner, H., Analysis of Small-Angle Scattering of Suspensions of Organically Modified Montmorillonite: Implications to Phase Behavior of Polymer Nanocomposites, *J. Polym. Sci. Part B Polym. Phys.*, **2003**, 41, 3214–3236.
- [119] Stribeck, N., Almendárez Camarillo, A., Nöchel, U., Schroer, C., Kuhlmann, M., Roth, S. V., Gehrke, R., Bayer, R. K., Volume-Resolved Nanostructure Survey of a Polymer Part by Means of SAXS Microtomography, *Macromol. Chem. Phys.*, **2006**, 207, 1239–1249.
- [120] Stribeck, N., Nöchel, U., Almendárez Camarillo, A., Scanning Microbeam X-ray Scattering of Fibers Analyzed by one-Dimensional Tomography, *Macromol. Chem. Phys.*, **2008**, 209, 1976–1982.
- [121] Sakurai, S., Yoshida, H., Hashimoto, F., Shibaya, M., Ishihara, H., Yoshihara, N., Nishitsuji, S., Takenaka, Ultra Small-Angle X-ray Scattering Studies on Structural Changes in Micrometers Upon Uniaxial Stretching of Segmented Polyurethaneureas, *Polymer*, **2009**, 50, 1566–1576.
- [122] Bragg, W. H., Bragg, W. L., The Reflection of X-ray by Crystals, *Proc. R. Soc. Lond. A*, **1913**, 88, 428–438.
- [123] Fakirov, S., Samokovliyski, O., Stribeck, N., Apostolov, A. A. Denchev, Z., Sapoundjieva, D., Evstatiev, M., Meyer, A., Stamm, M., *Macromolecules*, **2001**, 34, 3314–3317.

[124] Stribeck, N., Scattering of Soft Condensed Matter. From Fundamentals to Application, in Applications of Synchrotron Light to Scattering and Diffraction in Materials and Life Sciences, Ezquerra, T. A., Garcíá Gutiérrez, M., Nogales, A., Gómez, M., eds., Springer, Berlin Heidelberg, **2009**, volume 776 of Lect. Notes Phys. pp. 25–62.

[125] Stribeck, N., Buchner, S., J. Appl. Cryst., **1997**, 30, 722.

[126] Stribeck, N., Bayer, R., Krosigk, G., Gehrke, R., Polymer, **2002**, 43, 3779.

[127] Ruland, W., The Evaluation of the Small-Angle Scattering of Lamellar Two-Phase Systems by Means of Interface Distribution Functions, Colloid Polym. Sci., **1977**, 255, 417–427.

[128] Ruland, W., The Evaluation of the Small-Angle Scattering of Anisotropic Lamellar Two-Phase Systems by Means of Interface Distribution Functions, Colloid Polym. Sci., **1978**, 256, 932–936.

[129] Stribeck, N., Ruland, W., Determination of the Interface Distribution Function of Lamellar Two-Phase Systems, J. Appl. Cryst., **1978**, 11, 535–539.

[130] Méring, J., Tchoubar-Vallat, D., X-ray. Small-Angle X-ray Scattering in Diluted Suspensions. Computations of Chord Distributions (fr.), C. R. Acad. Sc. Paris, **1965**, 261, 3096–3099.

[131] Méring, J., Tchoubar-Vallat, D., Solid State Physics. Diffuse Small-Angle X-ray Scattering from Concentrated Systems (fr.), C. R. Acad. Sc. Paris, **1966**, 262, 1703–1706.

[132] Méring, J., Tchoubar, D., Interpretation of the SAXS from Porous Systems. Part I. (french), J. Appl. Cryst., **1968**, 1, 153–165.

-
- [133] Tchoubar, D., Méring, J., Interpretation of the SAXS from Porous Systems. Part II. (french), *J. Appl. Cryst.*, **1969**, 2, 128–138.
- [134] Stribeck, N., *J Appl Cryst*, **2001**, 34(4), 496–503.
- [135] Vonk, C.G., *Colloid Polym Sci.*, **1979**, 257, 1021–32.
- [136] Stribeck, N., Fakirov, S., *Macromolecules*, **2001**, 34(22), 7758–61.
- [137] Barbi, V., Funari, S.S., Gehrke, R., Scharnagl, N., Stribeck, N., *Macromolecules*, **2003**, 38(3) 749–58.
- [138] Stribeck, N., Androsch, R., Funari, S.S., *Macromol. Chem. Phys.*, **2003**; 204(9):1202–16.
- [139] Stribeck, N., Fakirov, S., Apostolov, A.A., Denchev, Z., Gehrke, R., *Macromol. Chem. Phys.*, **2003**, 204(7), 1000–13.
- [140] Ruland, W., *Small-Angle Scattering of Two-Phase Systems: Determination and Significance of Systematic Deviations from Porod's Law*, *J. Appl. Cryst.*, **1971**, 4, 70–73.
- [141] Koberstein, J. T., Morra, B., Stein, R. S., *The Determination of Diffuse-Boundary Thicknesses of Polymers by Small-Angle X-ray Scattering*, *J. Appl. Cryst.*, **1980**, 13, 34–45.
- [142] Stribeck, N., *Nanostructure Evolution Studies of Bulk Polymer Materials with Synchrotron Radiation. Progress in Method Development*, *Anal. Bioanal. Chem.*, **2003**, 376, 608–617.
- [143] VNI, 'PV-WAVE manuals,' V 7.5, Houston, TX, USA **2007**.

-
- [144] Buhmann, M. D., *Acta Numerica*, **2000**, 9, 1.
- [145] Porod, G., *Makromol. Chem.*, **1960**, 35, 1.
- [146] Statton, W. O., *J. Polym. Sci.*, **1962**, 58, 205.
- [147] Bonart, R., *Kolloid Z. u. Z. Polymere*, **1966**, 211, 14.
- [148] Perret, R., W. Ruland, *J. Appl. Cryst.*, **1970**, 3, 525.
- [149] Peterlin, A., *J. Mater. Sci.*, **1971**, 6, 490.
- [150] Peterlin, A., *Text. Res. J.*, **1972**, 42, 20.
- [151] Porod, G., *Fortschr. Hochpolym.-Forsch.*, **1961**, 2, 363.
- [152] Tang, Y., Jiang, Z., Men, Y., An, L., Endere, H.-F., Lilge, D., Roth, S. V., Gehrke, R., Rieger, J., *Polymer*, **2007**, 48, 5125.
- [153] Ruland, W., *Colloid Polym. Sci.*, **1977**, 255, 417.
- [154] Stribeck, N., Zeinolebadi, A., Ganjaee Sari, M., Botta, S., Jankova, K., Hvilsted, S., Drozdov, A., Klitkou, R., Potarniche, C.-G., Christiansen, J. d., Ermini, V., *Macromolecules*, **2012**, 45, 962.
- [155] Mohammadi B., Yousefi, A. A. and Bellah, S. M., *Polymer Testing*, **2007**, 26, 42-50.
- [156] Sun, L.L., Li, B., Zhang, Z.G., and Zhong, W.H., *Eur. Polym. J.*, **2010**, 46, 2112-2119.
- [157] Wu, J. and Schultz, J. M., *Macromolecules*, **2000**, 33, 1765-1777.
- [158] Maier, G. A., Wallner, G., Lang, R. W. and Fratzl, P., *Macromolecules*, **2005**, 38, 6099-6105.

[159] Huilong, G., Yao, Z., Feifei, X., Ziwei, C., Yingrui, S., Jingqing, L., Yu, C., Zhonghua, W., and Shichun, J., In-situ Synchrotron SAXS and WAXS Investigations on Deformation and α - β Transformation of Uniaxial Stretched Poly(vinylidene fluoride) CrystEngComm, **2013**,15, 1597-1606.

[160] Laroche,G., Lafrance, C.P., Prud'homme, R. E., and Guidoin, R., J. Biomed. Mater.Res., **1998**, 39, 184-189.

[161] Shen, Y., Zhao, J., Tan, Z., Sheldrake, T., in: '30th International Conference on Ocean, Offshore and Arctic Engineering', vol. 4, pp. 353–359, **2011** pp. 353–359.

[162] GE/Wellstream Internal Report (WSI-006) - Unpublished results.

Die Ergebnisse dieser Arbeit wurden zum Teil in dem folgenden Paper veröffentlicht.

Publikation

Aquino, Fabio; Stribeck, Almut; Li, Xuke; Zeinolebadi, Ahmad; Buchner, Stefan; Santoro, Gonzalo '*Variation of PVDF morphology due to radial cold flow in a flexible pipe*', *Polymer Engineering and Science*, 2015.

Teilnahme auf Tagungen/Konferenzen

1. Aquino F., Stribeck, N., Santoro G., 'Study of the Rearrangement of PVDF nanostructure by embossment of a corrugated metal hob by means of SAXS,'
XIPS 2013 - IX International Conference on X-ray Investigations of Polymer Structure – Zaczopane/Poland
2. Aquino F., Stribeck, N., Li X., Zeinolebadi, A., Buchner S., Santoro G., 'Rearrangement of PVDF morphology due to radial cold flow in a flexible pipe',
European Polymer Congress 2015 – Dresden/Germany
3. Aquino F., Stribeck, N., Li X., Zeinolebadi, A., Buchner S., Santoro G., 'Rearrangement of PVDF morphology due to radial cold flow in a flexible pipe',
Synchrotron Radiation in Polymer Science 2015 – Madrid/Spain
4. Aquino F., Stribeck, N., Li X., Zeinolebadi, A., Buchner S., Santoro G., 'Rearrangement of PVDF morphology due to radial cold flow in a flexible pipe',
16th International Conference on Small-Angle Scattering (SAS 2015), Berlin/Germany

Further Acknowledgments

Firstly, I would like to thank Hamburg University and also;

Thanks to Hamburg Synchrotron Radiation Laboratory (HASYLAB) for beam time granted.

Thanks to GE Oil & Gas

Thanks to Polymer Consult

List of hazardous materials used in this thesis.

None

Eidesstattliche Versicherung

Hiermit versichere ich an Eides statt, die vorliegende Dissertation selbst verfasst und keine anderen als die angegebenen Hilfsmittel benutzt zu haben. Ich versichere, dass diese Dissertation nicht in einem früheren Promotionsverfahren eingereicht wurde.

Hamburg den

Fabio Aquino